Radiative Effects of Boundary Layer Aerosols: Detectability of Hazes by GOES-8 And Estimation of Their Direct Effect

by
Kenneth R. Knapp

Department of Atmospheric Science
Colorado State University
Fort Collins, Colorado

Colorado State University

Department of Atmospheric Science

Paper No. 623

RADIATIVE EFFECTS OF BOUNDARY LAYER AEROSOLS: DETECTABILITY OF HAZES BY GOES-8 AND ESTIMATION OF THEIR DIRECT EFFECT

by

Kenneth R. Knapp

Department of Atmospheric Science

Fall 1996

ABSTRACT OF THESIS

RADIATIVE EFFECTS OF BOUNDARY LAYER
AEROSOLS: DETECTABILITY OF HAZES BY GOES-8
AND ESTIMATION OF THEIR DIRECT EFFECT

Atmospheric aerosols have an important role in the atmosphere through their radiative effects. Their cooling effect on the earth/atmosphere system is caused by reflecting more solar radiation (direct effect) and by increasing the total radiation reflected by clouds (indirect effect). The direct effect often renders aerosols detectable by satellites.

An Adding/Doubling model was used to retrieve aerosol optical depths over the Eastern U.S. from visible GOES-8 imagery during the summer of 1995. The Eastern U.S. is an excellent area to study aerosols because of (a) the amount of natural and anthropogenic aerosols emitted, (b) the weak summertime circulations and (c) the high relative humidities caused by the Bermuda High. Sensitivity analysis showed that retrieval of optical depth, τ, was possible from satellite to a resolution of 0.01 for dark backgrounds with primarily scattering aerosols. However, uncertainties due to instrument calibration and assumed aerosol optical properties suggested optical depth was sensed with a range of error $\pm(0.05\text{-}0.16)$ for optical depths less than one. Comparisons of the retrieved τ were made to the following surface data: a pyrheliometer, a transmissometer, several nephelometers and standard National Weather Service visibility observations. The nephelometers and transmissometer were operated by the Interagency Monitoring of Protected Visual Environments (IMPROVE). The pyrheliometer was operated by the Baseline Surface Radiation Network (BSRN) at the ARM (Atmospheric Radiation Measurements) site in Oklahoma. Correlation of satellite-based retrievals were found with the IMPROVE dataset (located in Virginia, Tennessee, Kentucky and West

Virginia) which contained the most haze events. The correlation of τ estimated from satellite data to NWS visibility measurements was poor in part due to low resolution of the surface reports.

Using a 2-stream radiative transfer model, the magnitudes of the direct aerosol effect were investigated from retrieved optical depths. It was found that the magnitude is linearly dependent upon optical depth. Aerosols in pollution episodes reflect about 1 to 3% of the available solar radiation. It was also found that the aerosol forcing (magnitude of the direct effect) might be directly measured by satellite without estimating optical depth.

ACKNOWLEDGEMENTS

This work was sponsored by the Department of Defense Center for Geosciences, Phase II, under grant #DAAH04-94-G-0402.

TABLE OF CONTENTS

LIST OF FIGURES

LIST OF TABLES

Introduction

Visible imagery from meteorological satellites has proved to be a valuable forecast and research tool for investigating meteorological phenomena. One of the many observable features in a visible satellite image is aerosols. Aerosols are observed being advected off the Western African coast, as well as in stagnant haze cases over the Midwest and Eastern United States (e.g., Carlson, 1979; Kaufman et al, 1990). Aerosols can degrade visibility, increase the local albedo by scattering more solar radiation to space, and also provide a medium for many atmospheric chemical reactions. The Interagency Monitoring of Protected Visual Environments (IMPROVE) program monitors aerosols and their effect on visibility at National Parks in the U.S. Satellite measurements of the amount of aerosol have been performed primarily over the ocean, which is a uniformly reflecting surface, and to some extent over land, a heterogeneously reflecting surface. Surface reflectance homogeneities play an important role in blurring satellites images, especially near distinct boundaries, e.g. coastlines, lakes and rivers. Retrievals of optical depth use radiative transfer models, although Fourier transforms and modulation transfer functions have also been used. Most of the previous work employed the higher spatial resolution and better data digitization of polar orbiting satellites (e.g. Landsat and National Oceanographic and Atmospheric Administration (NOAA) series)

(e.g., Durkee,1994; Kaufman, 1987) while limited studies use geostationary satellites (e.g. Geostationary Observational Environmental Satellite (GOES) series and METEOSAT) (e.g., Fraser et al., 1984). However, the GOES-8 satellite, launched in the spring of 1994, and others in its series provide high precision and spatial resolution data with better temporal coverage than polar orbiting satellites.

1.1 Background

1.1.1 Previous Aerosol and Haze Detection from Space

It is well known that satellite detected radiance over water is positively correlated to vertically integrated aerosol extinction – aerosol optical depth (Griggs 1979b, Durkee 1984). That is, as the aerosol optical depth increases the upwelling radiance detected by satellite instruments also increases. This happens because the ocean is a dark reflecting surface and aerosols are a predominantly scattering medium that scatter more radiation upward toward the satellite, which brightens a pixel. Land, however, is generally a brighter, less uniformly reflecting surface as seen in figure 1.1. So an aerosol might increase or decrease the upwelling radiance depending on the surface reflectance and aerosol absorptive properties (Kaufman, 1987). Previous investigators use approximate solutions to the radiative transfer to estimate the aerosol effect on satellite imagery, such as adding/doubling or 2n-stream models which take into account surface reflectance and aerosol and atmospheric optical properties. However, at nadir satellite observations, an analytical solution to the radiative transfer problem can be derived and is computationally

faster (Mekler and Kaufman, 1980), which is the case with some polar orbiting satellite instruments.

Landsat has been the primary satellite used in aerosol studies. The Thematic Mapper (TM) sensor has 6 channels between 0.45 and 2.35 μm, two of which are in the visible spectrum. The multiple shortwave channels allow the retrieval of multiple properties such as surface reflectance and optical depth (Conel, 1990). Unfortunately, the return time of Landsat is long such that coincident images are 9 days apart. This increases error when properties of the surface, aerosol or solar geometry are assumed constant between images, as does Kaufman (1987). The Advanced Very High Resolution Radiometer (AVHRR) sensor aboard the NOAA satellites present similar temporal problems. Conversely, geostationary satellites provide the best temporal coverage, at the sacrifice of high spatial resolution and multi-spectral imagery. Geostationary satellites - Meteosat, GOES-7 and GOES-NEXT - have only one visible channel and instantaneous field of view (FOV) of 1 km at NADIR.

Whereas using radiative transfer solutions may seem more intuitive, fast Fourier transforms (FFT) also provide insight to the optical depth of an aerosol. Modulation transfer functions (MTF), a form of FFT, are widely used in optics and to some extent atmospheric optics via remote sensing (Mekler and Kaufman, 1980; Valley, 1993; McDonald et al., 1993). Mekler and Kaufman (1980) provide a general introduction to the use of MTFs in remote sensing. In general, the MTF can be applied to the analytical solution of the radiative transfer equation and used to calculate theoretical detected radiance or other optical properties, such as optical depth.

Comparison between a satellite derived quantity and ground truth is somewhat ambiguous because it is comparing a point measurement at the surface and a vertically and horizontally averaged quantity. Some studies make comparisons to spatially averaged data measured using an aircraft (Durkee, 1984; Hindman et al., 1984; Kaufman et al., 1986). But this is costly to arrange, therefore most researchers compare optical depth retrievals to point measurements, from sun photometers and radiometers or visibility observations. Table 1.1 summarizes the satellites used, range of optical depths found and errors estimated in some previous studies (and including this work). The AVHRR, Imager, VISSR and SMS-1 instruments have similar spectral ranges in the visible and spatial resolutions, whereas the Landsat/MSS has finer spectral and spatial resolutions.

Spinhirne et al. (1980) studies the vertical structure of aerosol in the southwestern United States. Vertical cross sections, calculated from lidar measurements, show cases homogeneous and exponentially decreasing aerosol loading in the boundary layer. They also calculate that the boundary layer optical depth makes up about 83% of the atmospheric optical depth from 0 to 16 km.

Pinnick et al. (1993) studies the aerosol over the desert Southwestern U.S. Measurements of vertical structure show aerosols mainly confined to the boundary layer, with a sharp decrease in aerosol above it. Data show that as the boundary layer height increases through the day, and with it the height of the aerosol layer, the total optical depth remains constant. For cases when there is no atmospheric inversion defining a boundary layer, aerosol concentrations decrease monotonically upward.

Carlson (1979) uses a Monte Carlo model to retrieve Saharan dust optical depths from NOAA-3/VHRR (Very High Resolution Radiometer) imagery off the western coast of Africa. Retrieved optical depths range from 0.2 to 3.0, although the photometer network never measured an optical depth larger than 2.0. The emphasis of his work is on spatial distributions, not retrieval validation. He contours the optical depths for many cases and investigates the spatial distributions of these Saharan dust outbreaks being transported across the Atlantic Ocean.

Kaufman and Fraser (1983) study light extinction during summer air pollution events. They measure various aerosol parameters in the Washington D.C. area during July and August of 1980 and 1981. Optical thickness is derived from solar transmission measurements (from a transmissometer) ranging from 0.1 to 1.5 with daily variations around 0.2. They compare optical depth measurements to inverse visibility and found a correlation coefficient (r) of 0.85 for 1980, but only 0.58 for 1981. They attribute the change in correlation coefficients to variations in the aerosol scattering depth. Also, higher correlation was found in the mid-morning hours of 10:00 to 13:00 EDT.

Durkee, in 1984, studies aerosols in the marine boundary layer off the coast of Southern California. He does not retrieve optical depth, rather he compares upwelling radiance from NOAA-7/AVHRR (Advanced Very High Resolution Radiometer) and NIMBUS-7/CZCS (Coastal Zone Color Scanner) to optical depths calculated from size distributions measured by instruments onboard a twin-engine Piper Navajo airplane. Results show that aerosols above the boundary layer add uncertainty to this relationship.

Kaufman (1987) uses Landsat/TM data to retrieve optical depth and single scatter albedo, although he only performs one retrieval on two images 18 days apart, without any

comparison to surface data. The average retrieved optical depth is 0.6. His work utilizes the fact that the same aerosol will darken a bright surface and brighten a dark surface. Hence, between these effects there exists a surface reflectance for which there is no change in apparent reflectance. This critical reflectance, that renders an aerosol undetectable, is discussed in section 3.1.2. He uses critical reflectance detected with Landsat/TM data to estimate the single scatter albedo of the aerosol.

Kaufman et al. (1990) retrieves aerosol optical thicknesses ranging from 0.6 to 2.5 on one summer day over the northeast U.S. using NOAA-7/AVHRR imagery. Some assumptions that he makes are similar to those in this study: 1) the surface reflectance does not change between the hazy and clear days, 2) the surface is Lambertian, and 3) the haze layer is introduced on top of a background aerosol with the same optical properties. Once again, coincident NOAA-7 imagery is only available every nine days, which adds uncertainty to the first and third assumption. Because the AVHRR instrument has two channels in the visible, they are also able to retrieve mean particle radius and single scatter albedo. By using the mean particle radius to estimate the aerosol phase function, they are able to retrieve optical depths with an estimated error of $\Delta\tau = \pm(0.08\text{-}0.15)$. In this study, retrievals were made with no a priori knowledge of aerosol optical parameters.

Fraser et al. (1984) uses the Visible Infrared Spin Scanner Radiometer (VISSR) on GOES-7 to retrieve optical depths over the Eastern U.S. While the main effort was aimed at aerosol transport, he does make some comparisons between retrieved optical depths and surface measurements of τ. The estimated error ranges from 0.05 to 0.2 for τ values between 0.1 and 1.0, and goes as far as to say, "...the surface concentration of

aerosol mass is a poor estimator for columnar mass on many occasions, especially during air pollution episodes." This is important to this work because most of the available sources for comparison are surface extinction measurements. Later, Fraser (1993) retrieves optical depths over Tadzhikistan for a dust layer using NOAA/AVHRR imagery. Optical depths there range from 0.2 to 1.6 with an estimated error of $\Delta\tau = \pm 0.2$. Comparisons were made to surface visibility reports.

More recently, Kaufman (1993) stated that there are still some unanswered questions on the remote sensing of aerosols, some of which apply directly to this work:

1. "How accurately can we sense aerosol from space?"
2. "What are the uncertainties in the remotely sensed quantities due to the assumed particle composition, sphericity and size distribution?"
3. "For what conditions and geographical locations should atmospheric corrections of space-borne imagery be performed?"
4. "What is the relationship between aerosol loading and backscattering of radiation to space?"

The goal of this work was to retrieve aerosol optical over land and estimate the errors involved with such a retrieval (#1). In doing this, conditions were found when aerosols were best sensed by satellite (#3). The retrievals were also used to estimate the magnitude of the backscattering of radiance to space (#4). The errors due to sphericity of an aerosol were beyond the scope of this work, although errors dealing with optical parameters (which are dependent upon particle composition and size distribution) were investigated (#2).

In this study, an existing Adding/Doubling model was used to retrieve optical depths from GOES-8 imagery. Comparisons of the model output were made to the following surface observations: a sun photometer, transmissometer, nephelometers and horizontal visibility reports. The retrievals were for 5 cases (of 7 days or more) during the summer of 1995 over the Eastern U.S. with emphasis over IMPROVE sites. An error budget was calculated and retrievals had an estimated error of $\Delta\tau = \pm(0.05\text{-}0.16)$ for τ from 0.1 to 1.0. The retrieved optical depths were then used to estimate the direct radiative forcing of the aerosols.

1.1.2 Climatology of Eastern United States Haze Events

As the baroclinic zone moves northward in the spring, the Bermuda High begins to build a ridge extending over the East Coast of the U.S. This ridge causes weak circulation patterns and advection of tropical air over the continent. These conditions - higher boundary layer relative humidities, large-scale subsiding air and generally weak winds (Corfidi, 1993) - create an environment conducive to heavy summertime haze outbreaks.

It is interesting to note that the Great Smoky Mountains of Tennessee and the Blue Ridge Mountains of Virginia received their names from naturally occurring haze in those areas. While natural emission of aerosol by vegetation has remained relatively constant over the years, anthropogenic emissions of aerosol has increased by about 1.5 million tons of sulfate per year (a 50% increase) in the Northeastern U.S. between 1940 and 1980 (Husar and Wilson, 1993). The amount of naturally occurring and anthropogenic aerosols make the east a prime area of aerosol studies. Malm et al. (1994)

calculate spatial and temporal aerosol composition trends from 36 IMPROVE sites around the U.S. for a three year period between March 1988 and February 1991. They find that yearly averaged light extinction is 0.12 km^{-1} in the Eastern U.S. whereas values near the "smog zones" of San Francisco and Los Angeles are only half that (0.6 km^{-1}) and values in the Rocky Mountains are a full order of magnitude less than eastern conditions. Therefore, the aerosol retrieval efforts of this study were concentrated in the eastern region of the U.S.

Figure 1.2 shows the seasonal trend and annual average of aerosol fine particulate (particle diameter $\leq$ 2.5 μm) mass for IMPROVE sites in the east. Appalachia is an average of some IMPROVE sites located in the Appalachian Mountains. In each area, the maximum amount of fine particulate aerosol mass occurs during the summer months (June, July, and August). A similar trend is also noticed in the coarse particulate mass (2.5μm < particle diameter (D) < 10 μm), Figure 1.3. Also note that the Washington D.C. site, the only urban measurement, has the worst conditions. The large amount of coarse particles in the winter is most likely due to the trapping of urban pollutants by strong inversions.

Summertime aerosols consist mostly of sulfates (Table 1.2) with additional organic and soil particles. These compositions are largely hygroscopic, that is at high relative humidity the particle size increases due to absorption of water, increasing the aerosol scattering efficiency. Therefore, at high relative humidities, the single scatter albedo is also high. Also, sulfates are chemically stable (Corfidi, 1993) so atmospheric removal mechanisms are limited to gravitational settling or scavenging by rain and

clouds, thus their lifetimes are about 15 days. The retrievals of optical depth in this study were aimed at the summer months in the Eastern U.S. because it appeared to be the area of highest aerosol loading.

1.1.3 Global Importance of Aerosols

Aerosols can directly and indirectly affect the radiative balance of the earth. The direct effect is the scattering of more radiation to space by aerosols, increasing the effective albedo of a region. This effect has been under recent investigation by many researchers because of the anthropogenic aerosol influence and the local potential for reversal of greenhouse gas warming. Because aerosol lifetimes are on the order of weeks, transport is limited, so their cooling effects are regional. The direct effect is studied using box models (Charlson et al., 1991), radiative transfer (R.T.) models (Nemesure et al., 1995; Kiehl and Briegleb, 1993) and even observational studies on surface temperature deviations (Robock, 1988). Because of the variation in the results of these studies, a question is arising on what the magnitude of the direct effect is.

Aerosols also act as cloud condensation nuclei. An increase in aerosols increase the number of cloud droplets which increases the time to onset of drizzle, thereby increasing the lifetime of the cloud. Also, the larger concentration of droplets will also increase the cloud top albedo. These two effects, longer cloud lifetimes and higher albedoes, will increase the solar radiation reflected by clouds, which is the indirect effect (Platnick and Twomey, 1994; King et al., 1995). However, this effect is dependent upon many parameters that are beyond the scope of this work. Therefore, this work only looked at the direct effect of aerosols.

1.2 Purpose and Objectives

The study of aerosols is necessary because they affect the atmosphere by:

1. degrading visibility, which is of interest to the Department of Defense for battlefield preparation and the National Parks Service in protected visual environments.
2. directly and indirectly increasing the reflected shortwave radiation to space, affecting the global radiative balance.
3. having regional affects, because of short atmospheric lifetimes; yet are not accurately mapped globally.

Therefore, this thesis has the following objectives:

1. to retrieve optical depths from GOES-8 imagery using an existing Adding/Doubling radiative transfer model.
2. to estimate any errors associated with the retrieval of optical depth including errors associated with the Adding/Doubling model, GOES-8 satellite instrumentation and assumptions of the aerosol optical properties.
3. to compare retrievals to available surface data sets including: a pyrheliometer, transmissometer, nephelometers, and horizontal visibility reports.
4. to estimate the direct forcing from the retrieved optical depths.

Chapter 2 describes the data sets used in this study. Chapter 3 reviews the theory behind the retrievals while chapter 4 describes how optical depth was retrieved. Results are presented in chapter 5 and summarized and concluded in chapter 6.

Table1.1 - Summary of some previous studies and this study, including sensor, range and estimated error of optical depth and area of retrieval. (NR refers to error not reported).

INVESTIGATOR(S)	SATELLITE/ SENSOR	τ	τ ERROR	AREA
Carlson (1979)	NOAA-3/VHRR	0.2-3.0	NR	Atlantic Ocean
Norton et al. (1980)	SMS-1	0.1-0.6	NR	Atlantic Ocean
Kaufman & Joseph (1982)	Landsat/MSS	0.5-0.8	0.1	Coastline
Fraser et al. (1984)	GOES-7/VISSR	0.1-0.8	0.05-0.18	Eastern U.S.
Kaufman et al (1990)	NOAA-7/AVHRR	0.5-2.5	0.08-0.15	D.C. Area
Behunek et al. (1992)	NOAA-11/AVHRR	0.1-1.4	NR	Kuwaiti Plumes
Fraser (1993)	NOAA/AVHRR	0.2-1.6	0.2	Central Asia
Current Study	GOES-8/Imager	0.1-0.6	0.05-0.16	Eastern U.S.

Table 1.2 - Aerosol compositions (percent by mass) reported by Malm et al. (1993) for three eastern U.S. areas

	AMMONIUM SULFATE (%)	**ORGANIC PARTICLES (%)**	**SOIL PARTICLES (%)**	**OTHER (%)**
Appalachia	**63.5**	26.5	5.1	4.9
Northeast	**52.4**	35.1	3.6	8.9
Washington D.C.	**51.4**	26.1	5.3	17.2

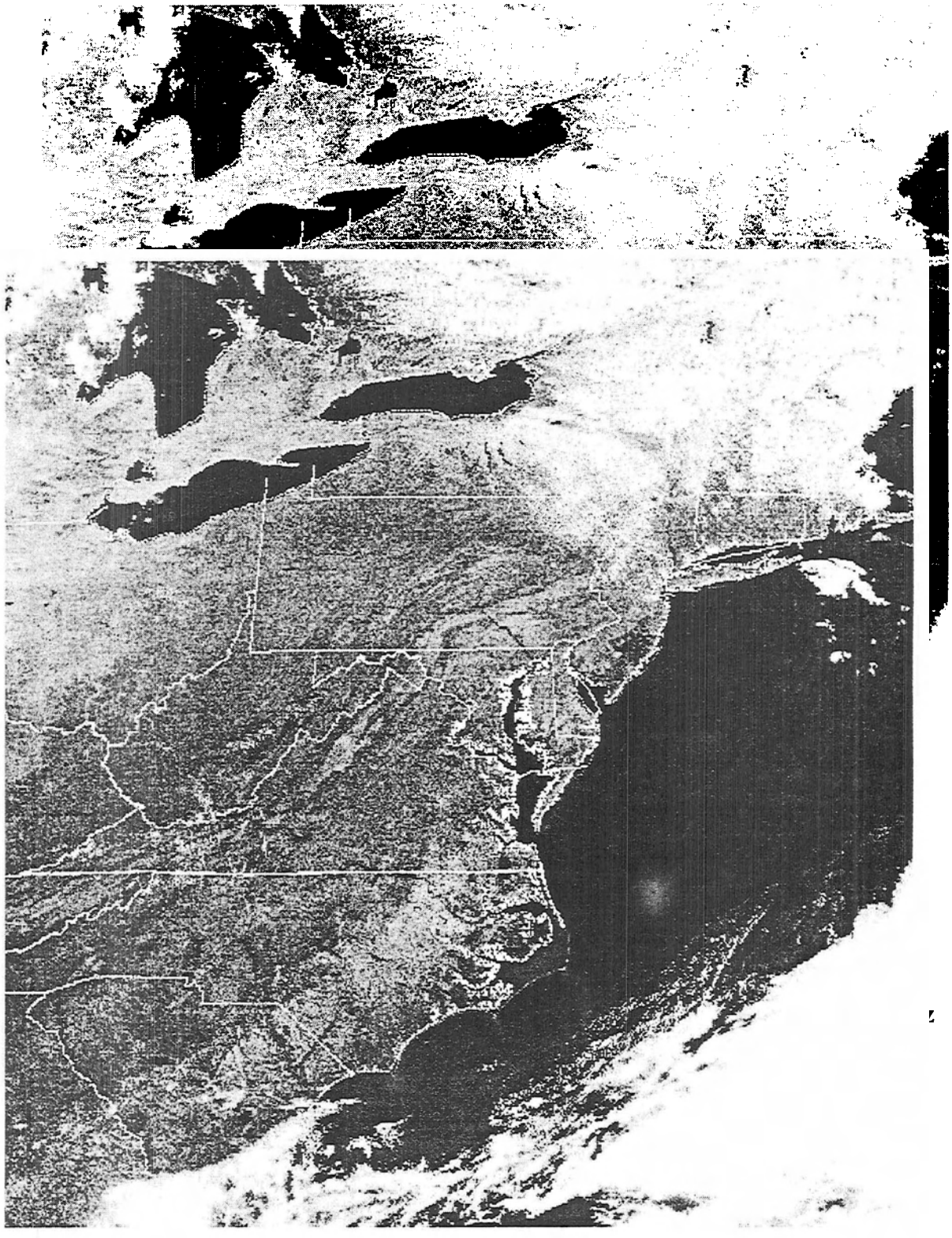

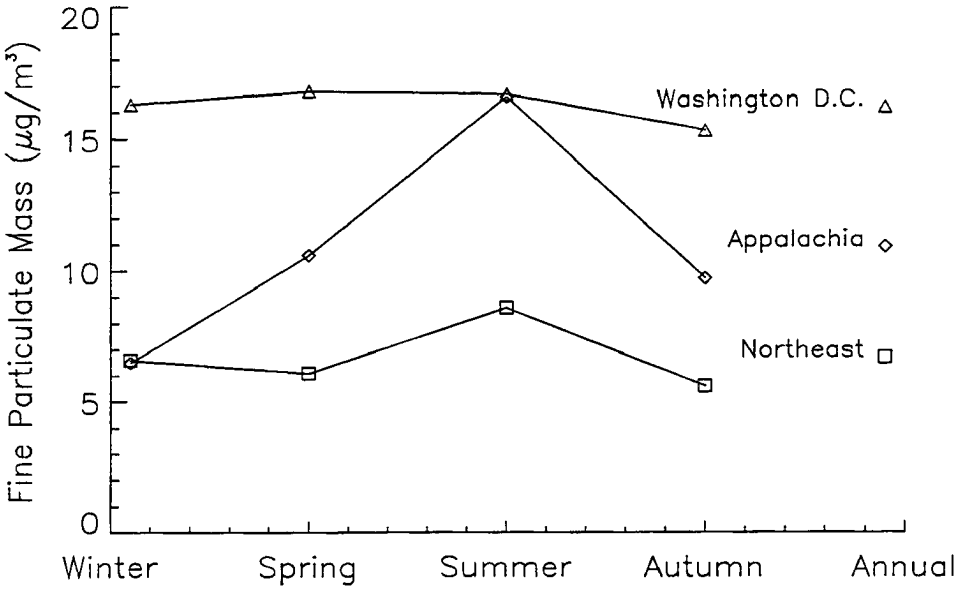

Figure 1.2 - Seasonal trend and annual average of fine particulate (D < 2.5μm) mass for Appalachia, Washington D.C. and the Northeast.

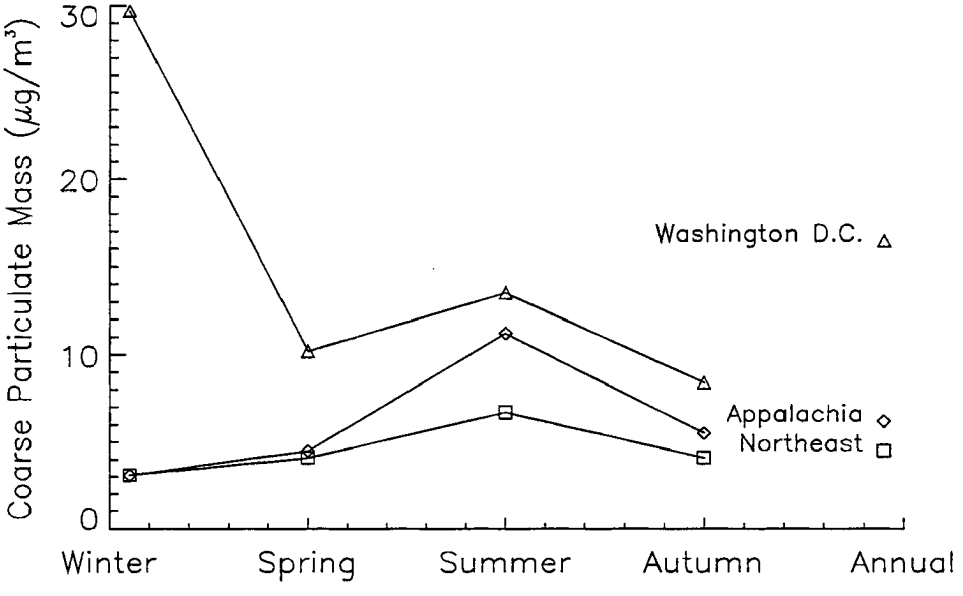

Figure 1.3 - Seasonal trend and annual average of coarse particulate (2.5μm < D < 10μm) mass for Appalachia, Washington D.C. and the Northeast.

Data

The data sets used for this work included space-borne and ground-based platforms. The primary satellite used to retrieve optical depths was GOES-8. Retrievals were compared to numerous surface data sets in chapter 5. These comparison data sets and sensors are discussed below.

Three major differences exist in the data sets: the amount of the atmosphere sampled, the wavelengths of radiation measured and how each instrument senses aerosols.

Figure 2.1 shows relative sampling techniques and volumes of the instruments used in this study. The GOES-8 visible channel detects radiation that is affected by the entire depth of the atmosphere and has a footprint of 1 km^2 at NADIR. Therefore, retrieved optical depths were affected by changes in aerosol structure in the entire column viewed by the GOES-8 Imager. Likewise, the pyrheliometer also views a vertical column of air, although it has a smaller sampling volume (see table 2.1). The other instruments have sample volumes limited closer to the ground. The IMPROVE transmissometer can sample a large part of the boundary layer if the path length is across a valley. The IMPROVE nephelometer and Automated Surface Observing System (ASOS) visibility instrument are limited to surface observations. Not shown is the

human sensor for visibility, the eye. This has a large sampling area (the entire horizon) and is also limited to the boundary layer, because vertical visibility is not measured in clear sky conditions.

Also, there are spectral differences in the instrumentation. Figure 2.2 shows the different spectral intervals of the instruments mentioned above and the gaseous absorption affecting them. The GOES-8 visible channel has a spectral range of 0.55 to 0.75 μm (Menzel and Purdom, 1994) which is largely in an atmospheric window of little gaseous absorption. The pyrheliometer, which also samples a vertical column, has a much larger detection band ranging from 0.3 to 3.0 μm. This range is affected by large absorption bands of water vapor (H_2O) and carbon dioxide (CO_2). Conversely, the IMPROVE instruments are filtered in such a manner to provide them with narrow detection centered at 0.55 μm with a band width of 0.01μm (Molenar et al., 1990). The ASOS instrument and human eye have similar bandwidths and are on the order of the GOES-8 instrument.

The means by which these instruments sense aerosols is discussed below.

2.1 Satellite Data - GOES 8

The GOES-8 satellite has many advantages over its predecessor, GOES-7, for aerosol retrievals. GOES-7 had a non-linear 6-bit digitization, whereas GOES-8 has a linear 10-bit digitization, which allowed for more resolved changes in satellite detected radiance. The signal to noise ratio was improved by a factor of 4, providing higher

confidence of the pixel count. This high quality sensor at geostationary orbit provides visible imagery at 15 minute intervals over the continental U.S.

A large sector of GOES-8 imagery over the Eastern U.S. was archived during the summer of 1995 for morning hours, 12:15 through 15:31z for the purpose of retrieving τ. The sector area was determined by positions of IMPROVE sites. It was later expanded west in July to incorporate another IMPROVE site (the nephelometer at Mammoth Caves National Park) and extended until 20:45z, to include more daylight hours for comparison.

2.1.1 Imager statistics

The GOES-8 imager has five channels in the visible and infrared wavelengths. Table 2.1 shows the bands used and corresponding sub-satellite resolution (SSR). For this research, only channel 1 (the visible) was used for aerosol sensing. The spectral response function of channel 1 is shown in figure 2.3. The sub-satellite instantaneous field of view (FOV) is 1× 1 km for the visible, but due to oversampling in the east-west scan, the SSR is 0.57 × 1.0 km. The resolution in the Eastern U.S. is around 0.73 × 1.3 km due to the curvature of the earth. Also, each scan covers 8km in the north-south, therefore there are eight visible detectors (each with a 1 km^2 FOV), each having its own initial calibration coefficients.

2.1.2 Calibration

The adding/doubling model (described in section 3.1) required reflectance in the calculation of optical depth. Therefore, satellite data (in counts) were converted to radiance, then to reflectance. In flight calibration of the visible sensor was not within the

scope of this work, therefore, the calibration equations and coefficients from the pre-flight calibration were used (available at the World Wide Web site http://climate-f.gsfc.nasa.gov/~chesters/text/ imager.calibration.html). The calibration equation, from digital count (n) to radiance (L_{sat}) is:

$$L_{sat} = mn + b, \tag{2.1}$$

where m is the sensor resolution (0.551 $Wm^{-2}ster^{-1}$) and b is the offset. Each of the eight visible detectors has different response and offset, therefore there are different coefficients for each detector. But, NOAA normalizes each detector to the same detector to simplify calibration and reduce image striping. Reflectance (ρ_{sat}) is then calculated from L_{sat} (Arino et al., 1991) via:

$$\rho_{sat} = \frac{\pi L_{sat}}{F_o \cos\theta_o} \tag{2.2}$$

where F_o is the top of the atmosphere solar irradiance integrated over the sensor response, $F_o = 1627\ W/m^2$. The derivation of equation 2.2 is shown in the appendix. Using equation 2.1, an alternate form of equation 2.2 is:

$$\rho_{sat} = k(mn + b)\sec\theta_o, \tag{2.3}$$

where $k = \pi / F_o$. Therefore, the smallest change in reflectance detectable by GOES-8 is:

$$\frac{d\rho_{sat}}{dn} = mk\sec\theta_o = 0.00106, \tag{2.4}$$

for $\theta_o = 0°$. ρ_{sat} has the unit $ster^{-1}$, so it is not a measure of the albedo, rather it is the specular reflectance. The albedo is the hemispheric integral of ρ_{sat}.

The visible detectors are subject to a change in their resolution, or responsivity, while in orbit due to environmental effects. On earth, in situ sensors can be removed from operation for an amount of time for cleaning and re-calibration, either in the field or laboratory. Most infrared satellite sensors have a blackbody cavity onboard which is used for calibration, but most visible sensors have no such reference. Therefore the calibration coefficients will change an unknown amount during the lifetime of a sensor. This sensor drift has occurred in the visible sensor of GOES-8 by increasing the resolution (increasing m in equation 2.1) (Weinreb, personal communication). In flight calibration can be performed using targets with known reflectances, such as the ocean (Fraser et al., 1984). However, for this study the preflight calibration coefficients were used.

2.2 Surface Observations

Surface data was collected for this work as point validation for the radiative transfer calculations of optical depth. The most direct comparison to the GOES-8 retrieved optical depth is a pyrheliometer, which measures extinction of the solar beam through the depth of the atmosphere. Transmissometer and nephelometer data are available through the IMPROVE network. The transmissometer measures atmospheric extinction, whereas the nephelometer measures atmospheric scattering. Although the nephelometer does not measure extinction, it is still a good point comparison because the majority of hazes on the east coast are scattering aerosols. Also, National Weather Service hourly observations of surface visibility were collected for point comparisons. The following sections describe the data sets in detail.

2.2.1 *ARM site data*

The Baseline Surface Radiation Network (BSRN) collected data from a pyrheliometer as part of the Atmospheric Radiation Measurements (ARM) program during the summer of 1995 in central Oklahoma. Data was received from the BSRN archive for dates May 1 through August 31. The pyrheliometer can provide a ground estimate of optical depth using Beer's Law:

$$L = L_0 e^{-\tau/\mu_o} \tag{2.5}$$

where L is the irradiance at some optical depth τ, μ_0 is the cosine of the solar zenith angle and L_0 is the TOA solar irradiance for the spectral interval and sensor spectral response of the pyrheliometer. This assumes that all light received has been attenuated. So, τ can be calculated by:

$$\tau = -\mu_o \ln\left(\frac{L}{L_0}\right) \tag{2.6}$$

Therefore, using the pyrheliometer, one can find the optical depth of the path between the sun and the instrument. This was used as a verification method for the adding/doubling model.

The pyrheliometer constant L_0 was calculated following the Liou (1980). Taking the natural logarithm of equation 2.5 results in:

$$\ln L_0 = \ln L - m_\theta \tau, \tag{2.7}$$

where $m_\theta = \sec \theta_0$. If the τ is constant over some amount of time, then ln L can be plotted against m_θ and ln L_0 can be solved for as the offset and τ as the slope of the line. This is

called a Langley plot, which is shown in figure 2.5 for the morning of 26 July 1995. The linear regression of this plot has $\ln L_o = 6.979$, or $L_o = 1074\ Wm^{-2}$.

The pyrheliometer was calibrated 29 July 1993 and has a resolution of 1.247 W/m^2. The instrument was stationed at 36.605° N and 97.485° W and the spectral range of the instrument is 0.3 to 3.0 μm.

2.2.2 IMPROVE data

The IMPROVE network consists of about 60 aerosol measuring sites at National Parks (N.P.) around the United States, which are concentrated in the west. Instruments used to monitor the air quality include: transmissometers, nephelometers, aerosol collection instruments and atmospheric state variables such as temperature and relative humidity. The nephelometer and transmissometer were used in this study as a point comparison and relative humidity was used to estimate changes in aerosol optical parameters.

Because the transmissometer and nephelometer are used to calculate the coefficients of extinction (b_{ext}) and scattering (b_{sca}), respectively, it is important to realize their relation to optical depth(τ):

$$\tau = \int_{sfc}^{TOA} b_{ext} dz \tag{2.8}$$

where dz is incremental height and b_{ext} is the extinction coefficient integrated from the surface (sfc) to the TOA. If we assume that aerosols are confined to a well-mixed scattering layer, then equation 2.5 becomes:

$$\tau = b_{ext}\, \Delta z, \tag{2.9}$$

where Δz is the depth of the scattering layer. Therefore, as long as Δz remains somewhat constant in time and b_{ext} is uniform with height, there should be some correlation between b_{ext} measured at the surface and satellite retrieved τ. Because extinction is the sum of scattering and absorption (b_{abs}) then equation 2.6 can be written as:

$$\tau = b_{sca}\Delta z + b_{abs}\Delta z. \tag{2.10}$$

So if $b_{sca} >> b_{abs}$, then b_{sca} should be correlated to τ. From Table 1.1, we see that east coast hazes are composed mostly of sulfates, which are largely scattering aerosols and this condition is satisfied, when relative humidities are high. The east cost IMPROVE sites measured humidities above 65% for all time periods discussed in this study.

Of the 14 IMPROVE sites encompassed by the GOES-8 sector archived for this work, only one site had a transmissometer, which was located at Shenandoah N.P. The transmissometer was operational for the summer of 1995, except for a down period between June 22 and July 12. The transmissometer measures b_{ext} by transmitting a pulsed beam of light (L_o) from a transmitter to a detector. Combining equations 2.4 and 2.6:

$$b_{ext} = \frac{-\ln\left(\frac{L}{L_o}\right)}{\Delta s} \tag{2.11}$$

where Δs is the path length of the transmissometer which is 0.68 km at Shenandoah (Molenar et al., 1990) and here L_o is the transmitted beam radiance and L is the radiance received by the detector. The detected wavelength of the transmissometer is 0.55 μm.

There are three nephelometer sites in the area encompassed by the GOES-8 collection region at: Dolly Sods, West Virginia near the Monongehela National Forest, Great Smoky Mountains N.P., Tennessee, and Mammoth Cave N.P., Kentucky. The

nephelometer measures atmospheric scattering at the wavelength 0.55 μm. Figure 2.4 shows the locations of these sites.

2.2.3 National Weather Service Data

Surface visibility reports were collected for the summer of 1995 from the NWS reporting stations. The Koschmeider equation (Koschmeider, 1924) relates visibility, V, to b_{ext} by:

$$V = \frac{3.912}{b_{ext}}. \tag{2.12}$$

Using equation 2.9 this can be written as:

$$V = \frac{3.912\Delta z}{\tau}, \tag{2.13}$$

which shows again that the scattering depth needs to be constant for any correlation to be found between τ and inverse visibility (V^{-1}). Comparisons of τ to visibility were also limited to how V is measured and reported. Most human measurements are not continuous, but reported in discrete intervals. That is, visibility is measured by the distance to the furthest object visible. This categorizes the measurement to which objects (with known distance from viewer) were seen that day. Also, visibility often has an upper limit; visibility is often truncated above a certain distance.

Retrievals of τ were performed over 21 NWS stations in the Ohio Valley area. A few were ASOS stations which report visibility by measuring the amount of scattered light at the scattering angle of 45°, which has been shown to be proportional to extinction

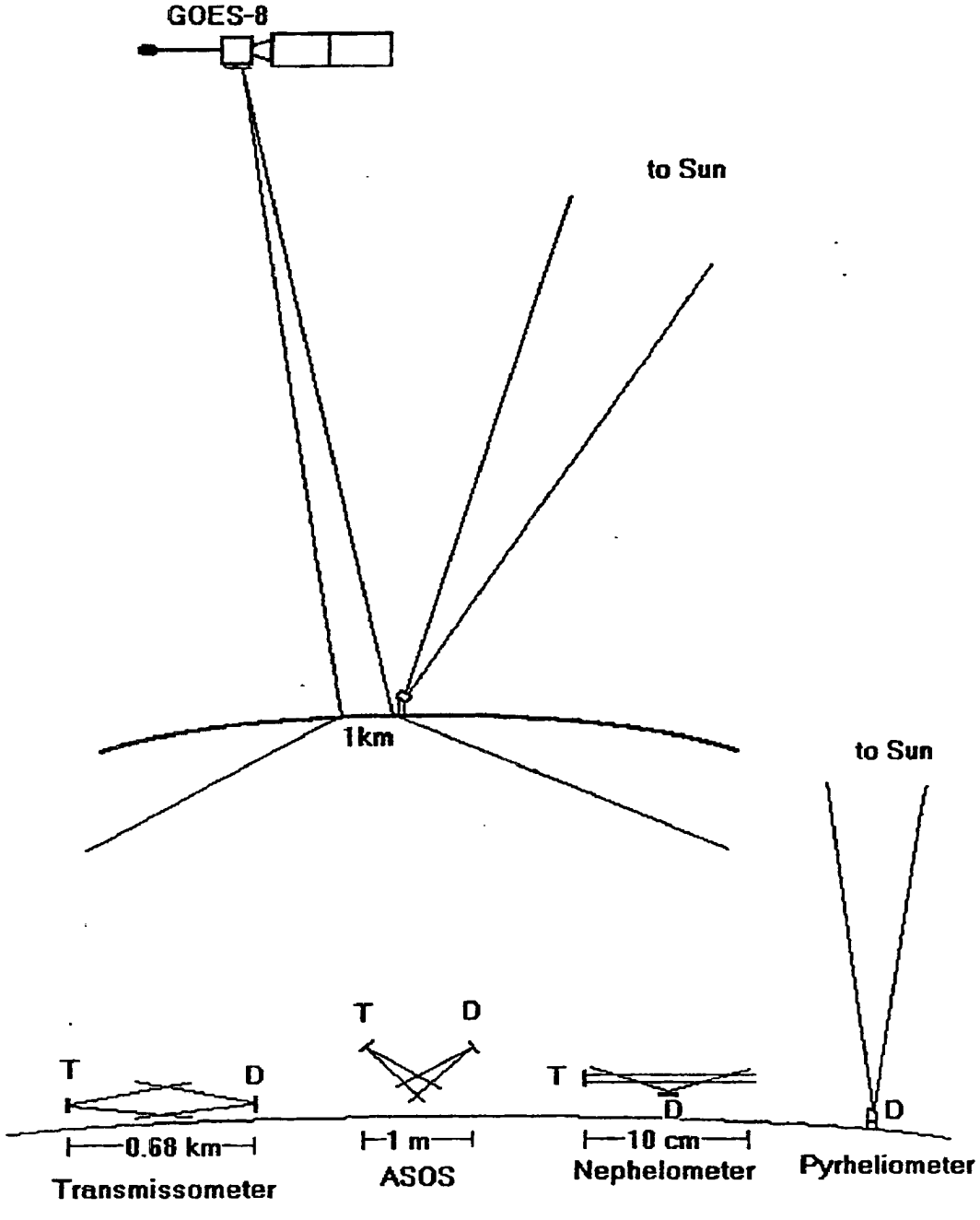

Figure 2.1 - Technique and scales of instrument sampling used in this study: T denotes a transmitter and D a detector.

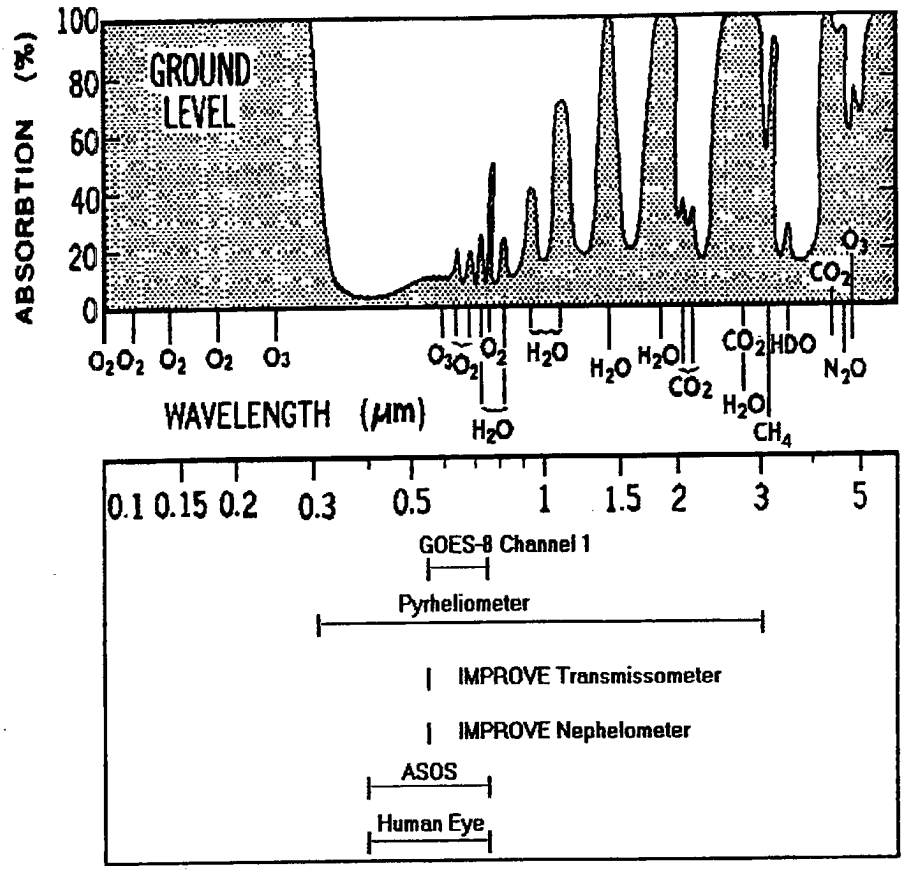

Figure 2.2 - Spectral ranges of instruments used in this study and atmospheric absorption at the ground (graph from Peixoto and Oort, 1992).

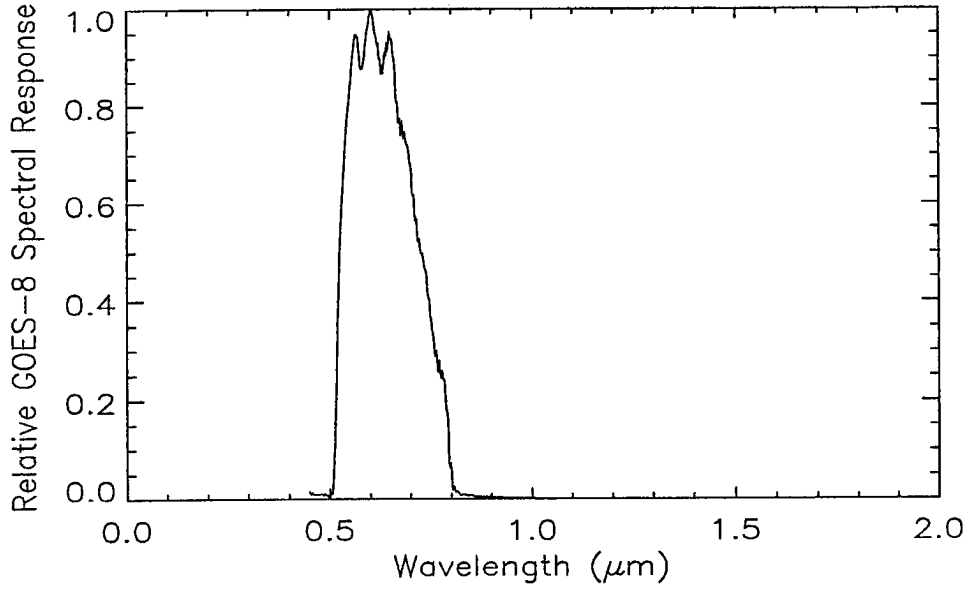

Figure 2.3 - Spectral response function for channel 1 of the GOES-8 Imager.

Figure 2.4 - Location of IMPROVE sites used for surface comparison in this study.

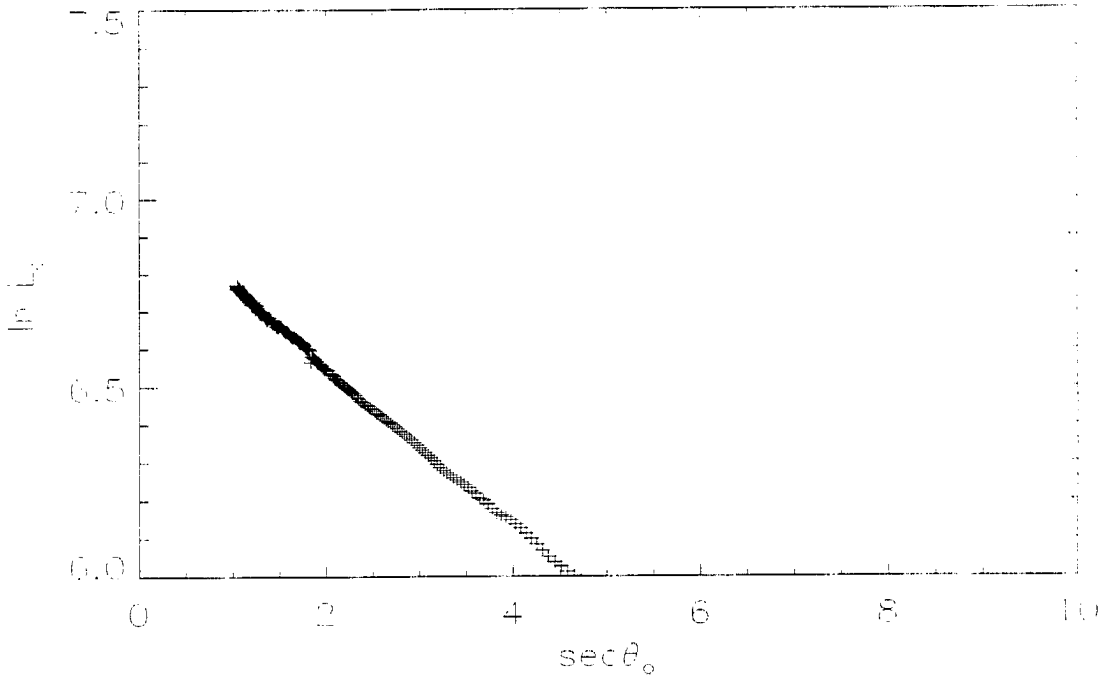

Figure 2.5 - Langley plot used to calculate the pyrheliometer constant.

Theory

This section describes the theory behind the radiative transfer models used to retrieve the optical depths from GOES-8 and calculate aerosol forcing from these retrievals. An adding/doubling model was used to retrieve optical depths and a 2-stream model was used to calculate the aerosol forcing.

3.1 Adding/Doubling Radiative Transfer Model

The shortwave radiance detected by a satellite (L_{sat}) can be thought of as having three components, as in figure 3.1:

$$L_{sat} = L_o + L_a + L_n \tag{3.1}$$

where L_o is the direct component (solar radiation transmitted through the atmosphere and transferred from the surface into the satellite FOV), L_a is the atmospheric component (solar radiation reflected by atmospheric constituents into the satellite FOV) and L_n is the adjacency effect (radiation reflected by a neighboring pixel, then scattered into the satellite FOV). For a pristine atmosphere (few aerosols), $L_o >> (L_a + L_n)$ because scattering is at a minimum. In which case, the radiance received at satellite is primarily a function of the surface reflectance. However, as the aerosol optical depth increases, the

($L_a + L_n$) component becomes larger. This will brighten or darken the pixel, depending on whether the aerosol is a scatterer or an absorber. According to Kaufman (1987), L_a is the dominant term over dark surfaces in a hazy atmosphere.

The adding/doubling, multiple scattering model used in this study was developed by Greenwald and Stephens (1988), hereafter referred to as the A/D model. It was designed to perform sky color, intensity and object contrast simulations (Tsay et. al., 1991). After some modifications by Graeme Stephens and Jan Behunek, it currently calculates optical depth from satellite detected reflectances, sun-earth-satellite geometry, and aerosol optical properties. The following is an overview of the model and its application to aerosol optical depth retrieval. For a more rigorous description, see Greenwald and Stephens (1988). This method has previously been used to retrieve optical depths from smoke plumes during the 1991 Kuwaiti oil fires (Behunek et al., 1993).

3.1.1 Theory

The equation of radiative transfer for a plane-parallel, scattering atmosphere is

$$\mu \frac{dL(\tau;\mu,\phi)}{d\tau} = -L(\tau;\mu,\phi) + \frac{\omega_o}{4\pi}\int_0^{2\pi}\int_{-1}^{1} P(\tau;\mu,\phi,\mu',\phi')L(\tau;\mu',\phi')d\mu' d\phi' + J(\tau;\mu,\phi) \tag{3.2}$$

where J, the "pseudo-source" term, is

$$J(\tau;\mu,\phi) = \frac{\omega_o}{4\pi}F_o P(\tau;\mu,\phi,-\mu_o,\phi_o)e^{-\tau/\mu_o} + \frac{\omega_o}{4\pi}F_o A_s P(\tau;\mu,\phi,\mu_o,\phi_o)e^{-(2\tau^*-\tau)/\mu_o} \tag{3.3}$$

L is radiance, $\mu=\cos\theta$, θ and ϕ are geometric angles (see figure 3.2), τ is optical depth, ω_o is the single scatter albedo, P is the phase function, F_o is the solar irradiance at the TOA, A_s is the specular reflectance and τ^* is the optical depth of the atmosphere. The first term in equation 3.2 and the second term in equation 3.3 represent L_o. The second term in equation 3.2 and the first term in equation 3.3 represent the L_a term. L_n is not accounted for by this model. J is a pseudo-source term because there is no source for visible radiation in the atmosphere, but the aerosol scattering of the direct solar beam can act as a source. The phase function used is the Henyey-Greenstein phase function:

$$P(\cos\Theta) = \frac{(1-g^2)}{(1+g^2-2g\cos\Theta)^{3/2}} \tag{3.4}$$

where Θ is the scattering angle defined by:

$$\cos\Theta = \mu\mu' + \sqrt{1-\mu^2}\sqrt{1-\mu'^2}\cos(\phi'-\phi) \tag{3.5}$$

and μ and ϕ and their primed terms are scattering angles as denoted in figure 3.2 and g is the asymmetry parameter.

By expanding the phase function using Legendre polynomials, the intensity using Fourier series and using a Gaussian quadrature approximation, equation 3.2 is transformed into a series of matrix equations that can be solved using the adding/doubling technique. The end product is a 32-stream radiative transfer model which calculates the theoretical satellite observed reflectance (ρ_{sat}), at 16 satellite zenith angles (θ) due to an aerosol layer with the optical parameters g and ω_o at the sun-earth-satellite geometry (μ_o, ϕ_o, ϕ) and a background surface reflectance (ρ_{sfc}).

Optical depth was then retrieved by iteratively solving the model (figure 3.3). By using the known latitude, longitude and time of the image, the scattering angles (μ, ϕ, μ', ϕ') were calculated. A background reflectance was found through an algorithm that used the darkest pixel over a time series of images, which is described in section 4.2. Then assuming some g and ω_o and starting with an initial guess for τ, a theoretical satellite-detected reflectance was calculated. This was then compared to the observed satellite reflectance, and a new estimate of τ was calculated from the difference in reflectances, iteratively solving for $\tau_{A/D}$.

Because the model used a background reflectance as a comparison to reflectance of haze, it only calculated the difference in τ between the background and haze satellite images due to an increase in τ from a layer of aerosols with the assumed optical properties. The surface reflectance used is not the actual surface reflectance, rather the darkest pixel at a location measured during the case. This contained some background aerosol signal. Because the optical depth is a difference, the nearly constant Rayleigh component and background aerosol optical depth are subtracted out.

3.1.2 Sensitivity Study

The satellite detected radiance, and reflectance, is then a function of all the input parameters. This section will look at the ability to measure changes in optical depth with varying solar zenith angle and aerosol optical parameters. A control run was calculated for a range of τ (0.05 to 1.0) and surface reflectance (0.035 to 0.08) and other parameters specified in table 3.1. The ρ_{sfc} range was determined from the range of satellite measured ρ_{sfc} of a large image over the Shenandoah area. The theoretical satellite-detected

reflectance calculated by the A/D model is $\rho_{A/D}$. The results are shown in figure 3.4. Figure 3.4a shows $\rho_{A/D}$ versus τ. Each line approaches its surface reflectance as τ goes to zero. It can be seen that the satellite observed reflectance should increase with τ for this specific aerosol. Also, as ρ_{sfc} increases, the slope of the lines decrease, showing less sensitivity to τ over brighter surfaces. These trends are also noticed in figure 3.4b which is the same data, only displayed differently. Here, the abscissa is surface reflectance and the ordinate is the estimated satellite detected reflectance less the surface reflectance (the increase of detected reflectance from the surface reflectance, $\Delta\rho$). Each line is for a different optical depth. As ρ_{sfc} increases, $\Delta\rho$ decrease for constant τ. The convergence of these τ contours is more noticeable in figure 3.5 where there is little change in $\Delta\rho$ between ρ_{sfc} of 0.16 and 0.25. This condition is called the critical albedo region, ρ_c, because for this range of surface reflectances, there is no measurable change in reflected radiance for any optical depth, rendering the haze undetectable. ρ_c is dependent upon the sun-earth-satellite geometry, aerosol optical properties and surface reflectance (Kaufman, 1987). ρ_c was not encountered in this study because the eastern region of the U.S. has relatively low ρ_{sfc} values and does not reach the critical albedo range for the aerosols investigated ($\omega_o > 0.95$).

Values for the control run and variations of certain parameters are listed in table 3.1. Only one parameter was varied at a time while control values were used for other parameters.

Table 3.2 shows the results of varying the parameters. The values shown are the average resolution of τ for optical depths from 0.0 to 1.0. For example, the control run

parameters allow a resolution of τ to 0.0116 at $\rho_{sfc} = 0.034$. Resolutions are lower for smaller g and higher ω_o, whereas the resolution as a function of θ_o varies. Figure 3.6 shows $\Delta\rho$ for $\tau = 0.1$, 0.3 and 0.9 at $\rho_{sfc} = 0.045$ (70 counts) as a function of θ_o. This shows that the best sensitivity occurs around θ_o of 65 to 70°, or about 8:00 a.m. local time (12:00z) over the east coast. Not only does the resolution change, but also, the critical albedo region changes. This is noticed in the change in resolution between the two reflectances (the difference column in table 3.2). Larger differences mean that sensitivity is decreasing more with respect to ρ_{sfc} and the ρ_c region is approaching lower ρ_{sfc}. So smaller zenith angles, lower ω_o or higher g decrease the ρ_c.

From this sensitivity study, it can be seen that the most detectable aerosols are highly scattering (larger ω_o), smaller particles (lower g) at $\theta_o \sim 65$-70°. These conditions allow for the most radiation to be scattered toward the satellite. Retrieving an optical depth then requires an assumption of the optical parameters. The error in this assumption is discussed in section 5.2. The parameters not varied above were model parameters held constant and geometric angles that did not change (angles for a geostationary satellite). Figure 3.7 shows the sensitivity graph for the optical properties used in this study and sun-earth-satellite angles characteristic of Shenandoah in mid-morning.

3.2 Error Budget

This section attempts to estimate the magnitude of errors associated with the retrieval of aerosol optical depth using the A/D model described above. Rodgers (1990) and Arino et al. (1991) define similar categories of retrieval errors, which were also used

in this study: sensor, atmospheric and surface errors. Another source of error was in the assumption of the aerosol optical properties g and ω_o. In the error discussions below, errors were estimated from separate retrievals of τ for identical 236 × 236 pixel images over the Shenandoah area (figure 3.8), which provided a wide range of surface reflectances. Errors are calculated as the difference between a control retrieval and a retrieval made using the change mentioned (e.g., change in ω_o, sensor calibration, etc.). Whereas the sensitivity study showed what type of aerosol and solar zenith angle was most detectable, this section discusses errors caused by noise and assumptions of optical parameters. Errors are estimated separately for each parameter.

3.2.1 Sensor Error

The sensor error includes digitization of an analog signal, calibration changes and inaccurate satellite navigation. The 10-bit digitization of the GOES-8 Imager allows 1.063×10^{-3} as the smallest detectable change in reflectance (0.551 $Wm^{-2}ster^{-1}$). A one count change in observed radiance results in a mean optical depth difference ($\overline{\Delta\tau}$) of 0.02.

The calibration of satellite sensors is performed in a laboratory before launch. These preflight calibration coefficients are valid for the time the sensor is in the lab. Otherwise, the sensor is subject to change in responsivity due to collection of dust during storage, the stresses of launch and collection of extraterrestrial dust on the optics. This change in response leads to an error in the calculation of the surface reflectance and satellite detected reflectance, which propagates an error in the retrieved optical depth. Therefore, multiple runs of the A/D model were performed using different sensor gains of

a 1, 5, 10 and 15% change in sensor responsivity. Table 3.3 summarizes the results for these differences, where $\overline{\Delta\tau}$ is the average difference and the last column is percent difference in $\overline{\Delta\tau}$. It can be seen that by decreasing the responsivity, calculated reflectances will decrease which lead to smaller optical depths and the negative change. Also, the percentage difference in calibration is magnified in the percentage change in τ.

Navigation error is the error associated with a pixel representing the same earth location between two images. GOES-8 uses a three-axis stabilized system to minimize movement and drift of the orbit. Menzel and Purdom (1994) quote the error to be near ±4 pixels during daylight hours. Although in the retrieval of τ, images were manually aligned to be within ±1 pixel. Table 3.4 summarizes the differences in τ due to satellite-navigated and manually aligned retrievals. The error in satellite-navigated retrievals was calculated by comparing two retrievals: with and without manual alignment data. The manual alignment error was calculated by assuming a 1 count offset error in the manually aligned data. The major difference in the two methods is that the manual alignment leads to smaller standard deviations (σ). The process of manual alignment is described in section 4.2. The change in τ for the image is relatively small, but the manual-alignment retrieval has less error (smaller σ) than the satellite-navigated retrieval.

3.2.2 Surface Error

Land and ocean do not reflect solar radiation uniformly with respect to wavelength or geometry. This causes error for those estimating surface albedoes from satellite (Arino et al., 1991), but did not affect the A/D model retrieval. The bi-directional reflectance function (BDRF) is the dependence of the reflectance of a surface

on the geometry of the reflecting surface with respect to the source and sensor. In retrieving τ for this study, cases were limited to 10 days to minimize the change in solar declination angle during the case, minimizing the change in θ_o. Also, ρ_{sfc} was determined from images from the same time of day, also limiting the change in θ_o. Therefore, the reflectance in both cases is for similar angles of the BDRF. Since the geometry does not change, the BDRF of the surface is not a factor.

Spectrally, the amount of reflected solar radiation changes. But this study was limited to the spectral range of the GOES-8 Imager. Therefore the optical depth retrieved is for the wavelength band of channel 1 (0.55 - 0.75μm).

Another surface effect was the contrast reduction (blurring) or adjacency effect. It is the scattering of light reflected from the surface from outside the field of view of the satellite, L_n in equation 3.1. The effect of aerosols on a surface discontinuity, such as a coastline or lake, is to blur the demarcation. Radiation is reflected by the brighter surface, and scattered into the field of view by aerosol over the darker surface. The horizontal extent (or range) of this blurring effect is dependent upon the optical depth and difference in reflectance between the dark and light surface (Mekler and Kaufman, 1980). Kaufman and Joseph (1982) calculate the range to be less than 2 km for most cases of aerosol properties. Therefore, the adjacency error caused some noise for inhomogeneous areas, but was not quantified here.

3.2.3 Atmospheric Error

Background images were created by compositing multiple images with the same sun-earth-satellite geometry. As mentioned above, composites were made using the same

time of day for each case. A cloud with sub-pixel resolution (less than 1.0 × 1.0 km), e.g. popcorn cumulus, will brighten the pixel, but not enough to be identified as a cloud. This corrupt pixel could be used in the composite or retrieval image and cause noise. Also, thin cirrus clouds can affect an image in a way that is difficult to distinguish from aerosol. These effects were treated as noise in section 4.4.

There are some gaseous absorption bands in the visible range that affect the visible sensor aboard GOES-8. Water vapor has a band centered at 0.72 μm, O_2 at 0.69 and 0.76 μm, NO_2 from 0.3 to 0.55 μm (Houghton, 1985) and molecular oxygen at 0.77μm (Kidder and Vonder Haar, 1995). Oxygen is well-mixed in the atmosphere and the nitrogen dioxide band is in the wing of the visible sensor (see figure 2.3). Therefore, the water vapor band is the only gas that would affect the retrieval of τ, and is accounted for as noise in the retrieval.

3.2.4 Aerosol Error

Because the source and composition of the aerosols were unknown, the optical properties were assumed. The same values were used in all of the subsequent case studies and comparisons, because no further information were known about the aerosol. The values used in this study were $\omega_o = 0.956$ and $g = 0.75$ (section 4.3).

The asymmetry parameter was varied from -5% through 5% of 0.75 (the value used in retrievals in chapter 4), a summary of which is in Table 3.5. τ decreases as g increases because the increased amount of forward scatter leads to less radiance reflected toward the satellite. The single scatter albedo also was varied from -5% to 5% of 0.956, and is likewise summarized in table 3.6. The magnitude of error here is larger than that

of the asymmetry error. As mentioned in section 3.1.2, an increase in ω_o means more scattering, thus requiring less aerosol to reflect energy to the satellite which decreases the retrieved τ.

Aerosol optical parameters vary with relative humidity of their environment. Hygroscopic aerosols absorb water vapor, increasing their size and decreasing the percent by mass of optically absorbing media (elemental carbon). This increases ω_o as well as g. Assuming an aerosol composition and size distribution allows the estimation of this change. This was performed by d'Almeida et al. (1991) whose results for an average continental atmosphere are presented in figure 3.9. These values were also used in a second set of retrievals over IMPROVE sites (section 5.2.2).

3.2.5 Summary

Figure 3.10 summarizes the errors described above for a range of τ. ΔL refers to the digitization error of the Imager sensor (in reflectance, mc = 1.06×10^{-3}). Optical parameter errors were estimated from likely ranges of g (0.7125 to 0.7825) and ω_o (0.946 to 0.966). This range of the optical parameters was chosen by the ranges of optical parameters in previous studies of optical properties (section 1.1.1 and table 4.3). The total error line results from summing the squares of the errors. The calibration error (ΔL_e) is for a 5% error. In general, τ can be retrieved $\pm$(0.05-0.16) for optical depths ranging 0.1 to 1.0.

If the relative humidity were known, this would lessen the uncertainty in the optical parameters. Also by recalibrating the instrument by using a known surface reflectance to $\pm$1%, the error budget becomes that shown in figure 3.11. For this case, the

largest contributors to error are the uncertainty in optical parameters and overall error is reduced to ±(0.05-0.09).

These figures represent bias errors which only increase or decrease the retrieved τ if corrected. Not included in figures 3.10 and 3.11 are the random noise effects due to navigation, sub-pixel cumulus, thin cirrus and variable water vapor absorption, which can increase or decrease a retrieved τ. These are discussed in section 4.4.

3.3 The Direct Effect of Aerosols on Climate

3.3.1 Theory

Direct radiative forcing due to tropospheric aerosols, ΔF [Wm^{-2}], was calculated according to Nemesure et al. (1995):

$$\Delta F = F_{sw}\uparrow(\text{TOA, background aerosol}) - F_{sw}\uparrow(\text{TOA, hazy day}) \qquad (3.6)$$

where $F_{sw}\uparrow$ is the outgoing shortwave radiative flux at the TOA for a clear day and a hazy day. This causes forcing to be negative because aerosols generally increase the local albedo.

Charlson et al. (1991) derives a simplified box model that aides in the general understanding of the direct effect, ΔF:

$$\Delta F = -\frac{1}{2} Q_o T^2 (1 - A_c)(1 - R_s)^2 \beta\tau \qquad (3.7)$$

where Q_o is the solar constant (1370±10 Wm^{-2}), T is the fractional transmittance of the atmosphere, A_c is the fractional cloud coverage, R_s is the surface albedo and β is the average upscatter fraction defined by:

$$\beta = \frac{1}{4\pi}\int_0^1\int_0^1\int_0^{2\pi} P(\mu,\phi,\mu_o)\,d\phi\,d\mu\,d\mu_o \qquad (3.8)$$

where P is the phase function of the aerosol. β represents the average value of the fraction of radiation reflected away from the earth during a day. The negative sign in equation 3.7 denotes that aerosols cause a cooling, and ½ because only ½ the earth receives the suns energy at any time. Using the approximate values $T \approx 0.76$, $\beta \approx 0.29$, $A_c \approx 0.61$ and $R_s \approx 0.15$ (Charlson et al., 1991), equation 3.7 reduces to:

$$\Delta F = -32\tau \qquad [W\ m^{-2}]. \qquad (3.9)$$

Equation 3.9 is dependent upon the parameters in equation 3.6, therefore the forcing is linearly dependent upon the aerosol optical depth, for constant β, T, A_c and R_s. So, an increase in transmittance or β or a decrease in cloudiness or surface albedo will increase the aerosol forcing. An increase in T allows more radiation to reach the aerosol layer, allowing more to be reflected upward. Likewise, an increase in β will reflect more radiance away from the earth. An increase in clouds will decrease the amount of radiance reaching an aerosol layer, decreasing ΔF. For a brighter surface (higher R_s), the increase in outgoing flux will be less than for a dark surface so ΔF is decreased. Charlson et al. (1991) then estimate the global distribution of forcing using a global, three-dimensional meteorological/chemical model for sulfate aerosols at 10° × 10° resolution. Their estimated global average forcing is -0.9 W m^{-2}, with most of the forcing in the Northern

Hemisphere. Equation 3.9 also shows that the forcing calculation is sensitive to the estimated amount of aerosol:

$$\frac{d(\Delta F)}{d\tau} = 32. \quad [W\ m^{-2}] \tag{3.10}$$

This shows that any estimates of the direct effect are sensitive to the estimated global distribution of aerosols. Another study, performed by Kiehl and Briegleb (1993), uses a δ-Eddington R.T. and 3-D diagnostic model to calculate the global distribution of shortwave forcing for an aerosol. Their estimate of the global impact is -0.54 W m^{-2}, much less than the amount from Charlson et al. (1991). Kiehl and Briegleb (1993) estimate that there could be as much as a 10% variation in forcing due to uncertainty in aerosol composition or size.

3.3.2 2 Stream Radiative Transfer Model

A 2-stream model, provided by Graeme Stephens, was used to calculate the excess shortwave radiation escaping to space due to the aerosol amount. The model is presented by Fu and Liou (1992) and has been modified by Graeme Stephens to incorporate 2 more shortwave bands. It currently has 6 bands in the shortwave region (Stephens, 1995) and uses correlated k-distribution to calculate transmission functions. It has also been used in research by Stephens and Gabriel (1996) and Harrington et al. (1996). This study used the same optical parameters to calculate ΔF that were used to retrieve τ.

Table 3.1 Adding/Doubling control parameter values and variations for the sensitivity study.

VARIABLE	g	ω_o	θ_o	θ	ϕ_o	ϕ
Control Value	0.75	0.956	45°	45°	354°	315°
Variations	0.7	0.99	15°	None	None	None
	0.8	0.97	30°			
		0.90	60°			
			75°			

Table 3.2 - Resolution of τ retrievals for ρ_{sfc} = 0.034 and 0.077 (GOES-8 count = 60 and 100, respectively) for varying values of A/D model parameters.

ρ_{sfc}	0.034	0.077	DIFFERENCE
Control	0.0116	0.0137	0.0021
θ_o = 75°	0.0112	0.0149	0.0037
= 60°	0.00943	0.0112	0.0018
= 30°	0.0149	0.0185	0.0036
= 15°	0.0192	0.0243	0.0094
g = 0.70	0.00971	0.0114	0.0017
= 0.80	0.0149	0.0182	0.0033
ω_o = 0.99	0.00990	0.0112	0.0013
= 0.97	0.0109	0.0126	0.0007
= 0.90	0.0149	0.0208	0.0059

Table 3.3 - Average and percent error in τ from errors in the sensor responsivity.

RESPONSIVITY DECREASE (%)	$\overline{\Delta\tau}$	$\frac{\overline{\Delta\tau}}{\tau}$ (%)
1	-0.0122	-4.12
5	-0.0281	-10.2
10	-0.0474	-17.5
15	-0.0658	-24.4

Table 3.4 - Mean difference and standard deviation (σ) of satellite navigated and manually aligned τ retrievals.

	$\overline{\Delta\tau}$	σ
Satellite Navigated	-0.00470	0.172
Manually Aligned	-0.00898	0.144

Table 3.5 - Average and percent error in τ from errors in asymmetry parameter (g).

g	Δg (%)	$\overline{\Delta\tau}$	$\overline{\Delta\tau}/\tau$ (%)
0.7875	5	0.0564	24
0.7725	3	0.0316	13
0.7575	1	0.0107	4.6
0.75	0		
0.7425	-1	-0.00746	-3.1
0.7275	-3	-0.0231	-9.7
0.7125	-5	-0.0368	-15

Table 3.6 - Average and percent error in τ from errors in single scatter albedo (ω_o).

ω_o	$\Delta\omega_o$ (%)	$\overline{\Delta\tau}$	$\overline{\Delta\tau}/\tau$ (%)
0.999	4.5	0.00894	15
0.9847	3	-0.0130	12
0.9656	1	-0.0106	4.5
0.956	0		
0.9464	-1	0.0145	6.4
0.9273	-3	0.0460	20
0.9082	-5	0.0873	40

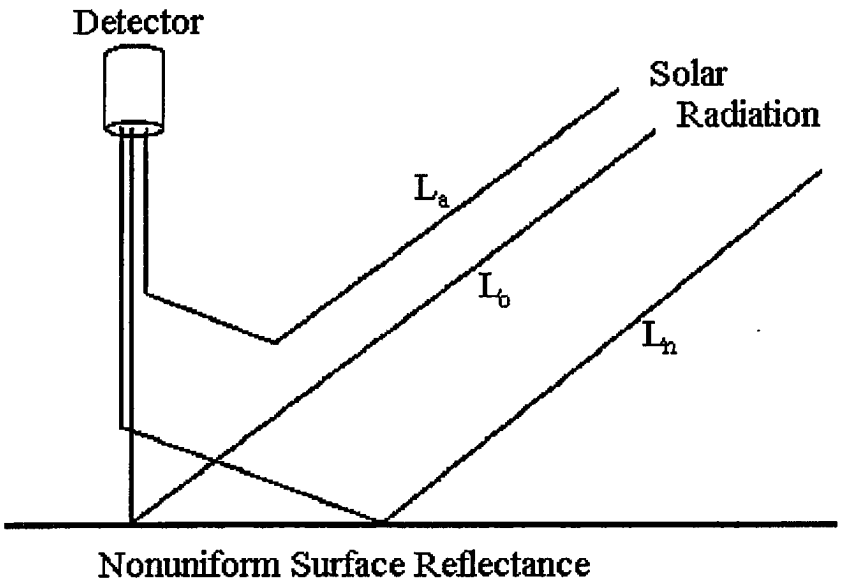

Figure 3.1 - Components of satellite detected radiance (from Kaufman, 1984).

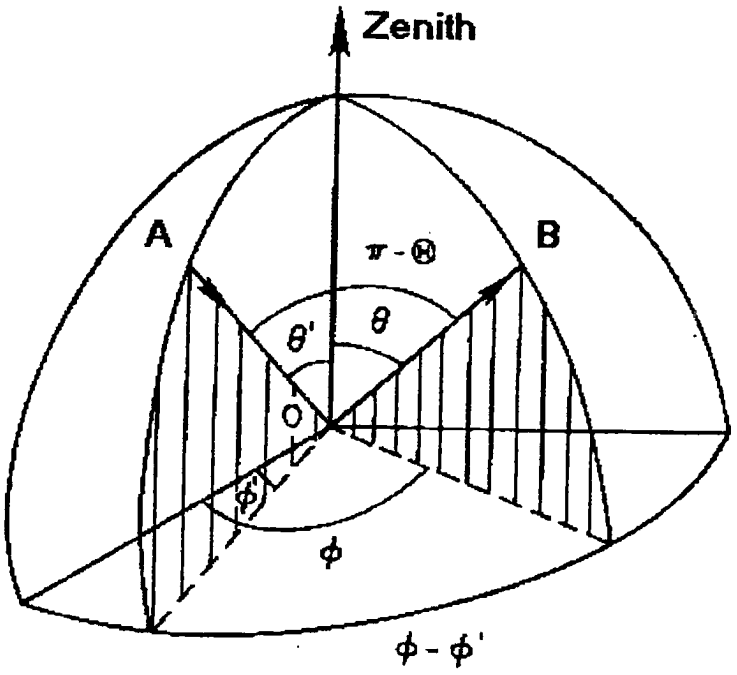

Figure 3.2 - Geometric angles used in the Adding/Doubling Model (from Liou, 1980).

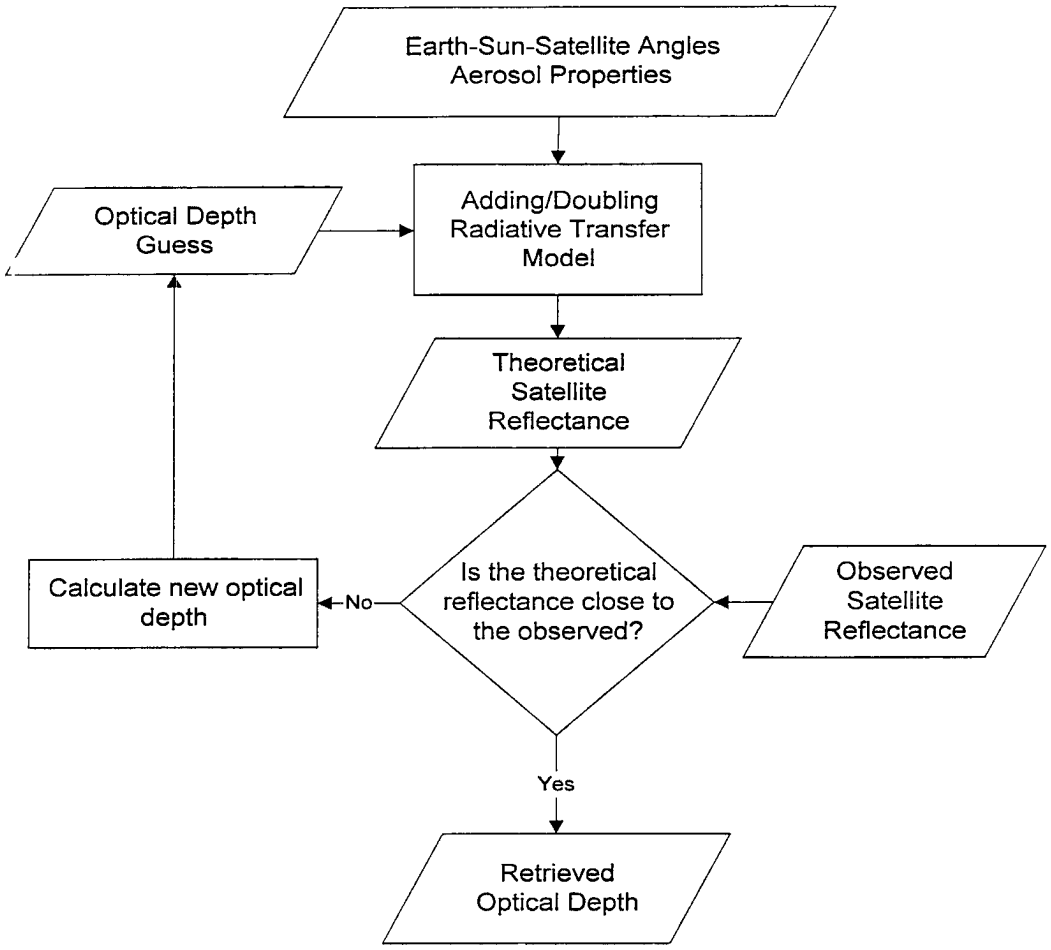

Figure 3.3 - Flowchart for iteratively retrieving optical depth.

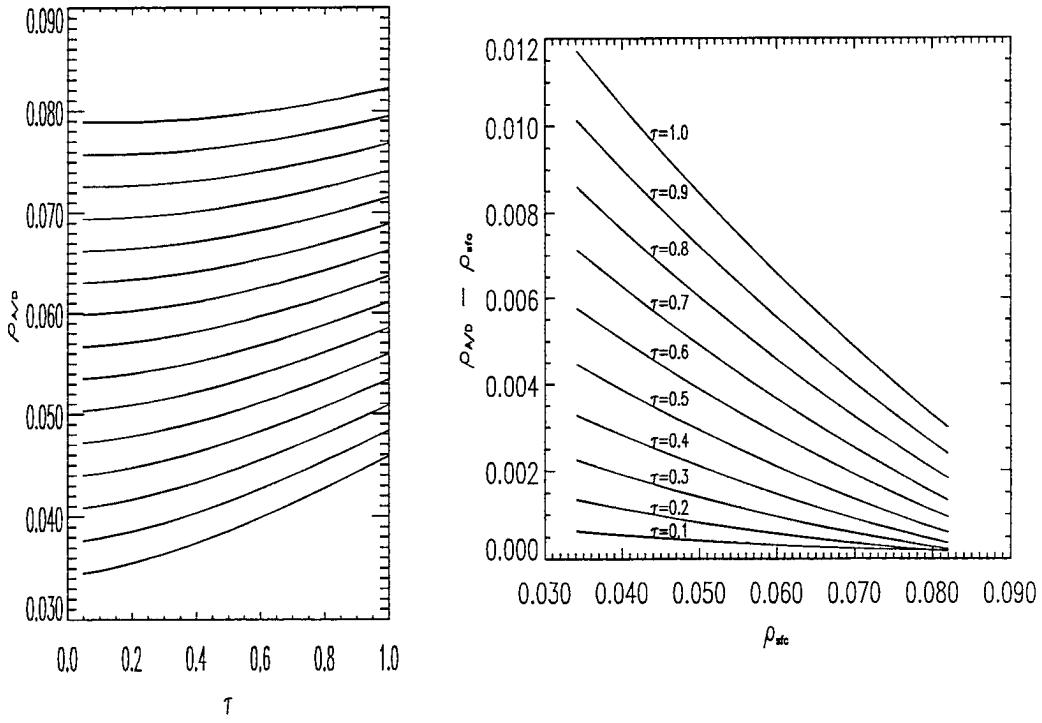

Figure 3.4 - a) Satellite detected radiance as a function of optical depth for different surface reflectances using control values from table 3.1. b) Increase in apparent reflectance as a function of surface reflectance for varying optical depths.

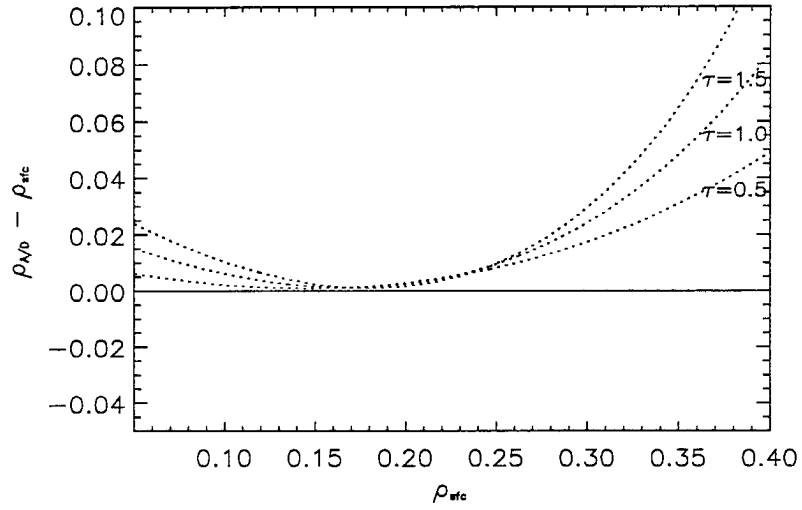

Figure 3.5 - Increase in apparent reflectance as a function of surface reflectance. This shows the critical albedo range between 0.15 and 0.28.

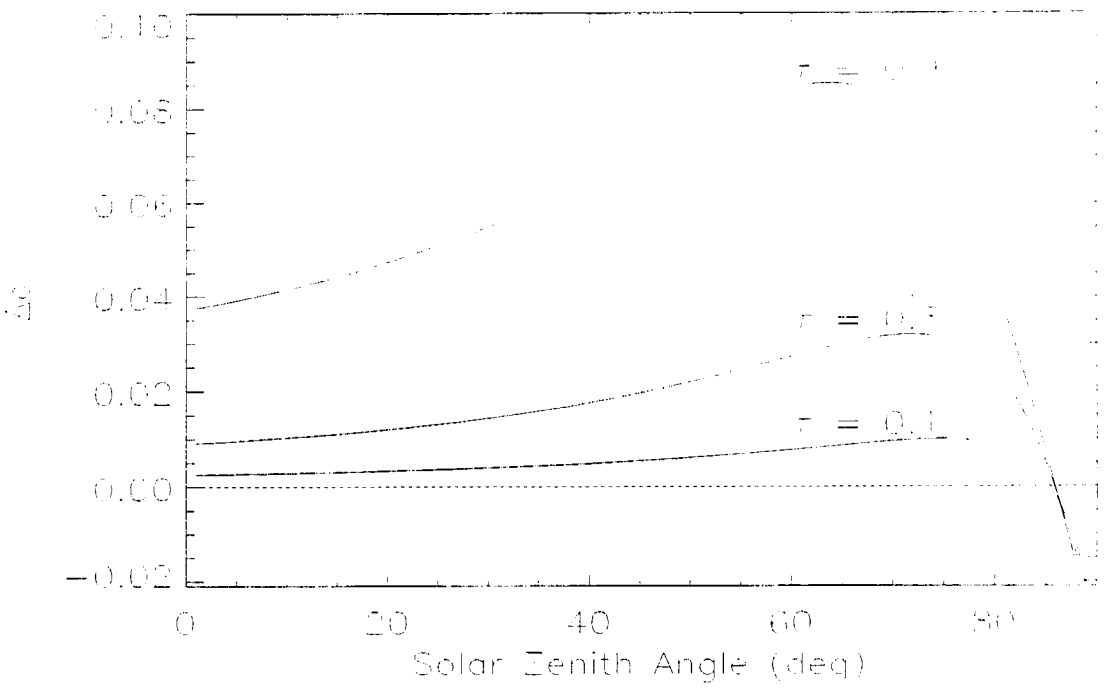

Figure 3.6 - Model calculated reflectance for varying θ_o and optical depths for a surface reflectance of 60 GOES-8 counts (dashed line).

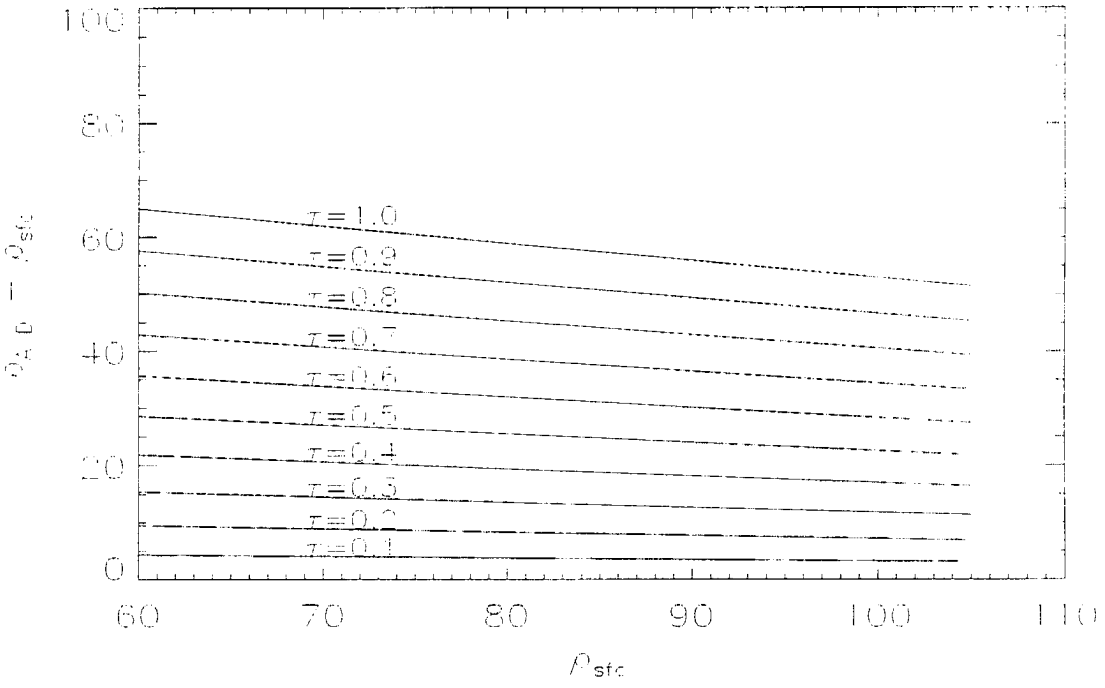

Figure 3.7 - Sensitivity graph for the Shenandoah area in mid-morning.

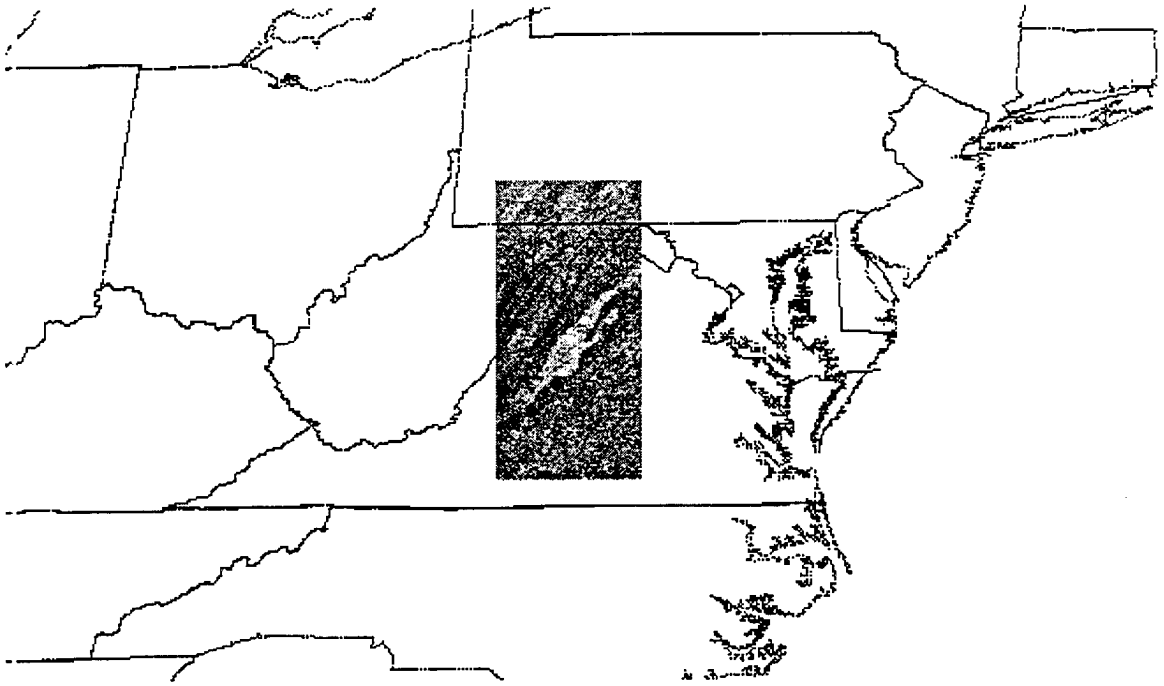

Figure 3.8 - GOES-8 image for the Shenandoah region on 20 May 1995 at 13:31z (9:31 EDT) used for error calculations, enhanced to show the land features.

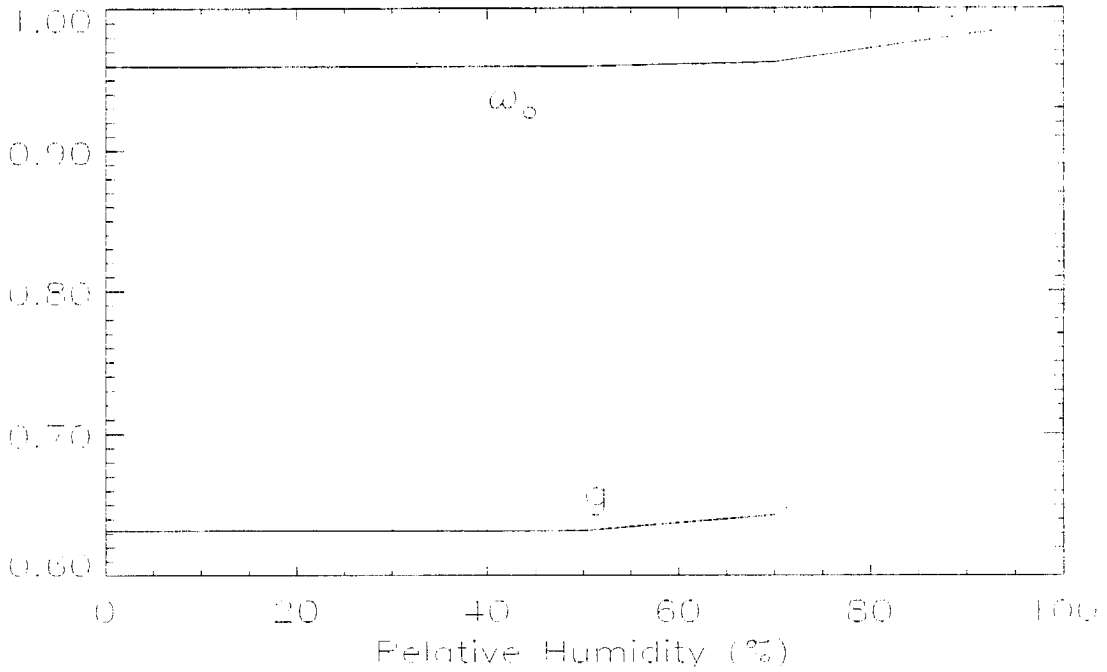

Figure 3.9 - Asymmetry parameter (g) and ω_o as functions of relative humidity (data from d'Almeida et al., 1991).

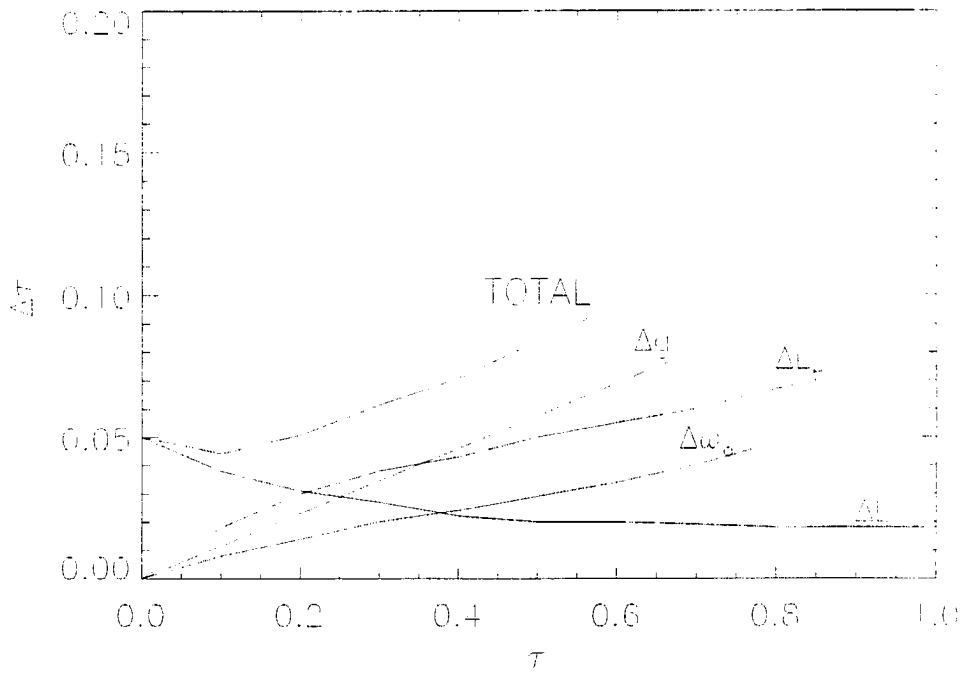

Figure 3.10 - Error budget for τ retrievals assuming errors of $\Delta g = \pm 3\%$, $\Delta L_e = 5\%$ error in sensor resolution, $\Delta \omega_o = \pm 1\%$, and $\Delta L = 0.001$ $Wm^{-2}\mu m^{-1}ster^{-1}$ (1 GOES-8 count) digitization error.

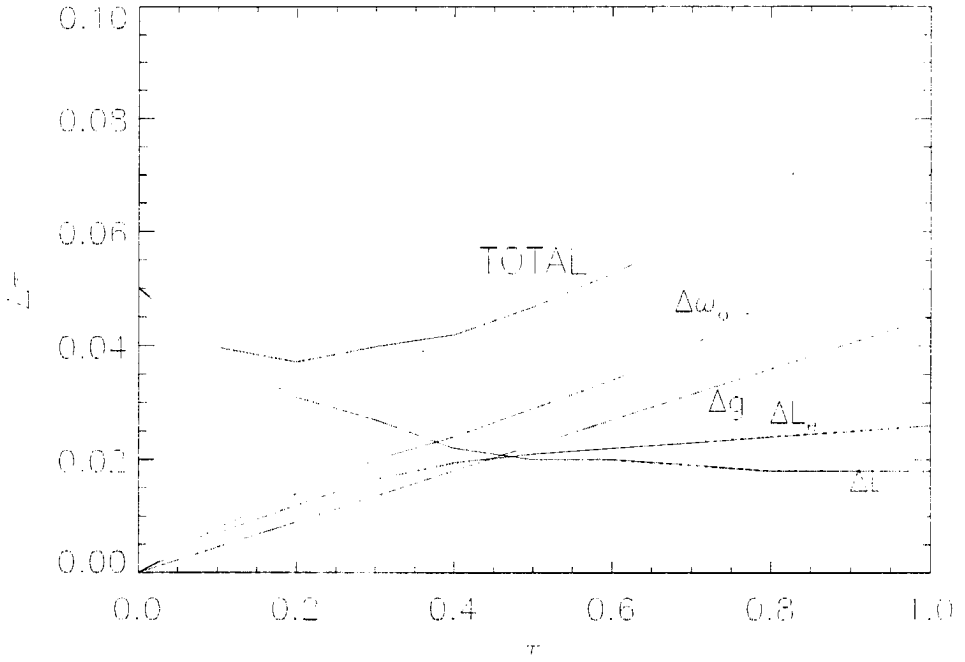

Figure 3.11 - Error budget for τ retrievals assuming errors of $\Delta g = \pm 1\%$, $\Delta L_e = 1\%$ error in sensor resolution, $\Delta \omega_o = \pm 1\%$, and $\Delta L = 0.001$ $Wm^{-2}\mu m^{-1}ster^{-1}$ (1 GOES-8 count) digitization error.

Method

Because of the availability of data between τ retrievals and the IMPROVE dataset, it became apparent that many comparisons could be made. Previous works make relatively fewer comparisons to surface data sets than this work. Fraser (1993) retrieves optical depth for one image over Tadzhikistan and compares his results to observed surface visibilities. Numerous times, Kaufman uses data from polar orbiting satellites (Landsat and NOAA/AVHRR) for only two days - a background and hazy image (Kaufman & Joseph, 1982; Kaufman, 1987; Kaufman et al., 1990).

This work, however, provided optical depth retrievals for many more days and with 4 different types of surface data for comparison.

4.1 Case Study

4.1.1 Selection

Retrievals were made for areas near IMPROVE and NWS sites during episodes of low visibility. Possible cases were initially determined from Daily Weather maps by inspection of the 12z surface maps during the summer of 1995 for stagnant high pressures over the east coast. Table 4.1 summarizes the time periods of the ten periods found using

daily weather maps. After inspecting the IMPROVE data (figures 4.1 and 4.2) and availability of GOES-8 imagery, the choices were narrowed down to 5 periods of a week or longer, possible case numbers B, C, D, G and I. No retrievals were made and no work was done on the other cases, therefore the cases were numbered and are summarized in table 4.2.

GOES-8 data was available at 15 minute intervals over the continental United States. The GOES-8 sector collection over the east coast was changed in July to increase the area westward and to include more daylight hours. The western bound was moved to include the IMPROVE nephelometer site at Mammoth Cave National Park, in Kentucky.

4.1.2 Synoptic Conditions

The dominant forcing in stagnant high pressure over the Eastern U.S. is the Bermuda High pressure area over the North Atlantic Ocean. Climatologically, it is situated in the North Atlantic with a strong ridge extending westward toward the U.S. Cases with coincident high amounts of scattering in the IMPROVE network and stagnant high pressure areas were selected as final cases (Table 4.2). Figures 4.3 through 4.7 depict the position of high pressures for cases 1 through 5, respectively. An H denotes the position of a surface high pressure center with a closed isobar at 7 a.m. EST, whereas an R denotes a broad surface ridge with no closed isobar and numbered subscripts are the Julian day. Positions were determined from NOAA's Daily Weather Maps.

Cases 1, 2, and 3 have similar synoptic trends (figures 4.3 through 4.5). In general, a broad high pressure with a north-south orientation over the Central U.S. moves toward the East Coast. Just off the coast, it strengthens in the ridge of the Bermuda High

and slowly pushes westward as an extension of the ridge. Whereas, case 4 (figure 4.6) is characterized by a nearly stationary surface high pressure area over the Ohio Valley. Case 5 (figure 4.7) is different in that it has two surface highs, the first moving off the coast while a second follows behind a surface low.

4.2 Background Compositing

As mentioned in section 3.1.1, an apparent surface reflectance, ρ_{sfc}, is necessary in retrieving optical depth. This section describes the method used in determining ρ_{sfc}. Background images of ρ_{sfc} were compiled for each time period and for each case. This removed the bispectral reflectance effects of the surface. Images were manually aligned to reduce the change in position of the sector from day to day oscillations. Surface features, such as lakes, river valleys and coastlines, were used to align sectors visually. Then, count values were converted to reflectance using equations 2.1 and 2.2. A threshold value of 0.157 (175 GOES visible counts) reflectance was subjectively chosen to mask a pixel as a cloud. This value was used only in the Eastern U.S. and would have to be modified were this method to be used over higher reflecting surfaces, such as the desert areas of the Southwestern U.S. Also, pixels near a cloud were not used in the background composite, to remove possible cloud shadows from the composite. The distance from a cloud to mask shadows was determined from θ_o. After cloud and shadow masking was performed, the composite was created by choosing the darkest of the remaining reflectance values for each pixel for the duration of the case (from 7 to 10 days).

Figure 4.8 shows an example of the background compositing process. Note: This sector was not used in this study, but chosen for its distinct geographical feature. The dark horizontal feature in figure 4.8c is Grand Lake St. Mary's in Western Central Ohio, 50 miles north of Dayton. Daily oscillations of the satellite can be seen in the repetition of this lake in the un-navigated and non-cloud masked background (fig. 4.8a). Once navigated, fig. 4.8b, the oscillations are gone, but cloud shadows are still prevalent. Figure 4.8c shows the final product, after manual navigation and cloud shadow masking. Note that the shadows are removed and the valleys in the upper right hand corner are more clearly defined than in figure 4.8a.

The compositing process requires that a pixel have a day when the atmosphere had a minimal amount of particles in it during the case time period. When this occurs, the A/D model calculates τ such that $\rho_{A/D}$ matches ρ_{sat}. In the event that an air pollution event encompassed the case such that the darkest pixel still had a significant amount of aerosol, the $\tau_{A/D}$ is the difference between the τ for that particular satellite image and the smallest τ for that pixel. This results in incorrectly retrieved lower τ values.

4.3 Application of the Adding/Doubling Model

Many parameters are necessary for the adding/doubling model to calculate optical depth. As mentioned above, the necessary parameters are: sun-earth-satellite geometry, ω_o, g, ρ_{sfc}, ρ_{sat} and two model parameters (number of azimuth modes and satellite zenith category).

Equations for sun-earth-satellite geometry were calculated using:

$$\cos\theta_o = \sin\varphi \sin\delta + \cos\varphi \cos\delta \cos h \tag{4.1}$$

$$\sin\theta = \frac{r_G \sin\beta}{\sqrt{r_e^2 + r_G^2 - 2r_e r_G \cos\beta}} \tag{4.2}$$

$$\sin\phi_o = \frac{\sin h}{\sin\beta} \tag{4.3}$$

$$\sin\phi = \frac{\sin(\lambda - \lambda_G)}{\sin\beta} \tag{4.4}$$

where:

$$\cos\beta = \cos\varphi \cos(\lambda - \lambda_G), \tag{4.5}$$

h is the hour angle, δ is the solar declination angle, φ is latitude, λ is longitude, r is radius from center of the earth and subscript e and G denote the earth and GOES-8, respectively. Equation 4.1 and tables for δ came from Houghton (1985) and equations 4.3 through 4.5 were derived using spherical and planar geometry. The satellite zenith category, a result of the Gaussian quadrature approximation, was chosen using the category value nearest the actual θ. The surface instrument site latitude and longitude were used to calculate the angles. This incorporates minimal error in the τ retrieval because retrievals were made for a 9 by 9 pixel area (5.1 × 9 km) centered on the surface site.

The background surface reflectance was determined according to section 4.2 and the satellite detected reflectance was calculated using equations 2.1, 2.2, and 4.1. Also, pixels in the background composite image were coupled to pixels in the satellite image using the same manual alignment data used to remove the oscillations from the background composite.

Various techniques were used to decrease the time the model took to converge on a solution. A look up table was used for previously calculated values of ρ_{sfc} and ρ_{sat} having the same optical parameters and geometry. The threshold value for convergence of the iterative solution was determined from the responsivity of the Imager sensor. The calculated τ was considered a solution if it produced (in the A/D model) a haze reflectance (equation 2.4) within ±0.5mk ($\pm 5.316 \times 10^{-4}$). Another model variable is the number of azimuth modes (NAM) used in retrieving τ. Increasing the azimuth modes increases the τ accuracy, but also increases the retrieval time. Table 4.4 shows the relationship of τ to NAM. It is obvious that NAM = 1 is insufficient to resolve τ, yet NAM = 10 requires too much computing time. So NAM = 3 was chosen because it had less than 1% change in τ from $\tau_{NAM=10}$.

Because the source and composition of the aerosols is unknown, the optical properties ω_o and g must be assumed. The same values were used in all of the subsequent case studies and comparisons, because no further information is known about the aerosol. Values found or used in previous work are shown in Table 4.3. Values for ω_o range from 0.956 to 0.97 and g = 0.748 for hazes. Previous studies report aerosol size distributions and calculate optical parameters from Mie code, the parameter g is rarely directly reported. The values in this study were $\omega_o = 0.956$ and g = 0.75, because these seem to be the general consensus. The error in the retrieved τ in assuming these values was discussed in section 3.3.4. Relative humidity measurements from the IMPROVE sites were used as a second retrieval set by adjusting the optical parameters according to figure 3.9 and relative humidity measurements from IMPROVE sites.

4.4 Post-retrieval processing

Figures 4.9 and 4.10 show examples of optical depth retrievals over ocean and land, respectively. Figure 4.10 is the same satellite data used in the control runs of the error budget (section 3.2), while the ocean scene is off the coast of North Carolina.

Figure 4.9a shows the visible satellite image over the ocean on 13 July 1995 at 14:15z. The image size is 62 × 108 km (108 × 108 pixels). Figure 4.9b shows the optical depth retrieval of the image in part a. The black areas are where the A/D model retrieved cloud pixels. The cloud edges are not identified as cloud, but are retrieved as aerosol. This is seen in figure 4.9c. The cross section in c is the white line in part b, which passes through a small cloud. This small cloud was not masked by the retrieval as cloud, but retrieved as an optical depth.

The problem with cloud filtering for aerosol retrievals is to filter cloud, but not filter aerosols that may have reflectances with similar values of some cloud edges or thin clouds. The signal for aerosol retrievals lies in the range of reflectances between the surface and a cloud. It is important not to remove aerosols. Therefore a conservative filter was used, such that only the brightest pixels were masked. The retrieval determines a pixel as a cloud if the detected radiation is 100 GOES-8 counts (55.1 $Wm^{-2}ster^{-1}$) brighter than the background. Also, any retrieval with a cloud detected in the 9 ×9 retrieved area is not used for comparison, because the τ from that retrieval is most likely affected by the cloud edge, and not boundary layer aerosols. Therefore scenes used in the comparisons of chapter 5 were manually checked for clear skies near the surface site.

Also, in figure 4.9c, the ocean seems noisy, which is most likely due to noise in the instrument. The standard deviation for the $\tau_{A/D}$ in an area away from clouds is 0.08, which is attributed as noise. Therefore, the retrievals are averaged over a 9 × 9 area, the size of the matrix retrieved over surface sites. The spatial averaging area size (9 × 9) was chosen as a size that aerosol optical depth should be homogeneous. Also, the size allowed for sensing and filtering of nearby clouds. The solid line in 4.9c shows this averaging. It reinforces the need for manual cloud clearing, because no pixels were flagged as clouds, yet average τ in the cloud is 0.6. This value would be mistaken as an aerosol in any comparisons, unless manually filtered out.

Figure 4.10 shows similar imagery for the Shenandoah area. Figure 4.10a is the satellite image while b is the τ retrieval. Figure 4.10c is a spatial average of the τ retrieval. White boxes in center and upper-left are clouds. The lower left portion of figure 4.10c shows an aerosol layer with τ retrieved near 0.4. The cross section (white line in lower part of image) is shown in figure 4.10d. The retrieval is somewhat noisier than the ocean retrieval above with a standard deviation of 0.12, yet shows a west to east increase in τ, from 0.2 to nearly 0.4.

Also, comparisons to IMPROVE and NWS data were temporally averaged because they were only available at hourly intervals. Therefore, τ retrievals were averaged to the nearest hour. The exception is the pyrheliometer data which has 1 minute resolution, in which case no temporal averaging was performed.

Table 4.1 - List of Possible cases as determined by Daily Weather Maps

POSSIBLE CASE	JULIAN DAYS	POSSIBLE CASE	JULIAN DAYS
A	126-128	F	211-213
B	**140-146**	**G**	**222-230**
C	**164-171**	**H**	**234-236**
D	**191-197**	I	241-250
E	205-208	J	261-263

Table 4.2 - Time periods of the cases used in this study

CASE	JULIAN DAYS	DATES	TIMES OF GOES-8 DATA
1	140-148	May 20-28	12:15-15:31z
2	163-167,171-172	June 12-16,20-21	12:15-15:31z
3	191-200	July 10-19	12:15-20:45z
4	220-230	Aug. 8-18	12:15-20:45z
5	240-249	Aug. 28 - Sep. 6	12:15-20:45z

Table 4.3 - List of references and optical properties used

REFERENCE	AEROSOL TYPE	ω_o	g
Kaufman et al., 1990	Smoke Haze	0.92 0.97	
Fraser, 1993	Dust	0.93	
Kaufman, 1987	Industrial Haze	0.94 ± 0.04	
Kaufman & Joseph, 1982		0.96	
Schneider & Fuller, 1994	Shenandoah Haze	0.956	0.748

Table 4.4 - Determination of the number of azimuth modes (NAM) for use in the A/D model.

NAM	$\bar{\tau}$	$\lvert\bar{\tau}-\bar{\tau}_{10}\rvert$	$\frac{\lvert\bar{\tau}-\bar{\tau}_{10}\rvert}{\bar{\tau}_{10}}$ (%)
1	0.3390	0.0584	20.83
2	0.2738	0.0068	2.42
3	0.2790	0.0016	0.57
4	0.2806	0.0002	0.07
10	0.2804	-	-

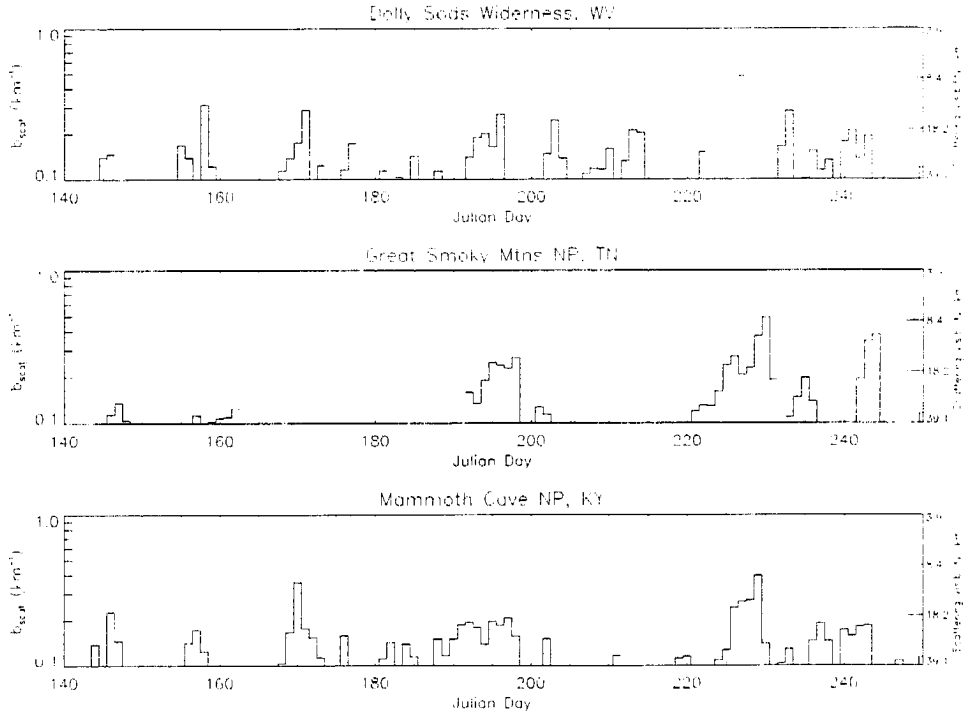

Figure 4.1 - Time series plot of b_{scat} during the summer of 1995 for 3 IMPROVE sites in the east. The secondary y axis is calculated using equation 2.13 and an assumed $\Delta z = 1$ km.

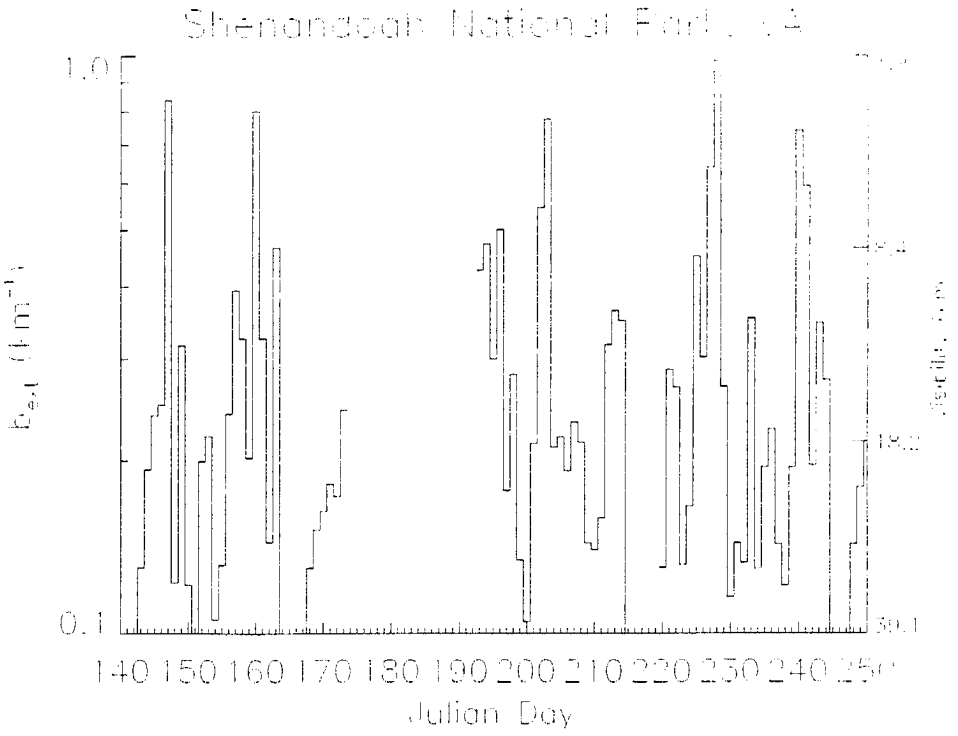

Figure 4.2 - Time series plot of daily average extinction coefficient (b_{ext}) for the transmissometer at Shenandoah National Park The secondary y-axis is calculated using equation 2.13 and an assumed $\Delta z = 1$ km. Note: the instrument was not operating between Julian day 173 and 193.

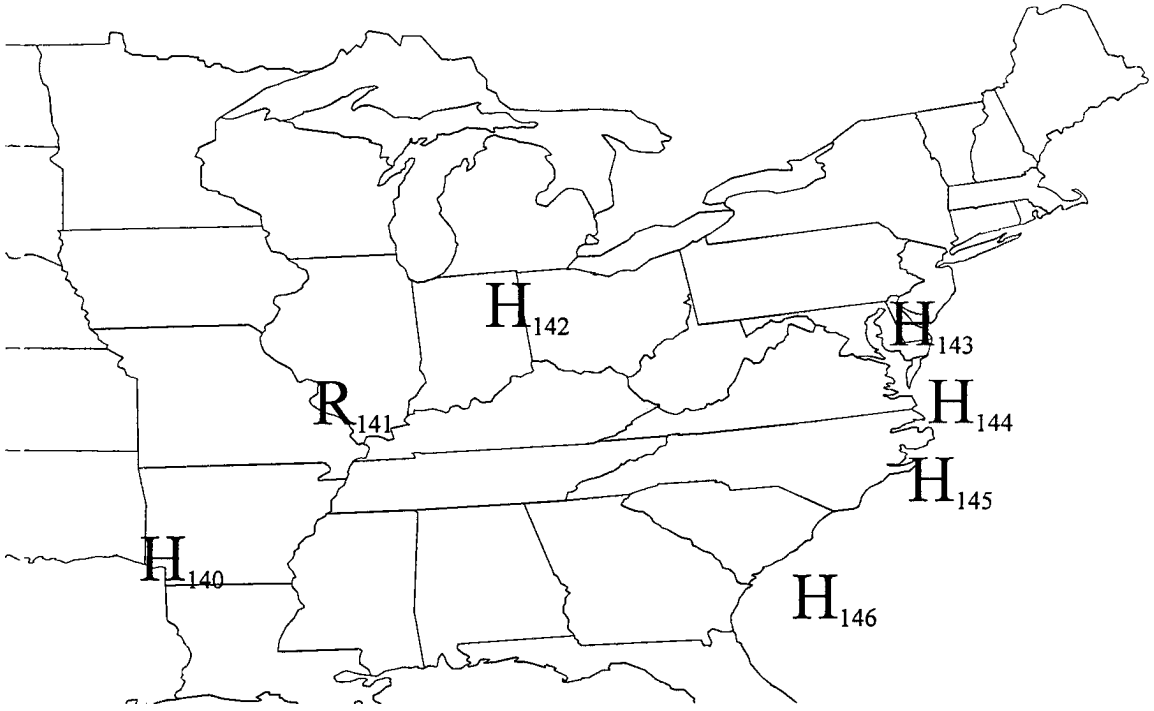

Figure 4.3 - Positions of surface high pressure areas (H) and ridges (R) during Case 1. Numbers denote Julian day.

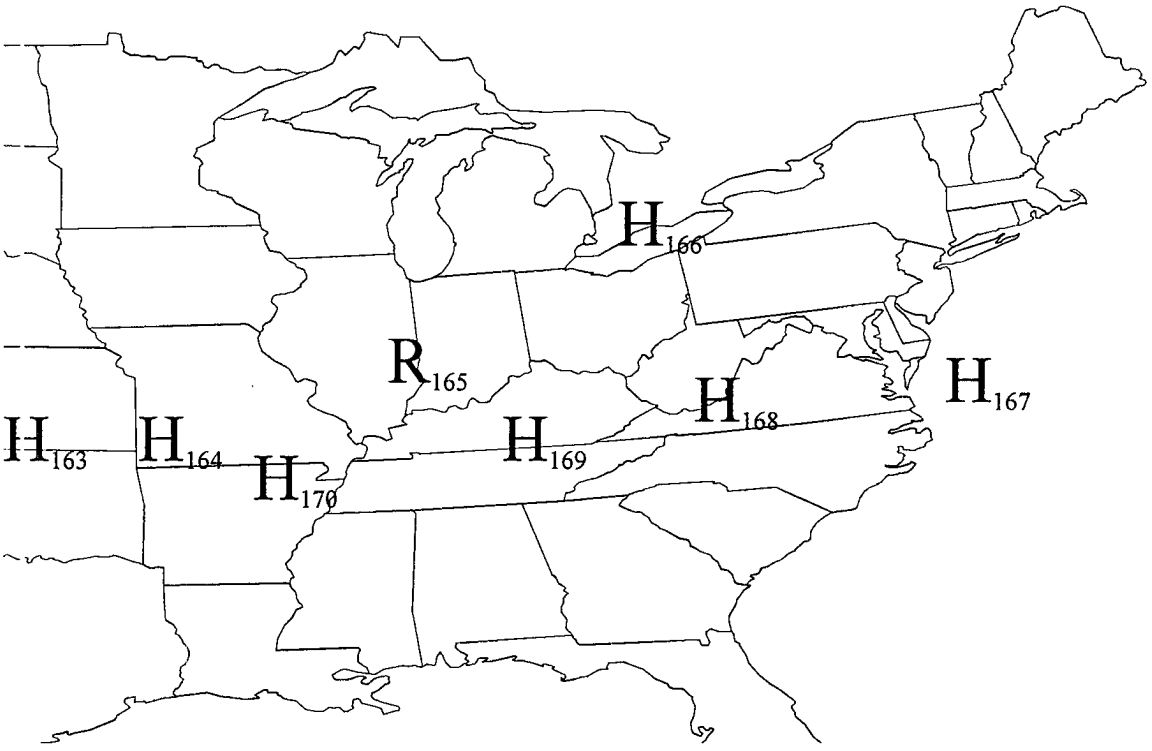

Figure 4.4 - Same as figure 4.3 except for Case 2.

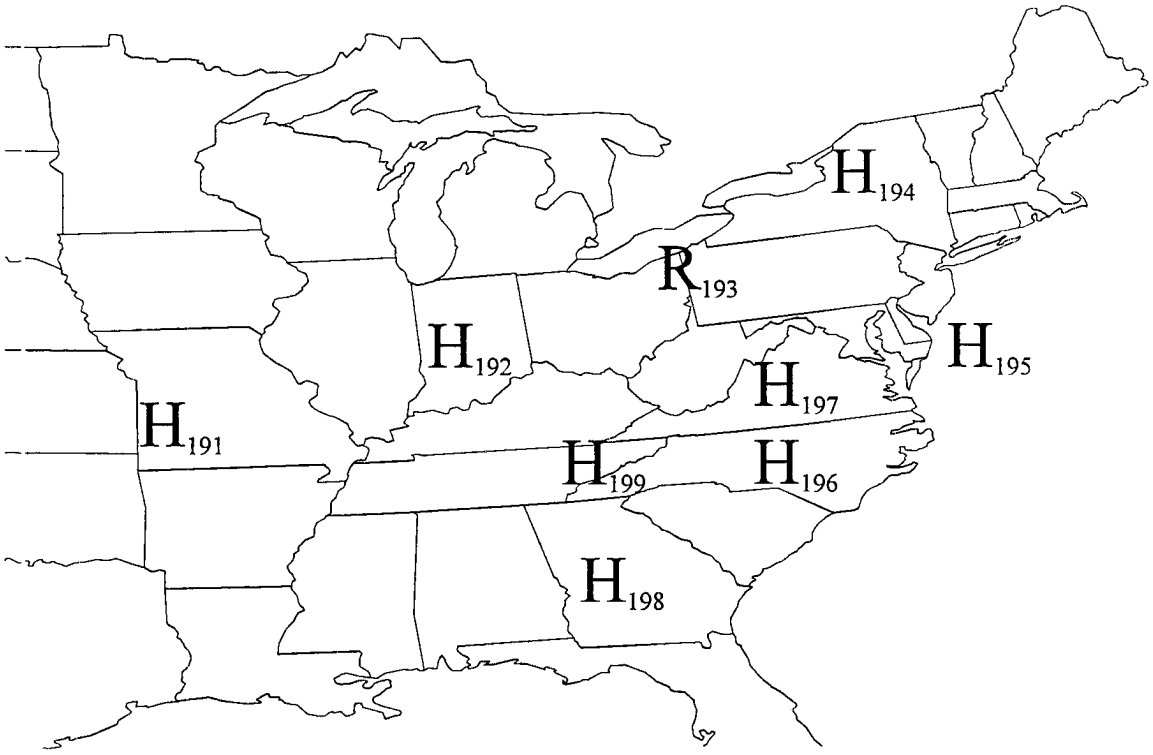

Figure 4.5 - Same as figure 4.3 except for Case 3.

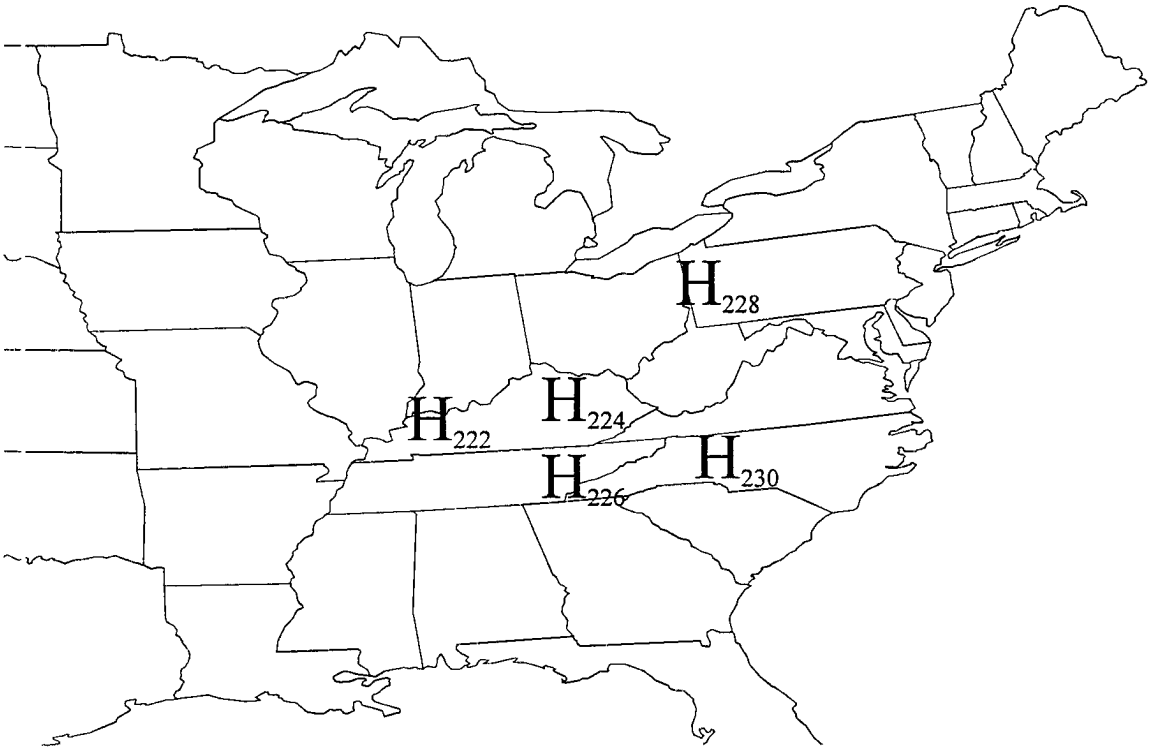

Figure 4.6 - Same as figure 4.3 except for Case 4.

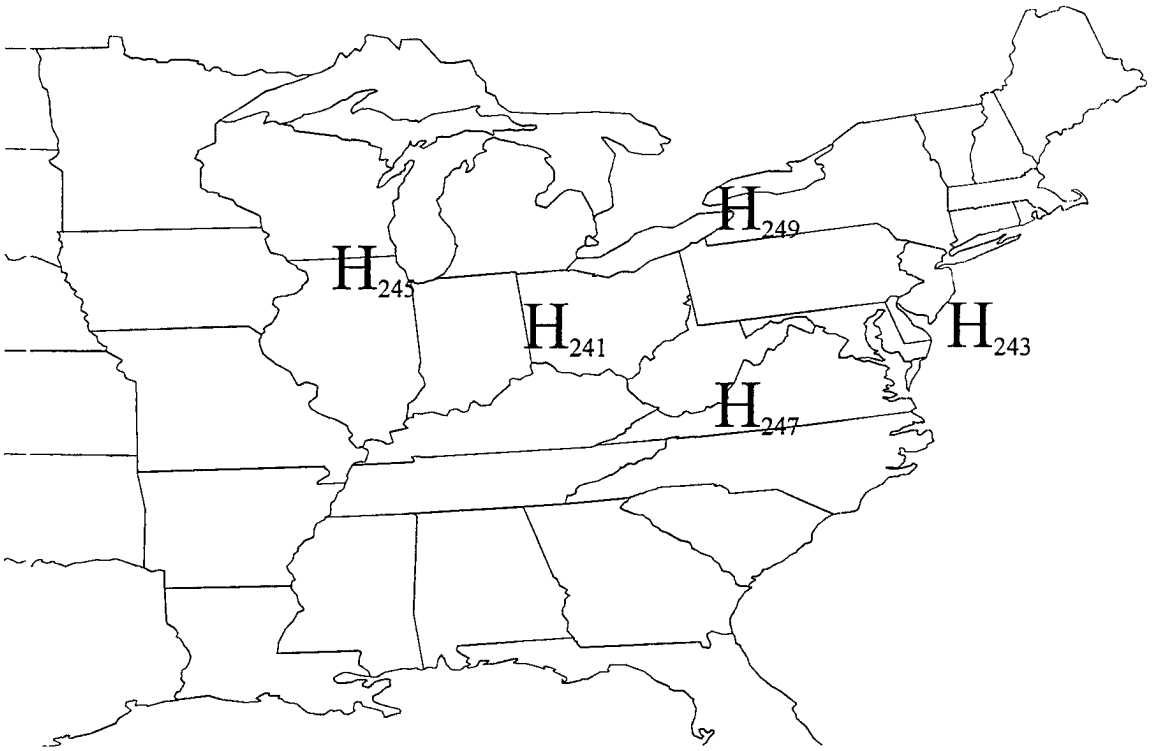

Figure 4.7 - Same as figure 4.3 except for Case 5.

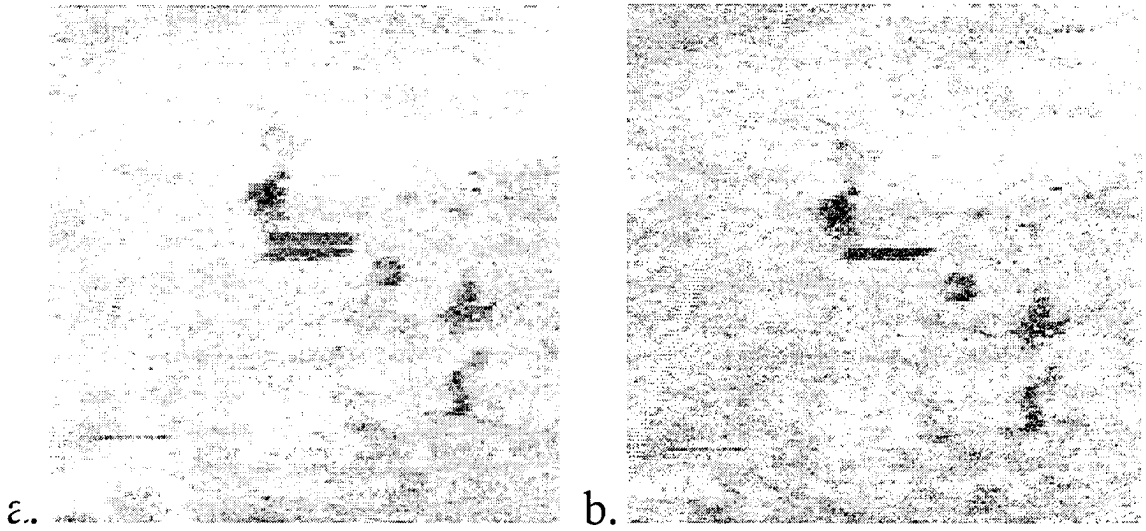

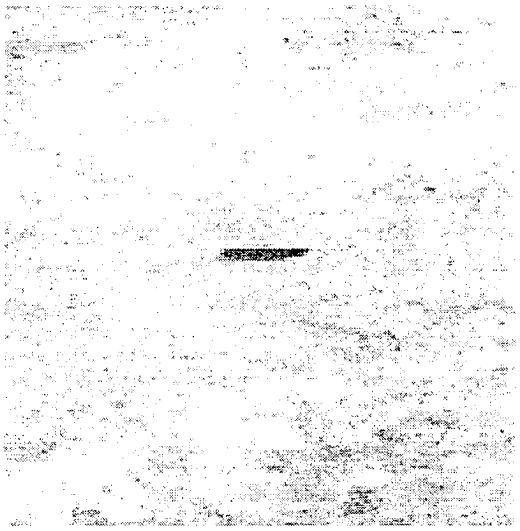

C.

Figure 4.8- Example of manual navigation and cloud shadow filtering. a) raw composite image, b) navigated composite image without cloud shadow filtering, and c) the final product is a manually navigated image filtered for cloud shadows. The plus signs are the Ohio/Indiana state boundary.

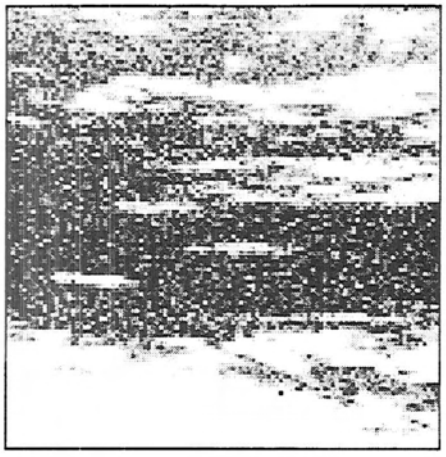

A)

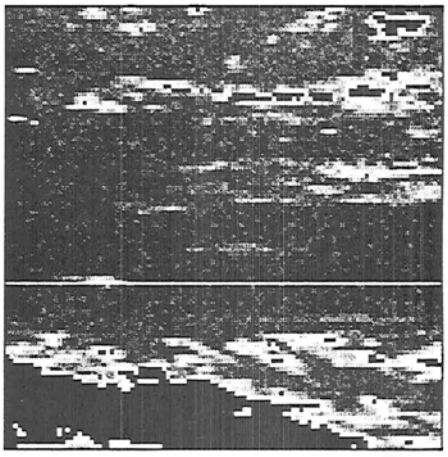

B)

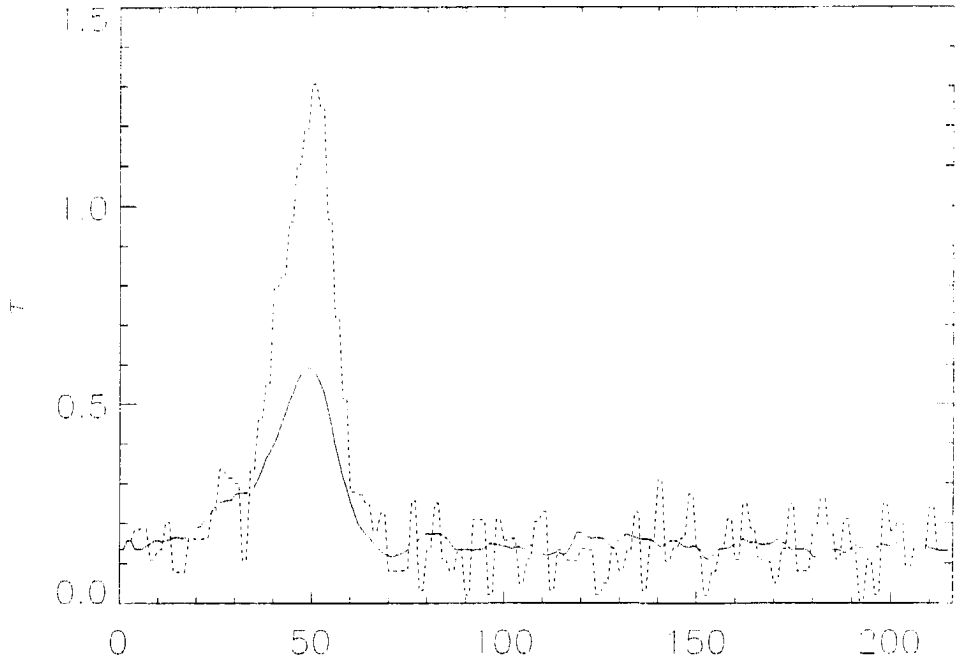

C)

Figure 4.9 - Ocean retrieval of optical depth. a) Visible satellite image, b) optical depth retrieval, blackest portions are cloud, c) cross section of optical depth (dashed) and spatially averaged (solid) along the white line in part b.

A)

B)

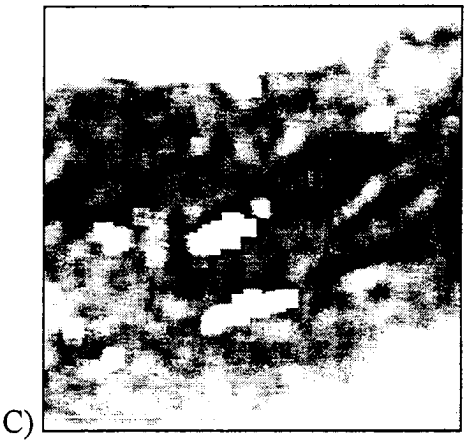

C)

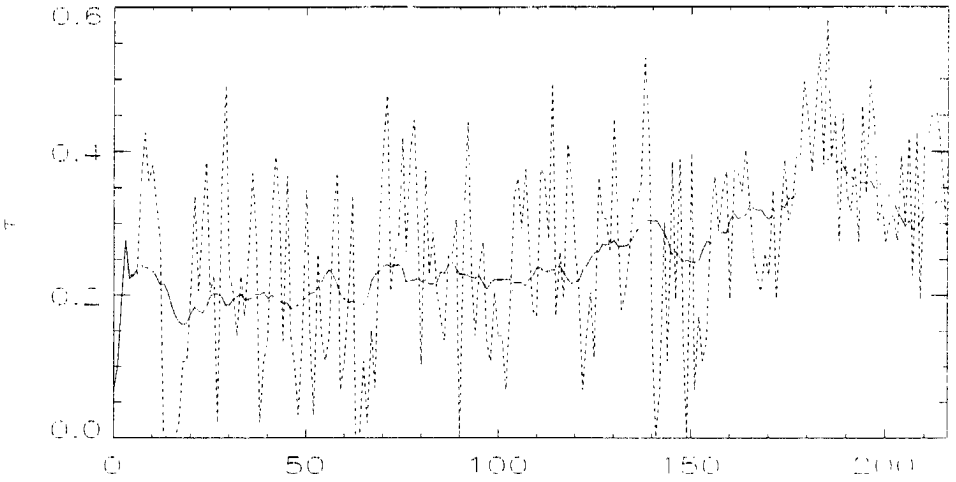

D)

Figure 4.10 - Optical depth retrieval over the Shenandoah area. a) Visible satellite image, b) Optical depth retrieval of part A, c) 9 × 9 spatial average of part B, d) cross section through the southern portion (white line) of B (dashed) and C (solid).

Results

In section 3.12 and 3.2, the ability of the Adding/Doubling model to retrieve optical depths from GOES-8 visible data was discussed. It was determined that retrieving τ is feasible as long as the conditions were not near the critical albedo range (determined by the surface reflectance, solar zenith angles and aerosol optical properties). The areas in which retrievals were aimed were forested mountains of the east (specifically IMPROVE sites) which happen to have visible reflectances (measured by GOES-8) less than 0.1. This range does not fall in the critical reflectance range for aerosols expected to be found over this area.

This chapter presents the comparisons of optical depth retrieved from satellite data using an A/D model, presented in chapters 3 and 4, to various surface data discussed in chapter 2. Results of some retrievals were used to estimate their direct effect. Further discussion of these results will be given in chapter 6.

5.1 Comparison to Surface Measurements

Before discussing comparisons of the satellite τ retrievals to surface data, a review of the process to retrieve τ is given. As discussed in chapter 2, the satellite retrieval of τ is a vertically integrated quantity. Because a "background" reflectance is chosen for

comparison, the retrieved τ is the required optical depth to increase the reflected radiance from that measured on a clear day to that measured on a hazy day. This is done by increasing the reflected radiation by "adding" an aerosol layer with the specified optical parameters. Therefore, the retrieved optical depths are representative of a column of atmosphere. Conversely, a surface point measurement of some aerosol property (extinction, scattering, etc.) is just that, only a data point from the surface. Although, most of the changes in aerosol amounts (on the time scale of the cases presented) are limited to the boundary layer. This is because the major source for all aerosols is the earth. Also note that stratospheric aerosols do not affect this retrieval method, unless there is a significant change in optical depth, e.g. volcanic eruption between the background composite and satellite image. Therefore, most of the optical depths retrieved caused by changes in aerosols in or just above the boundary layer. How well a surface measurement of aerosol represents a column average is a different story. Moreover, the best correlation that this study might find is the correlation of surface b_{ext} to its vertical average (τ). What is being compared is the measurement of b_{ext} (or b_{scat}) and the retrieval of τ. Certainly, pyrheliometers sample an atmospheric column for a better comparison, but pyrheliometer measurements were sparse during the summer of 1995.

5.1.1 ARM-BSRN Site

The comparison to the pyrheliometer at the ARM site in the Southern Great Plains (near Lamont, OK) was made using a separate case from the cases mentioned in section 4.1, because it was contained in a different archived satellite sector and lies much further west than the IMPROVE sites mentioned. Also, because of the archived times of the

sector, images are only available between 19:15 and 1:45z (14:15 to 20:15 CDT) at half hour intervals. This limits comparisons to the afternoon hours.

Figure 5.1 shows the scatter plot of τ retrieved from satellite data using the A/D model and τ measured by the pyrheliometer. As mentioned above, the retrieval process only excludes the brighter clouds. Therefore, the satellite images were investigated for the presence of clouds or possible presence of subpixel cumulus clouds. Also, the pyrheliometer data was investigated for clouds. Data from the pyrheliometer were excluded if the τ measurement shortly before and after showed significantly smaller τ values. These instances were interpreted as a sub-pixel cloud, directly between the sun and instrument for a short amount of time. The result of this cloud filtering is shown in figure 5.2. The numbers represent the Julian day of the data. While the points with larger values of τ have been excluded, the scatter has only decreased slightly (table 5.1). Unfortunately, the optical depth for the pyrheliometer ranged from 0.03 to 0.14, which were, for the most part, less than the random noise of the retrieval and not large enough range for a conclusive comparison.

5.1.2 IMPROVE Network

The amount of stations and data in the IMPROVE network allowed for better comparisons than the pyrheliometer. Hereafter, the IMPROVE sites will be abbreviated as: DOSO - Dolly Sods N. F., GRSM - Great Smoky, N.P., MACA - Mammoth Caves, N.P. and SHEN - Shenandoah N.P. Also, a comparison will refer to the relation of satellite, A/D model retrieved τ ($\tau_{A/D}$) to IMPROVE data (b_{scat} or b_{ext}) at a specific site for a certain case. $\tau_{A/D}$ is spatially averaged and manually cloud filtered, as described in

section 4.4. The number of samples (n or the parenthetical value in tables 5.2 and 5.3) is defined as the total points available for each comparison.

Table 5.2 shows the change in r for the GRSM nephelometer between single pixel comparison and spatial averaging. The averaging results in better correlation in cases 1 and 3 and little change in cases 4 and 5. The decreases in n in table 5.2 are due to removal of retrievals that flagged clouds within the 9 × 9 averaging box. The spatial averaging removed some of the noise in the retrieval, as seen by the increase in correlation in some cases. Table 5.3 shows the change in sample size and r due to manual cloud filtering for all cases. As mentioned above, satellite images that showed clouds near the IMPROVE sites were removed from the comparisons, which largely reduced n. Case 2 will not be used in the remainder of the study because the GRSM nephelometer was inoperable and MACA wasn't yet in the satellite archived sector (see section 2.1), while DOSO and SHEN were obscured by clouds for the majority of the case. The shaded boxes in table 5.3 represent comparisons that will no longer be used. The cloud removal process had a variable affect on r in the remaining comparisons, increasing r in 8, decreasing in 3 and having little affect on 1 comparison. Also from table 5.3, it can be seen that there exist some well correlated comparisons, and others not showing any positive correlation.

An example of a well correlated case is GRSM case 3 (figure 5.3) for which r = 0.763. It was one of the better comparisons. Overall, the GRSM site had better correlation, except for case 5. Figure 5.4 shows a scatter plot for case 5. It can be seen in 5.4b that some relatively bad retrievals occurred at 12z. In earlier cases, this was not a

problem. But for case 5, the sun is lower in the sky (smaller declination angle) and θ_o = 77° for 12:15z. This shows a possibility that retrieval errors might be large when θ_o is large. Upon further inspection of the satellite imagery, it appears possible that days 244 and 246 could be affected by cloud edges or subpixel clouds. This would explain the high values of $\tau_{A/D}$ for that day. Removing these problem areas from the comparison (figure 5.4d) results in better correlation (r = 0.777).

Figure 5.5 shows the scatter plots for other comparisons with correlations affected by small datasets, cloud contamination, and other errors. SHEN case 1 has excellent correlation (r = 0.993) only because most points are clustered over a small range of b_{scat} resulting from an incomplete dataset to make a complete comparison. However, DOSO case 3 does show an example of a poor retrieval. The large range of $\tau_{A/D}$ values for small b_{scat} could be cloud contaminated retrievals, at least for the points above $\tau_{A/D}$ = 0.5. Although, the $\tau_{A/D}$ values for larger b_{scat} values are lower than those retrieved in other scatter plots. This could be caused by an errant background composite. ρ_{sfc}, from the background composite, might be contaminated by heavy aerosol (as mentioned in section 4.2), which could lead to smaller $\tau_{A/D}$ values.

Tables 5.4 through 5.7 summarize the statistics for the IMPROVE comparisons under varying conditions. The first two rows provide a range of visibilities during the case, estimated from the IMPROVE instrument. As mentioned in section 2.2.2, there are nephelometers at DOSO, GRSM and MACA and a transmissometer at SHEN, which measure b_{scat} and b_{ext}, respectively. Then there are four sets of conditions for each comparison. The first is for τ retrieved using constant optical parameters, whereas the

second set varies g and ω_o according to the relative humidity measured at the IMPROVE site and figure 3.9. The second two sets of comparisons adjust the $\tau_{A/D}$ retrieved by the Δz from the NWS rawinsondes to calculate a pseudo-retrieved extinction coefficient (pseudo because part was calculated using *in situ* data):

$$\hat{b}_{ext} = \frac{\tau_{A/D}}{\Delta z} \tag{5.1}$$

As mentioned in section 2.2.3, this should increase the correlation by taking into account a variable size boundary layer. The rows m and b refer to the slope and offset, respectively, for the least squares best fit line. E is the standard error of the estimate and $\bar{\tau}$ (or $\overline{\hat{b}_{ext}}$) is the average τ (or $\hat{b}_{ext}$) for the comparison.

Figure 5.6 shows the relationship of $\tau_{A/D}$ to visibility. The data is from GRSM case 3 and the dashed line is the least squares fit. The visibilities in this plot are approximations of the actual visibility using equation 2.13 and a constant scattering depth (Δz). This shows that at higher visibilities, there is more noise in the retrieval.

5.1.3 NWS Visibility Reports

Two characteristics limit the comparison of retrieved τ to visibility reports. First, visibility is reported in incremental amounts, because visibility is the distance to the furthest visibly detectable object which is not a continuous measurement. Secondly, visibility is reported at airports because of aviation concerns. Therefore, there is often an upper limit above which, visibility is simply rounded down. For example, an actual visibility might be 35 mi., although the furthest object visible with a known distance may be 25 mi. away. Furthermore, it may be the standard procedure at such an airport to

report visual ranges between 0 and 20 miles, then the visibility is reported as 20 miles, a far cry from the actual 35 mi.

Figure 5.7 shows the locations of NWS sites for which τ was retrieved for case 3. Retrievals for the NWS satellite sector were not manually cloud filtered, because there are many sites in the sector, covering a large horizontal area. An ideal comparison of visibility and $\tau_{A/D}$ is shown in figure 5.6 for an IMPROVE site, which measures aerosol scattering (or extinction) in a more continuous sense than the NWS. Figure 5.8 shows the comparison of $\tau_{A/D}$ (the ordinates) to observed visibility (abscissas in km) for the NWS sites shown in figure 5.7. Most noticeable is that, for most sites, there seems to be no correlation (remembering that τ is reciprocally related to Visibility). One reason being that the $\tau_{A/D}$ values are spread over the finite intervals of the NWS observations. Another being that the observations have an upper limit (more noticeable for sites such as FKL and HSP). Diamonds in figure 5.8 are visibility reportedly obstructed by haze. Haze is reported for visibilities between 1 and 25 km at ZZV. One would expect to see more of these reports at lower visibilities or for higher values of τ, but does not. Also, the correlations were no better for ASOS sites. Assuming that possible cloud contaminated points exist, some sites that showed positive correlation (a decrease in τ with increasing visibility) are: MFD BVI, YNG, CMH, and PIT. Overall, this shows that $\tau_{A/D}$ is generally incomparable to surface visibility because of the errors in both measurements.

5.2 Forcing Calculations

The direct effect was calculated by the 2-stream model by computing difference between the amounts in outgoing shortwave radiation between clear sky and an aerosol-laden atmosphere. The aerosol layer was defined as 1 km deep at the surface with the same optical properties used in the A/D retrieval (ω_o = 0.956 and g = 0.75).

Computations for forcing using optical depth maps were highly correlated with τ. The amount of solar radiation lost to space ($-\Delta F$) is plotted against optical depth for several θ_o values in figure 5.9. Correlation coefficients for the relationship are -0.996, -0.999 and -0.999 for the θ_o equal to 0°, 30° and 60°, respectively. This is true for all aerosols and areas, as long as the sun-earth-satellite geometry and aerosol optical properties remain constant. Then ΔF can be written as (using a least squares fit):

$$\Delta F = -45.4\tau - 0.34 \ [Wm^{-2}] \tag{5.2}$$

for θ_o = 60°. Then, this can be written:

$$\frac{d(\Delta F)}{d\tau} = -45.4 = -k_\tau \tag{5.3}$$

where k_τ is the slope of the least squares fit. Also, note that this equation is similar to equation 3.10 which Charlson et al. (1991) derived from a box model. Figure 5.10 shows the relationship of k_τ to θ_o. It can be seen that there is a maximum of forcing near 65°, which can change, depending upon the optical parameters of the aerosol.

From this model and using the retrievals in the study it is possible to retrieve the optical depth and estimate the total energy lost to space during the day. An example of this is calculated for the GRSM IMPROVE site for Julian day 241 (29 August 1995).

Figure 5.11 shows the time series of the ρ_{sfc} and ρ_{sat} for Julian day 241 over GRSM, where ρ_{sfc} comes from the background compositing for all the days of the case while ρ_{sat} is from the satellite images for that day. Most noticeable, is that the surface reflectance does vary with solar geometry by 10%, showing the surface is not Lambertian. Figure 5.12 shows the time series of the τ and energy lost to space. Integrating ΔF over the 7 hours (14:00 to 21:00z) resulted in 1.2×10^5 J m^{-2} lost to space. This day had a low average τ, but was clear all day.

However, figure 5.13 shows the time series of τ and magnitude of aerosol forcing for a hazy day ($\bar{\tau} = 0.46$) over MACA on the morning of Julian day 228 (the afternoon of the day was cloud covered). The forcing was larger, by about four times, than the forcing estimated for Julian day 241 over GRSM. Integrating the aerosol forcing resulted in 2.1 $\times 10^5$ J m^{-2} lost to space over 3.5 hours in the morning. This was twice the forcing that occurred over GRSM, but in half the time.

To put this into perspective, assume that the lost energy would have been absorbed by the ground. So the energy might have gone to evaporating soil moisture or surface water (lake or ocean). If all the energy goes to evaporation, then using the Latent heat of vaporization (~2.5×10^6 J kg^{-1}) the amount of water not evaporated due to less energy can be estimated. This resulted in 0.048mm of lost evaporation for GRSM and 0.084mm for MACA. The direct effect is shown as a fraction of the available solar radiation in figure 5.14. The forcing amounted to 1.5 to 2.5% of the total solar radiation.

The graphs for $\Delta\rho$ as a function of τ and ΔF as a function of τ are very similar. Therefore, it was hypothesized that one could directly infer the aerosol forcing directly

from satellite measurements. Figure 5.15 shows that this is possible. The ΔF was calculated from the 2-stream model using τ calculated from satellite and the ΔL_{SAT} is the increase in satellite detected radiance (comparable to $\Delta\rho$). There is a high correlation (r = 0.920) and nearly a one-to-one correspondence (slope = 1.3) between the two variables.

Table 5.1 - Statistics for the comparison of retrieved τ to measured τ.

	ALL POINTS	CLOUD FILTERED
n	85	42
r	0.218	0.286
$\overline{\tau_G}$	0.423	0.272
$\overline{\tau_p}$	0.278	0.0732

Table 5.2 - Correlation coefficients (and number of samples) for pixel and spatially averaged comparisons to the Great Smoky N.P. nephelometer.

CASE	$\tau_{site}(n)$	τ_{avg}
1	0.656 (17)	0.870 (16)
3	0.334 (42)	0.763 (30)
4	0.839 (23)	0.790 (21)
5	0.0786 (56)	0.138 (46)

Table 5.3 - Table of correlation coefficients (and number of samples) for all cases and IMPROVE sites (top) and for manually cloud filtered (bottom).

	CASE 1	CASE 2	CASE 3	CASE 4	CASE 5
DOSO	0.541 (26)	-0.104 (15)	0.00940 (57)	-0.352 (24)	0.582 (63)
	0.224 (10)	-	-0.390 (20)	-	0.722 (28)
GRSM	0.770 (29)		0.620 (31)	0.419 (23)	0.509 (56)
	0.870 (16)		0.763 (30)	0.719 (21)	0.138 (46)
MACA			0.102 (49)	0.595 (29)	0.413 (66)
			0.265 (39)	0.562 (29)	0.0941 (58)
SHEN	0.877 (15)	0.594 (13)	0.226 (24)	0.711 (4)	0.620 (35)
	0.993 (9)	0.451 (6)	0.669 (9)	-	0.790 (27)

Table 5.4 - Statistics for IMPROVE comparisons - Case 1

PARAMETER	DOSO	GRSM	MACA	SHEN
V_{max}	248	111		66
V_{min}	48	36		16
DEFAULT				
n	10	16		9
r	**.223**	**.870**		**.993**
m	.53	1.5		2.8
b	.088	.012		-.10
E	.041	.0076		.00034
$\bar{\tau}$	.11	.10		.12
R.H. ADJUST				
n	9	14		11
r	**.294**	**.857**		**.951**
m	.44	.874		2.3
b	.046	.017		-.10
E	.023	.0057		.012
$\bar{\tau}$	.068	.071		.14
R.H. & ΔZ ADJUST				
n	9	14		11
r	**.0630**	**.817**		**.932**
m	.042	.41		.414
b	.028	.0029		-.01
E	.012	.0039		.0061
$\overline{\hat{b}_{ext}}$	.030	.028		.034
ΔZ ADJUST				
n	10	16		10
r	**-.0462**	**.812**		**.945**
m	-.053	.66		.72
b	.052	.0012		-.02
E	.022	.0064		.0078
$\overline{\hat{b}_{ext}}$	.050	.040		.049

Table 5.5 - Statistics for IMPROVE comparisons - Case 3

PARAMETER	DOSO	GRSM	MACA	SHEN
V_{max}	41	65	30	20
V_{min}	6.4	15	4.6	3.0
DEFAULT				
n	20	30	39	9
r	**-.390**	**.763**	**.265**	**.669**
m	-.80	1.9	.15	.28
b	.40	-.059	.15	.03
E	.12	.038	.08	.07
$\bar{\tau}$	.22	.29	.19	.15
R.H. ADJUST				
n	17	23	39	7
r	**-.427**	**.810**	**.326**	**.106**
m	-.60	1.2	.12	.16
b	.28	-.043	.097	.12
E	.096	.028	.051	.16
$\bar{\tau}$	.15	.20	.13	.18
R.H. & ΔZ ADJUST				
n	18	17	30	8
r	**-.363**	**.823**	**.289**	**-.192**
m	-.32	.63	.036	-.15
b	.17	-.055	.041	.14
E	.064	.013	.018	.071
$\overline{\hat{b}_{ext}}$	.096	.076	.051	.089
ΔZ ADJUST				
n	21	21	30	11
r	**-.360**	**.833**	**.156**	**.319**
m	-.67	1.0	.030	.12
b	.33	-.091	.066	.068
E	.12	.019	.028	.086
$\overline{\hat{b}_{ext}}$	.18	.11	.075	.11

Table 5.6 - Statistics for IMPROVE comparisons - Case 4

PARAMETER	DOSO	GRSM	MACA	SHEN
V_{max}		38	48	
V_{min}		7.6	5.5	
DEFAULT				
n		21	29	
r		**.790**	**.562**	
m		.879	.71	
b		-.055	.064	
E		.052	.10	
$\bar{\tau}$		.17	.25	
R.H. ADJUST				
n		13	27	
r		**.859**	**.519**	
m		.64	.43	
b		-.064	.051	
E		.035	.079	
$\bar{\tau}$		.14	.17	
R.H. & ΔZ ADJUST				
n		13	28	
r		**.651**	**.503**	
m		.22	.095	
b		-.017	.022	
E		.026	.020	
$\overline{\hat{b}_{ext}}$		.053	.048	
ΔZ ADJUST				
n		22	29	
r		**.657**	**.546**	
m		.309	.16	
b		-.018	.028	
E		.035	.030	
$\overline{\hat{b}_{ext}}$		.065	.071	

Table 5.7 - Statistics for IMPROVE comparisons - Case 5

PARAMETER	DOSO	GRSM	MACA	SHEN
V_{max}	162	144	140	55
V_{min}	24	12	9.7	8
DEFAULT				
n	28	46	58	27
r	**.722**	**.139**	**.0941**	**.790**
m	4.4	.34	.18	.67
b	-.051	.19	.17	.0076
E	.031	.11	.11	.029
$\bar{\tau}$	.25	.22	.19	.11
R.H. ADJUST				
n	26	32	56	18
r	**.726**	**.112**	**.119**	**.594**
m	2.7	.18	.15	.28
b	-.022	.149	.12	.028
E	.030	.10	.074	.020
$\bar{\tau}$	.17	.17	.13	.070
R.H. & ΔZ ADJUST				
n	26	35	57	18
r	**.393**	**-.0623**	**-.106**	**.795**
m	.35	-.046	.061	.10
b	.027	.063	.050	.0074
E	.032	.044	.026	.0036
$\overline{\hat{b}_{ext}}$	.052	.058	.044	.022
ΔZ ADJUST				
n	29	47	59	27
r	**.291**	**-.0424**	**-.0867**	**.798**
m	.68	-.046	-.080	.196
b	.044	.080	.074	.0047
E	.059	.050	.042	.0087
$\overline{\hat{b}_{ext}}$	.090	.070	.065	.035

Table 5.8 - Correlation coefficients (r) for Cleveland area NWS stations.

	BKL	CGF	LNN
CLE	0.577	0.547	0.367
LNN	0.479	0.478	
CGF	0.643		

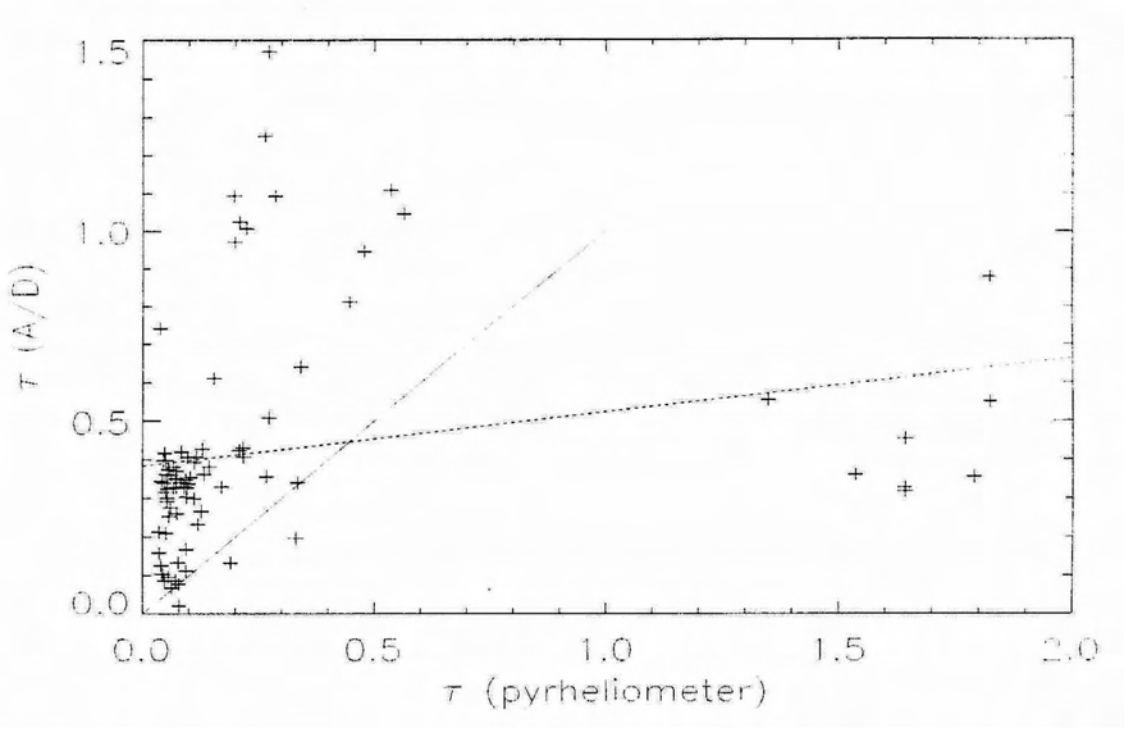

Figure 5.1 - Scatter plot of τ measured by a pyrheliometer and τ retrieved from GOES-8 using the Adding/Doubling model. Solid line corresponds to the one to one relationship, while the dashed line is the linear regression.

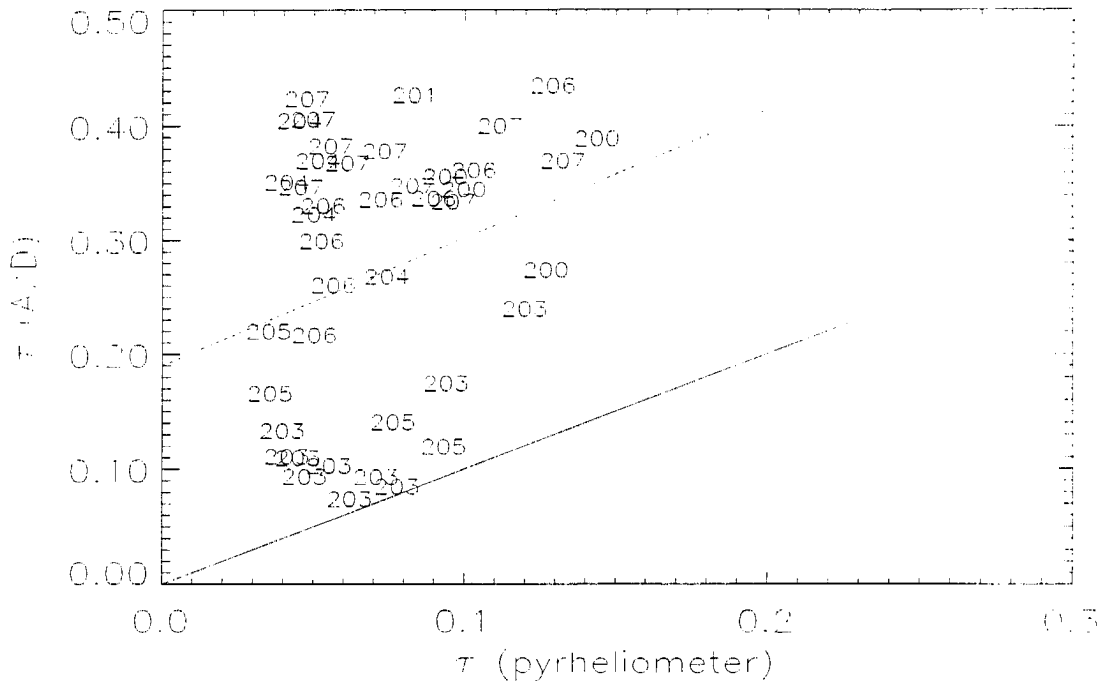

Figure 5.2 - Cloud filtered scatter plot of τ measured by a pyrheliometer and τ retrieved from satellite data. Numbers refer to Julian day, the solid line is the one-to-one relationship and the dashed line is the linear regression.

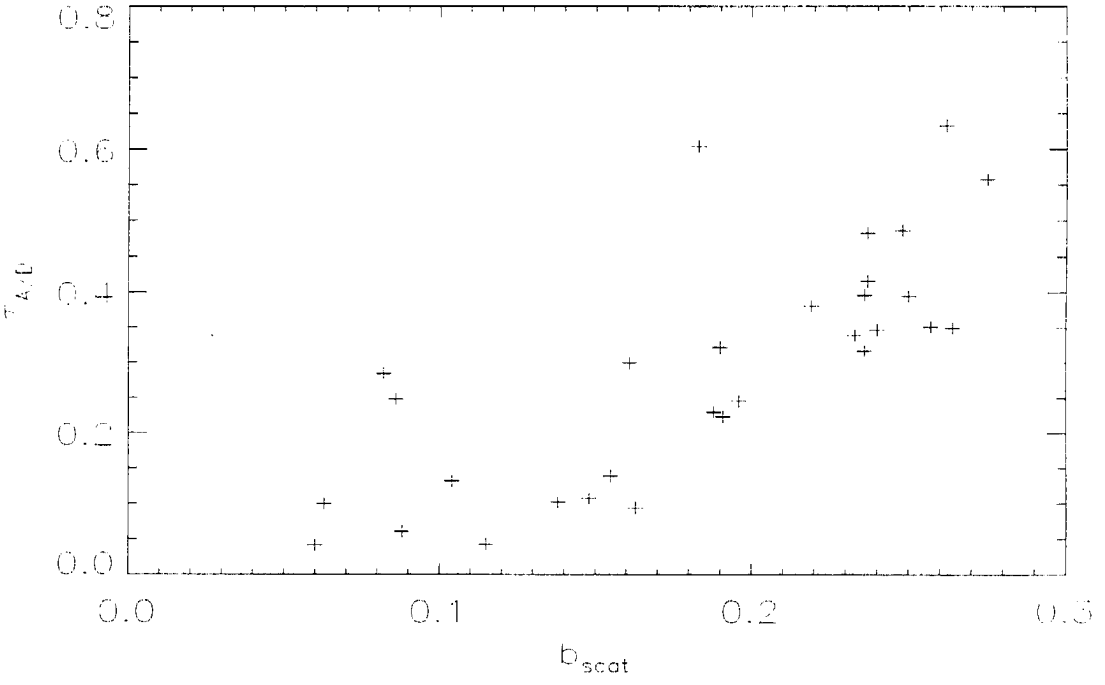

Figure 5.3 - Scatter plot of b_{scat} measured at GRSM to τ retrieved from GOES-8 using an A/D model during case 3.

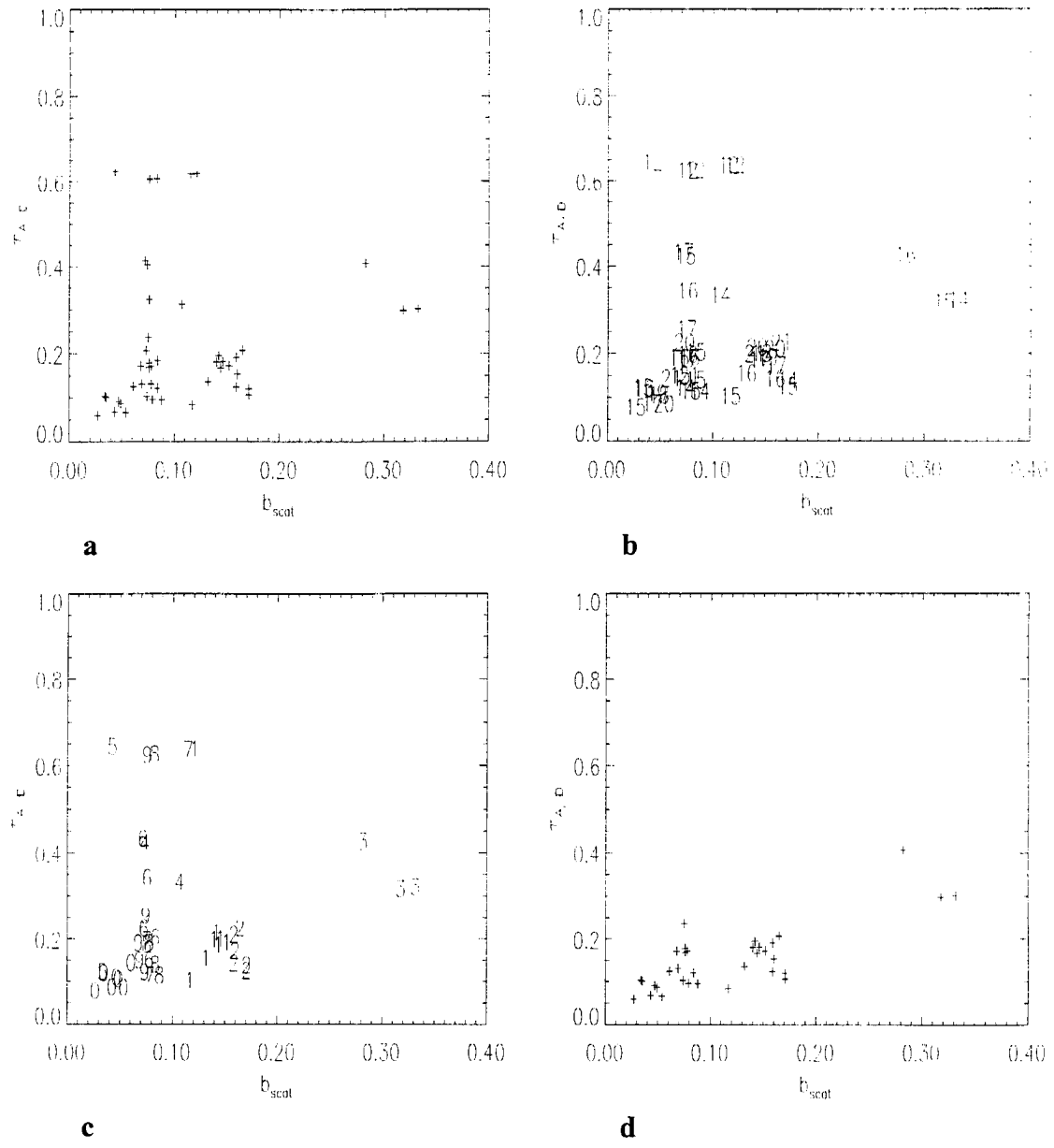

Figure 5.4 - Scatter plots for GRSM case 5 - a) scatter plot, b) scatter plot of time of day (UTC), c) scatterplot of Julian day - 240 (0 through 9 are days 240 through 249) and d) scatter plot with problem areas removed.

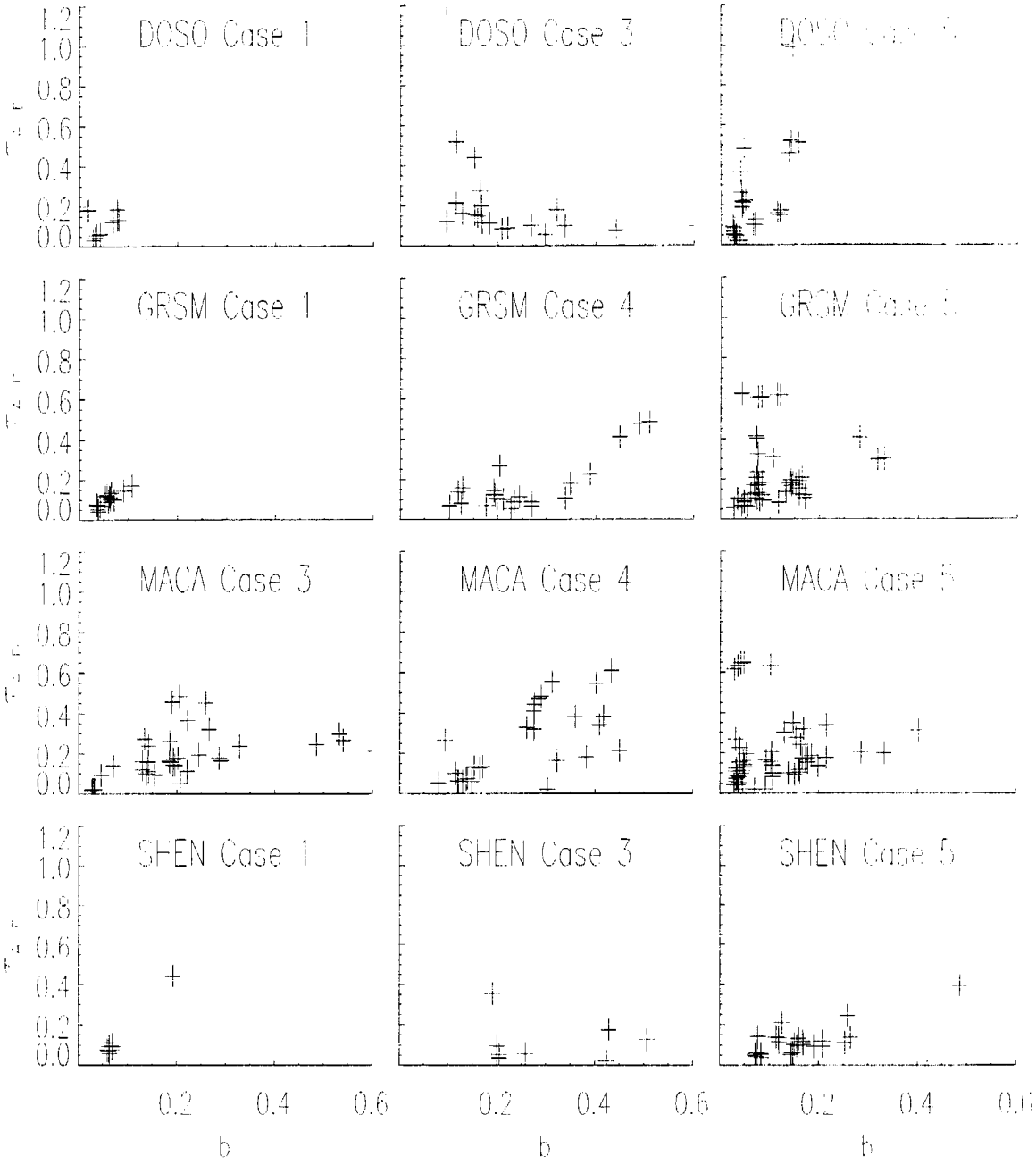

Figure 5.5 - Scatter plot for all comparisons (except GRSM case 3), where b is b_{ext} for SHEN and b_{scat} for DOSO, GRSM and MACA.

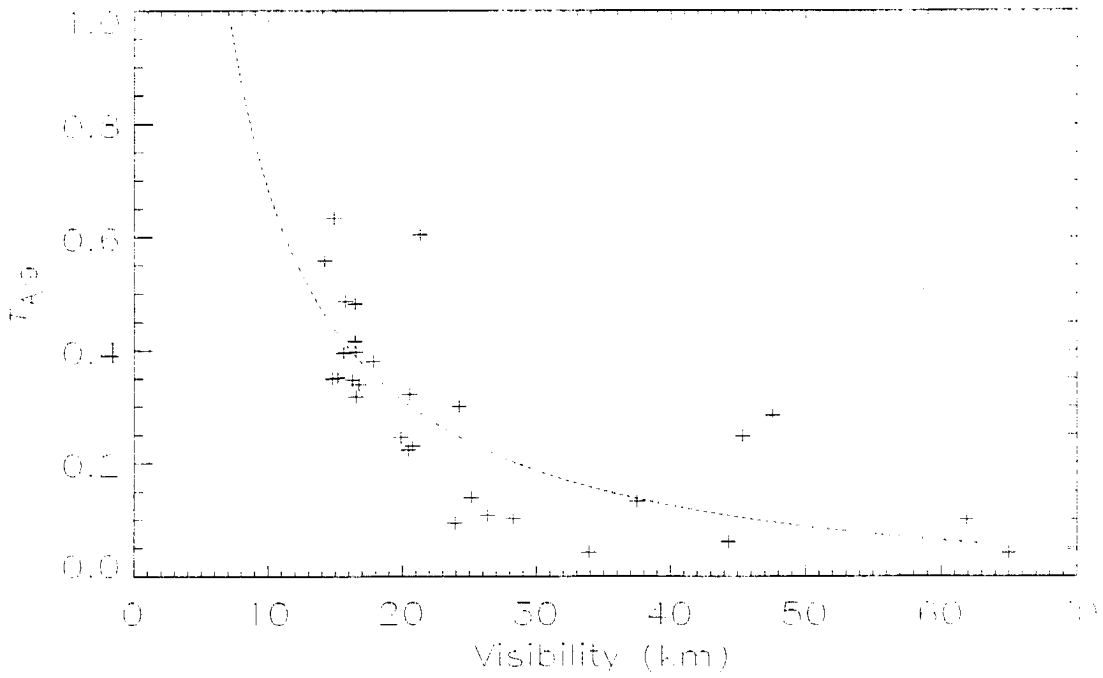

Figure 5.6 - Scatter plot of $\tau_{A/D}$ and visibility calculated from the nephelometer data at GRSM for case 3.

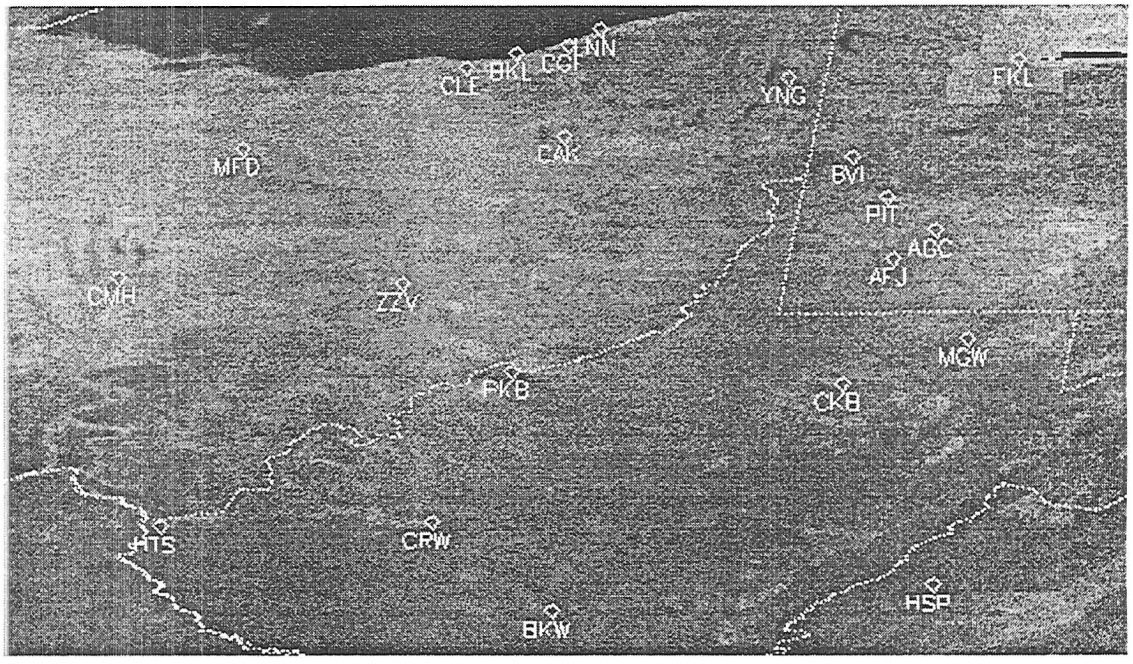

Figure 5.7 - An example of a background composite of surface reflectance for some of the NWS sites. Note: the dark spot in the northeastern edge is an artifact of the cloud clearing scheme, not an error, but an area where it was cloudy for the entire duration of the case.

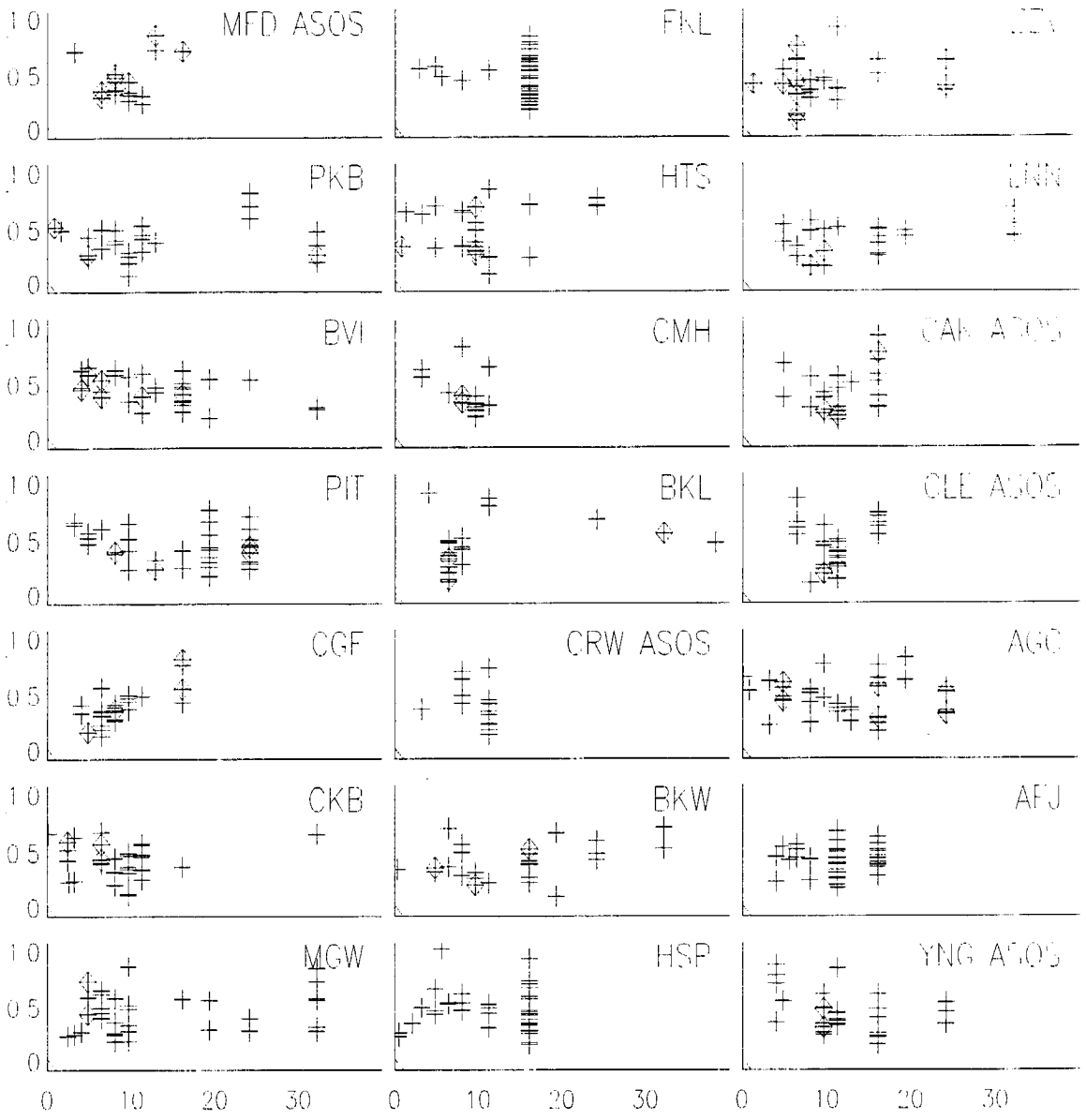

Figure 5.8 - Scatter plots comparing $\tau_{A/D}$ (ordinate) to NWS measured visibilities (abscissa). Diamonds are points when haze was reported by the station, ASOS sites are denoted as such.

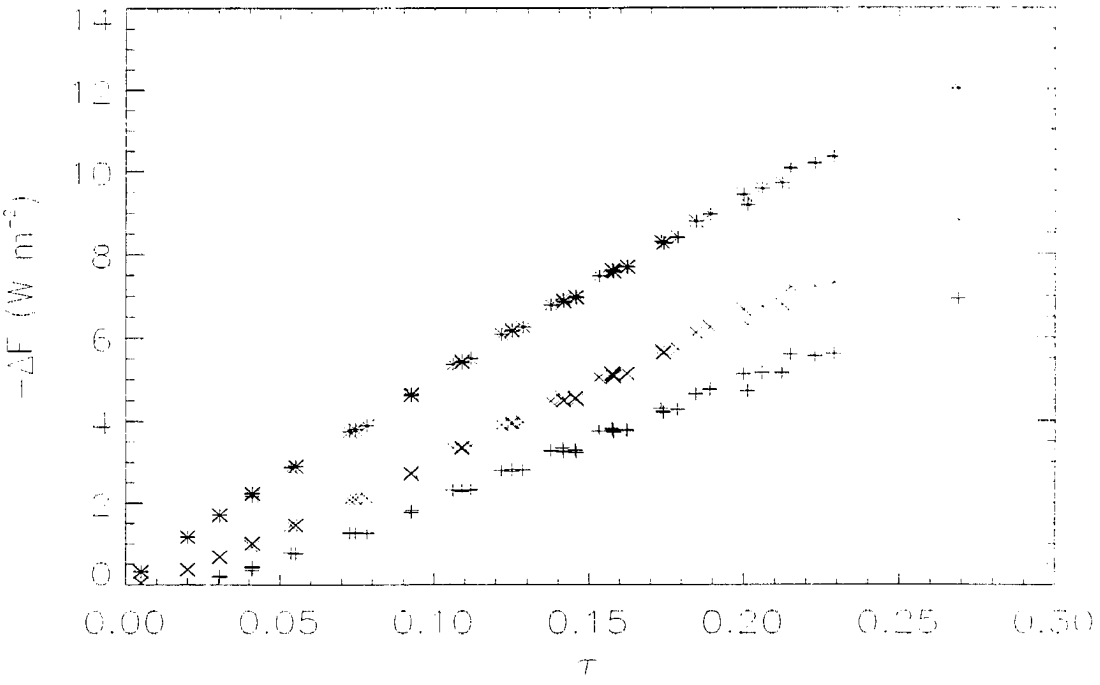

Figure 5.9 - The net shortwave lost to space ($-\Delta F$) due to aerosol forcing as a function of τ for θ_o = 0°(+), 30°(×), and 60°(*).

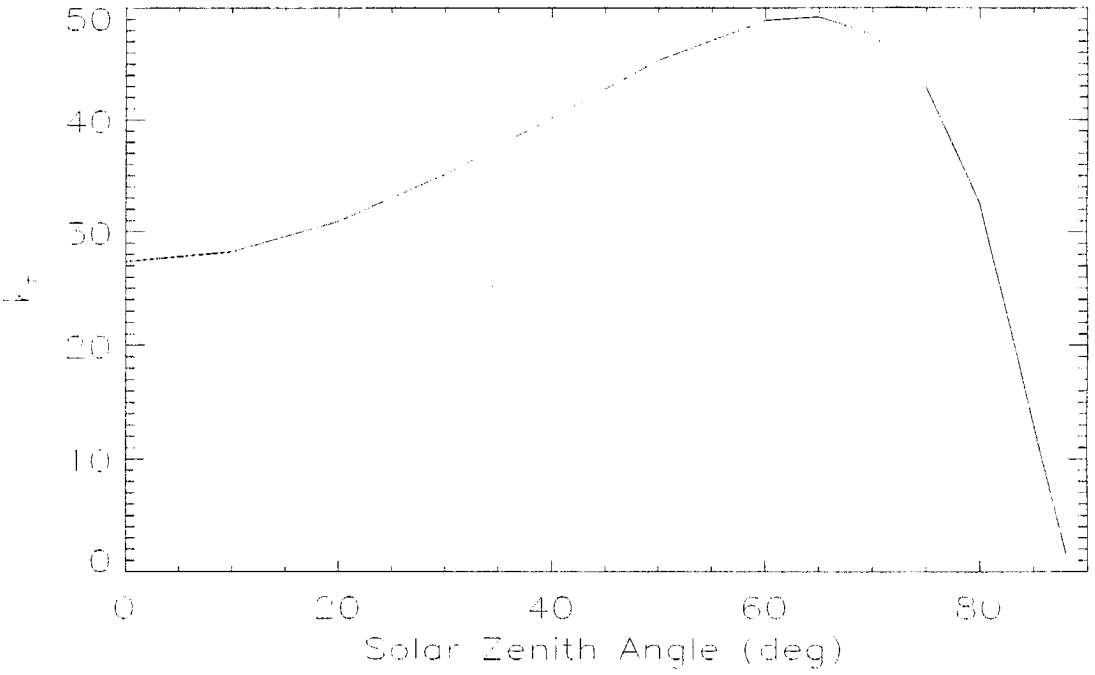

Figure 5.10 - k_τ as a function of θ_o

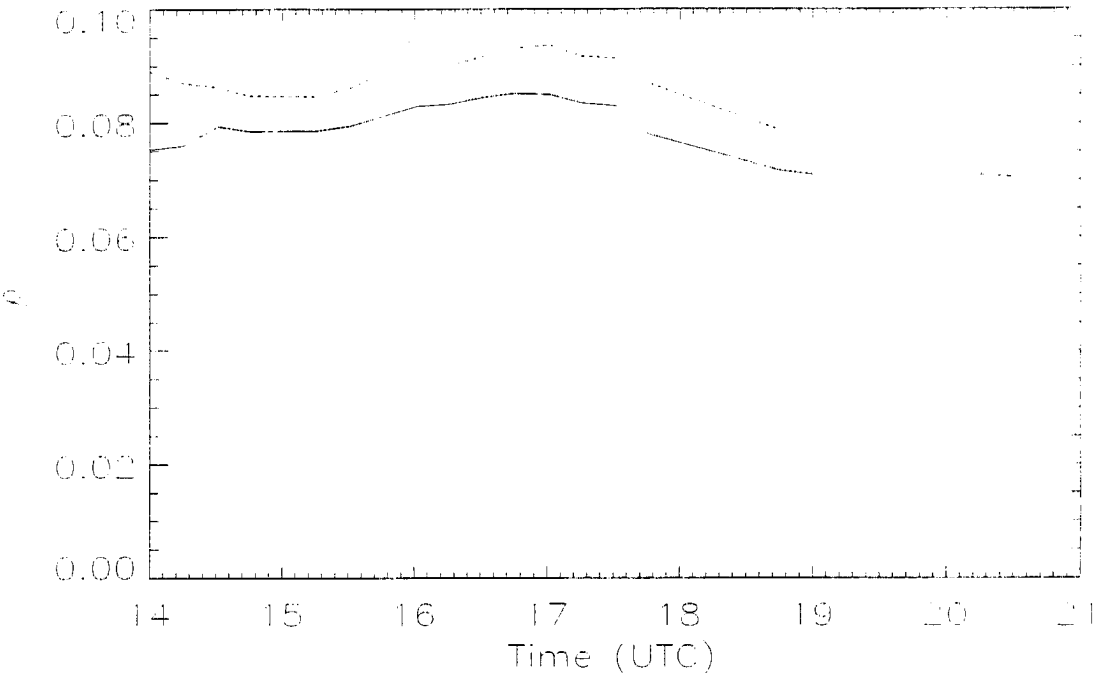

Figure 5.11 - Time series of background composited reflectance (solid) and satellite detected radiance (dashed) for Julian day 241 over GRSM.

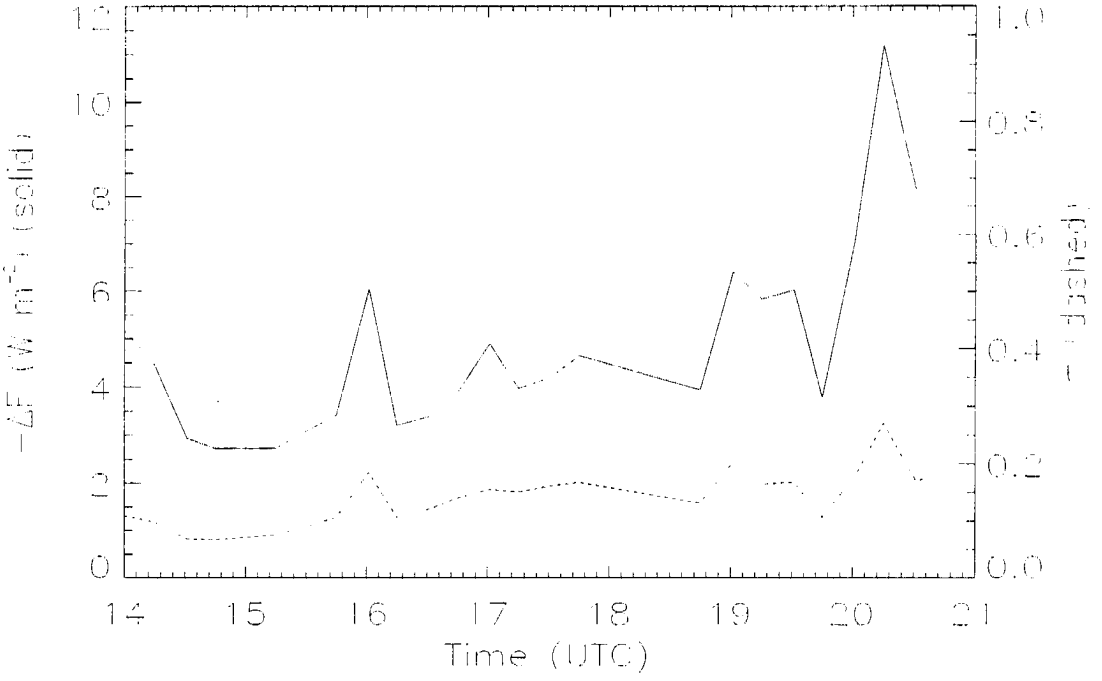

Figure 5.12 - Time series of aerosol forcing (solid) and τ (dashed) for GRSM Julian day 241.

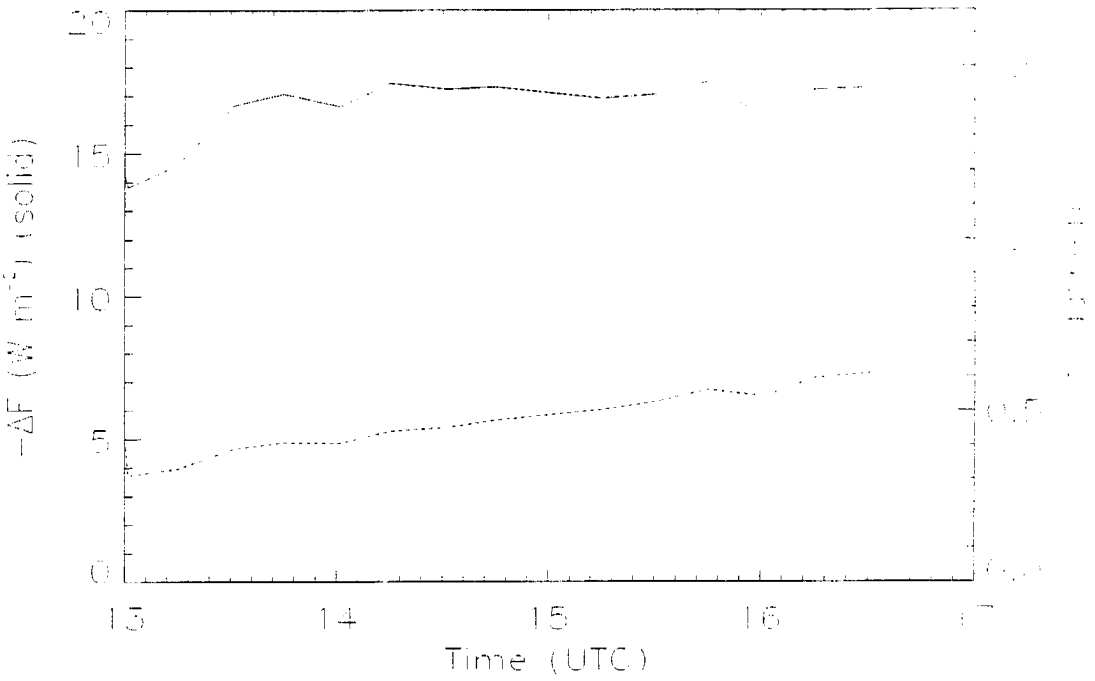

Figure 5.13 - Time series of aerosol forcing (solid) and τ (dashed) for the morning hours at MACA on Julian day 228.

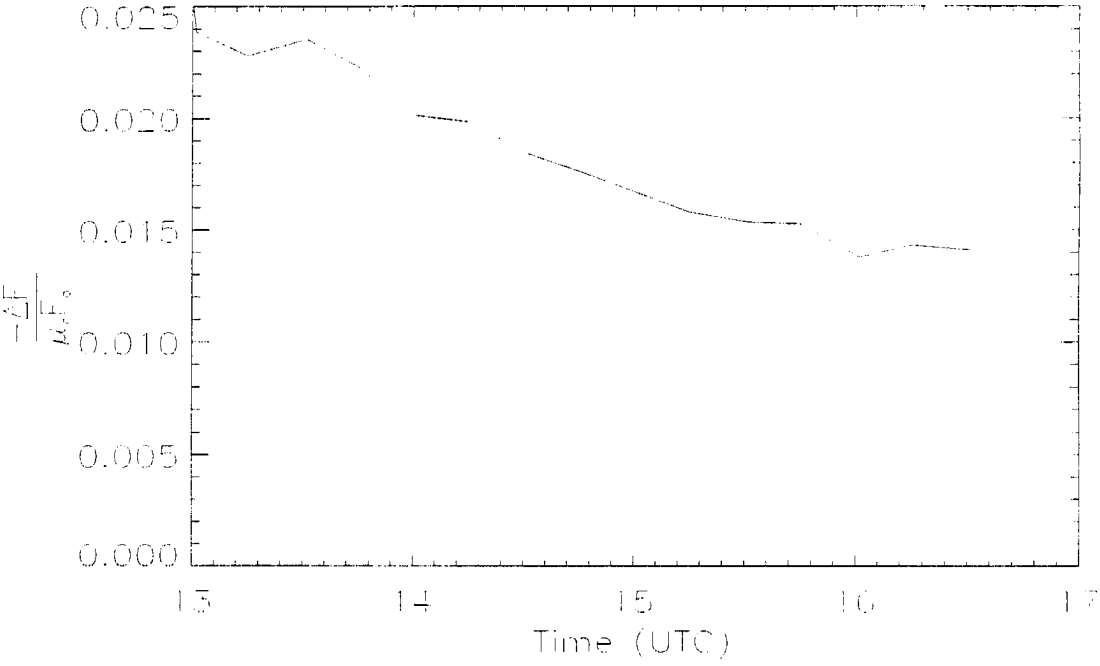

Figure 5.14 - Time series of the direct effect as a fraction of the available solar radiation for MACA, Julian day 228.

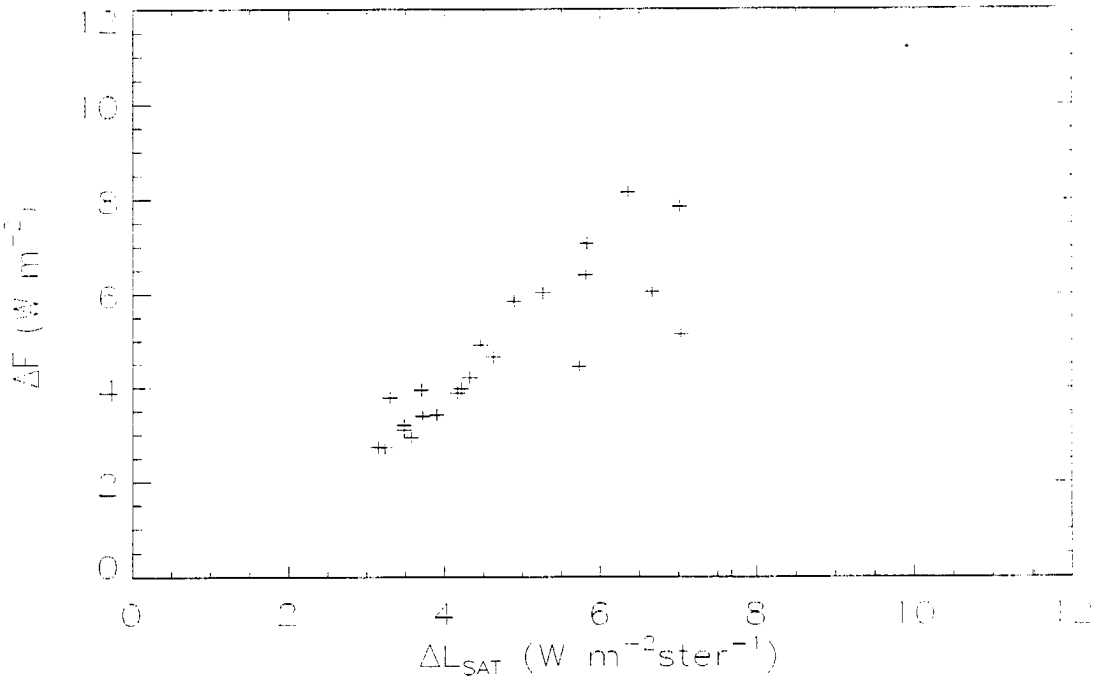

Figure 5.15 - Aerosol forcing vs. increase in satellite detected radiance for GRSM on Julian day 241.

Conclusion

6.1 Conclusions

Aerosols are important in chemical and radiative processes in the atmosphere. For this reason, it is important to know the temporal and spatial distributions of aerosols. A measured global distribution of aerosols is yet unknown, but this work is a step in that direction. The results of this study are summarized in table 6.1 and below.

Sensitivity studies showed that sensing aerosols from GOES-8 using an Adding/Doubling model is possible, at a high resolution of optical depth. Although, errors in the process allow retrievals at a lower resolution of τ. Noise in the system is attributed to navigational error, instrument uncertainty, cloud contamination (thin cirrus and sub-pixel cumulus), surface reflectance inhomogeneities, and water vapor variability. These effects are unaccounted for by the retrieval process and by the Adding/Doubling Model. Because of their randomness, it was assumed that spatial and temporal averaging removed most of their effects. This noise had a magnitude of $\Delta\tau$=0.08 and 0.12 over the ocean and land, respectively.

Bias errors due to inaccurate assumptions of model parameters were smaller in magnitude. For a 1% error in a parameter, single scatter albedo was the largest of biased errors, followed by the asymmetry parameter then calibration. For smaller τ (0.04 to 0.3)

the digitization of the signal caused the largest part of the error. The bias error was 0.05 to 0.16 for τ ranging from 0.04 to 1.0. τ measured in this study ranged from 0.04 to 0.6. By the process of background compositing to find a surface reflectance, the τ retrieved is the change in optical depth between that occurring on the background pixel and for the day of the retrieval. Therefore, the retrieved τ is an increase in optical depth over a background aerosol that is always present.

Unfortunately, the comparison to a pyrheliometer proved inconclusive, because the τ measured by the pyrheliometer failed to be significantly larger than the instrument noise after manual cloud filtering. Correlation between the retrieved τ and that measured was only 0.286.

Comparisons to IMPROVE site measurements of surface extinction and scattering coefficients were more successful due to more measurements during hazy conditions, although the number of samples for comparisons was greatly limited by the cloud coverage. The number of total samples decreased from 559 to 348 (38%) due to cloud coverage, most of which were for the sites at Shenandoah N.P. and Dolly Sods N.F. It was found that comparisons were better when surface extinction (or scattering) was higher. This is attributed to the signal of the aerosol (larger surface values usually mean higher τ values) being larger than the retrieval noise.

Retrieving τ again, using optical parameters adjusted by a measured surface relative humidity increases correlation in most cases, while having little affect in others. This is because the optical parameters were held fixed in the initial retrieval, but optical parameters can vary by 10% in asymmetry parameter and 2% in single scatter albedo due

to relative humidity variations. As mentioned above, for the same percentage change, the optical depth retrieval is more sensitive to error in single scatter albedo.

Adjusting the retrieved τ by the boundary layer height, thereby calculating a pseudo-retrieved boundary layer averaged extinction coefficient did not increase the correlation because the assumptions in the process. First, for a perfect correlation, the aerosol must be well mixed in the boundary layer. This allows the surface measurement to characterize the vertical structure. Secondly, the aerosol change must be confined to the boundary layer, so the retrieved τ corresponds to an amount of aerosol in the boundary layer. Other errors in this comparison result in the lack of vertical soundings near the IMPROVE sites and the change in station elevations between the IMPROVE and NWS sites. Also, day to day aerosol changes are not limited to the boundary layer and surface measurements are not always representative of the atmospheric optical depth.

Also, the temporal evolution of the boundary layer will play an important role in the correlation of surface parameters to layer integrated values. In afternoon hours, after solar heating has caused the boundary layer to be well-mixed, it is expected that the correlation might increase. However, in the morning hours the boundary layer can be stratified by the nocturnal inversion causing the surface to be decoupled from the boundary layer, decreasing the correlation. It is expected that the comparisons during morning hours decreased the correlation for this reason.

Comparison to National Weather Service visibility reports were for the most part uncorrelated. This was due to the noise in the retrieval and process of measuring visibility (discretization and low τ round-off). Also, retrieved τ and NWS reported haze

events were uncorrelated. Comparison here was also limited to the accuracy of the visibility measurement, which showed a large error when comparing visibility reports at two nearby NWS stations. This does not mean to imply that a modified, higher resolution NWS output could not be useful for future aerosol optical depth studies.

In general, comparisons were limited to the correlation of the actual τ to the comparison measurement, in this case, surface measurements of extinction and scattering coefficients. Also, the type of cloud filter limits the optical depth retrieved. It is important to remove clouds, but not aerosols. Reflectivities produced by aerosols are in the range from the surface reflectance to on the order of thin clouds. The background composite produces an excellent cloud filter, although has a hard time in distinguishing thin clouds from large amounts of aerosol.

The results of the direct effect investigation showed that the aerosol forcing was linearly dependent on τ. This relationship changed for different solar zenith angles. For the aerosol studied, the forcing was at a maximum when $\theta_0 = 65°$. Aerosol forcing was integrated over a day, to find total energy lost to space due to aerosol. The amount for a hazy day was equivalent to 0.084mm loss in evaporation (assuming all lost energy would have been used in evaporation). Also, the aerosol forcing is dependent upon the increase in satellite detected radiation, which showed that the direct effect can be directly measured by satellite.

6.2 Future Work

Some possible future research that was pondered in the process of working on this thesis includes:

- The 11 and 12 μm channels on the Imager (channel 4 and 5) have a difference in absorption of low-level water vapor. Low-level water vapor could be retrieved from these channels and used to adjust g and ω_o in the retrieval.
- Including the adjacency effect into the A/D model might improve comparison correlations over land.
- The direct effect can be measured directly by satellite, so using the compositing scheme and integrating the radiance received at the satellite over the upward hemisphere, the measurement of aerosol forcing could be calculated over large areas.
- Also using the compositing scheme, measurements of surface reflectances and bi-directional reflectance properties could be made by including measurements from GOES-9 and NOAA/AVHRR for large areas, at low horizontal resolution (~1 km^2).
- Calibrate GOES-8 and 9 using a radiative transfer model and assumed atmospheric properties. The degradation of the system response needs to be quantified before further work can be done using the visible channel.
- Using the background compositing scheme, a cloud filter can be developed.

Table 6.1 - Summary of thesis.

QUESTION	METHOD	ANSWER
Is the A/D model adequate for τ retrieval from GOES-8 over land?	Use the A/D R.T. model to find the sensitivity of the model to an aerosol layer over varying background reflectances.	If the background reflectance is not in the range of the critical reflectance then retrievals are possible.
What are the errors involved with retrieving τ from GOES-8?	Vary A/D model parameters and find which parameters and assumptions are likely to cause the most error.	$\Delta\tau = \pm(0.05\text{-}0.16)$ due to ω_o, g, calibration, and $\Delta\tau = \pm 0.1$ due to noise in the retrieval (navigation and unaccounted for variables)
Are satellite retrievals of τ comparable to surface point measurements of similar parameters?	Compare τ retrievals to surface point measurements: pyrheliometer, transmissometer, nephelometer, and NWS visibility reports.	Comparisons were best for the IMPROVE data sets. NWS not comparable due to stepping in visibility reports. Not enough aerosol over the pyrheliometer.
Does knowledge of the boundary layer depth decrease the scatter in the comparisons?	Divide the retrieved τ values by the boundary layer depths estimated from NWS sondes and compare to surface data.	No noticeable increase in correlation of comparisons. Errors involved in this calculation were large.
How does the inclusion of surface relative humidity affect the retrieval?	Vary the optical parameters ω_o and g as a known function of RH and compare changes.	Resulted better correlation in some cases, and little change in others (it did not significantly decrease correlation).
What do retrievals reveal about the direct effect of aerosols?	Use a 2-stream R.T. model to find the direct effect of the retrieved τ values.	For constant values of θ_o, g and ω_o, the forcing was a direct function of τ, similar to that found by Charlson et al. (1991) and might be directly estimated from satellite data.

References

Arino, O., G. Dedieu, and P. Y. Deschamps, 1991: Accuracy of Satellite Land Surface Reflectance Determination, *J. Appl. Met.*, **30**, 960-972.

ASOS Technical Note, 1994: *Algorithms for the Automated Surface Observing System (ASOS),* U.S. Dept. of Commerce, ISL Office Note 94-4.

Behunek, J.L, J.M. Forsythe, and T.H. Vonder Haar, 1993: Satellite analysis of Kuwaiti oil smoke plumes. In Proceedings of the 1993 Battlefield Atmospherics Conference, 30 Nov. - 2 Dec. 1993, Las Cruces, NM, U.S. Army Research Lab., White Sands Missile Range, NM, 357-368.

Carlson, T. N., 1979: Atmospheric Turbidity in Saharan Dust Outbreaks as Determined by Analyses of Satellite Brightness Data, *Mon. Wea. Rev.*, **107**, 322-335.

Charlson, R. J., J. Langner, H. Rodhe, C. B. Leovy, and S. G. Warren, 1991: Perturbation of the northern hemispheric radiative balance by backscattering from anthropogenic sulfate aerosols, *Tellus*, **43AB**, 152-163.

Chesters, Dennis, 1994: http://climate-f.gsfc.nasa.gov/~chesters/text/imager. calibration.html

Conel, J. E., 1990: Determination of surface reflectance and estimates of atmospheric optical depth and single scattering albedo from Landsat Thematic Mapper data, *Int. J. of Rem. Sensing,* **11**, 783-828.

Corfidi, S. F., Lost Horizons, 1993: *Weatherwise*, June/July, 12-17.

d'Almeida, G. A., P. Koepke, and E. P .Shettle, 1991: *Atmospheric Aerosols: Global Climatology and Radiative Characteristics,* A. Deepak Publ., 561 pp.

Durkee, P. A., 1984: The relationship between marine aerosol particles and satellite-detected radiance, Ph.D. Dissertation, C.S.U. Atmospheric Science Paper No. 380, 124 pp.

Fraser, R. S., 1993: Optical Thickness of Atmospheric Dust over Tadzhikistan, *Atm. Env.*, **27A**, 2533-2538.

Fraser, R. S., Y. J. Kaufman, and R. L. Mahoney, 1984: Satellite measurements of aerosol mass and transport, *Atm. Env.*, **18**, 2577-2584.

Fu, Q. and K. N. Liou, 1992: On the correlated k-distribution method for radiative transfer in nonhomogeneous atmospheres, *J. Atmos. Sci.*, **49**, 2139-2156.

Greenwald, T. J. and G. L. Stephens, 1988: Application of a Adding-Doubling Model to Visibility Problems, C.S.U. Atm. Sci. Paper, 89 pp.

Griggs, M., 1979: Satellite Observations of Atmospheric Aerosols During the EOMET Cruise, *J. Atmos. Sci.*, **36**, 695-698.

Harrington, J, P. Gabriel and G. Stephens, Parameterization of radiative transfer models, Part II: Utility of adjoint and perturbation methods, in preparation for *J. Atmos. Sci.*, 1996.

Hindman, E. E., P. A. Durkee, P. C. Sinclair, and T. H. Vonder Haar, 1984: Detection of marine aerosol particles in coastal zones using satellite imagery, *Int. J. Remote Sensing*, **5**, 577-586.

Houghton, H. G., 1985: *Physical Meteorology*, MIT Press, 442 pp.

Husar, B. H. and W. E. Wilson, 1993: Haze and Sulfur Emission Trends in the eastern United States, *Environ. Sci. Tech.*, **27**, 12-16.

Kaufman, Y. J., 1993: Aerosol Optical Thickness and Atmospheric Path Radiance, *J. Geophys. Res.*, **98**, 2677-2692.

Kaufman, Y. J. and J. H. Joseph, 1982: Determination of Surface Albedos and Aerosol Extinction Characteristics from Satellite Imagery, *J. Geophys. Res.*, **87**, 1287-1299.

Kaufman, Y. J., 1984: Atmospheric Effect on Spatial Resolution of Surface Imagery, *Appl. Optics*, **23**, 3400-3408.

Kaufman, Y. J. and R. S. Fraser, 1983: Light Extinction by Aerosols During Summer Air Pollution, *J. Clim. and Appl. Met.*, **22**, 1694-1706.

Kaufman, Y. J., 1987: Satellite Sensing of Aerosol Absorption, *J. Geophys. Res.*, **92**, 4307-4317.

Kaufman, Y. J., T. W. Brakke, and E. Eloranta, 1986: Field Experiment for Measurement of the Radiative Characteristics of a Hazy Atmosphere, *J. Atmos. Sci.*, **43**, 1135-1150.

Kaufman, Y. J., 1979: Effect of the Earth's Atmosphere on contrast for zenith observations, *J. Geophys. Res.*, **84**, 3165-3172.

Kaufman, Y. J., R. S. Fraser, and R. A. Ferrare, 1990: Satellite Measurements of Large-Scale Air Pollution: Methods, *J. Geophys. Res.*, **95**, 9895-9909.

Kidder, S. Q. and T. H. Vonder Haar, 1995: *Satellite Meteorology: An Introduction*, Academic Press, 466 pp.

Kiehl, J. T. and B. P. Briegleb, 1993: The Relative roles of Sulfate Aerosols and Greenhouse Gases in Climate Forcing, *Science*, **260**, 311-314.

King, M. D., S. C. Tsay, and S. Platnick, 1995: *In Situ* Observations of the Indirect Effects of Aerosols on Clouds, in *Aerosol Forcing of Climate*, R. J. Charlson and J. Heintzenberg, eds., John Wiley & Sons, Ltd., 416 pp.

Koschmeider, H., 1924: Theorie der horizontalen Sichtweite, *Beirn. Phys. Atmos.*, **12**, 33-35 and 171-181.

Liou, K. N., 1980: *An Introduction to Atmospheric Radiation*, Academic Press, Inc., 392 pp.

Malm, W. C., J. F. Sisler, D. Huffman, R. A. Eldred, and T. A. Cahill, 1994: Spatial and seasonal trends in particle concentrations in the United States, *J. Geophys. Res.*, **99**, 1347-1370.

McDonald, C. J., J. Carbajal, J. Florres, R. Mesta, G. Carillo, M. A. Nunez and L. Carillo, 1993: Measurement of the overall modulation transfer function of desert atmospheres, *In proceedings of SPIE - The international Society for Optical Engineering*, **1968**, 745-765.

Mekler, Y. and Y. J. Kaufman, 1980: The effect of the earth's atmosphere on contrast reduction for a non-uniform surface albedo and two-halves field, *J. Geophys. Res.*, **85**, 4067-4083.

Menzel, W. P. and J. F. W. Purdom, 1994: Introducing GOES-I: The first of a new generation of Geostationary Operational Environmental Satellites, *Bull. of the Amer. Met. Soc.*, **75**, 757-781.

Molenar, J. V., G. Persha and W. C. Malm, 1990: Long path transmissometer for measuring ambient atmospheric extinction, *Environment and Pollution Measurement Sensors and Systems,* **1269**, 37-55.

Norton, C. C., F. R. Mosher, B. Hinton, D. W. Martin, D. Santek and W. Kuhlow, 1980: A Model for Calculating Desert Aerosol Turbidity over the Oceans from Geostationary Satellite Data, *J. Appl. Met.,* **19**, 633-644.

Nemesure, S., R. Wagener, and S. E. Schwartz, 1995: Direct Shortwave Forcing of Climate by Anthropogenic Sulfate Aerosol: Sensitivity to Particle Size, Composition and Relative Humidity, submitted to *J. Geophys. Res.,* **100**, 26,105-26,116.

Peixoto, J. P. and A. H. Oort, 1992: *Physics of Climate*, American Institute of Physics, 520 pp.

Pinnick, R. G., G. Fernandez, E. Martinez-Andazola, B. D. Hinds, A. D. A. Hansen and K. Fuller, 1993: Aerosol in the Arid Southwestern United States: Measurements of Mass Loading, Volatility, Size Distributions, Absorption Characteristics, Black Carbon Content, and Vertical Structure to 7 km above Sea Level, *J. Geophys. Res.,* **98**, 2651-2666.

Platnick, S. and S. Twomey, 1994: Remote Sensing the Susceptibility of Cloud Albedo to Changes in Droplet Concentration, *Atm. Res.,* **34**, 85-98.

Robock, A., 1988: Surface Temperature Effects of Forest Fire Smoke Plumes, in *Aerosols and Climate*, P. V. Hobbs and M. P. McCormick, eds., A. DEEPAK Publ., 435 - 442.

Rodgers, C. D., 1990: Characterization and Error Analysis of Profiles Retrieved from Remote Sounding Measurements, J. Geophy. Res., **95**, 5587-5595.

Schneider, T. L. and K. A. Fuller, 1994: An Intercomparison of Doubling-Adding and Backward Monte Carlo Radiative Transfer Models for Aerosol Modeling, in the Proceedings of the International Specialty Conference on Aerosols and Atmospheric Optics: Radiative Balance and Visual Air Quality in Snowbird, Utah, Air & Waste Management Assoc. and Amer. Geophys. Union.

Spinhirne, J. D., J. A. Reagan and B. M. Herman, 1980: Vertical Distribution of Aerosol Extinction Cross Section and Inference of Aerosol Imaginary Index in the Troposphere by Lidar Technique, *J. Appl. Met.,* **19**, 426-438.

Stephens, G. L., 1994: *Remote Sensing of the Lower Atmosphere: An Introduction,* Oxford University Press, 523 pp.

Stephens, G. and P. Gabriel, Parameterization of radiative transfer models, Part I: Validity of simple models, in preparation for *J. Atmos. Sci.*, 1996.

Tsay, S.-C., G. L. Stephens and T. J. Greenwald, 1991: An investigation of aerosol microstructure on visual air quality, *Atm. Env,* **25A**, 1039-1053.

Weinreb , M., personal communication and Memo.

Appendix: Radiance to Reflectance for GOES-8 Channel 1

The following is a discussion on converting GOES-8 Imager visible radiance measurements to reflectance values. An overview of the GOES-8 Imager is provided then the reflectance equation is derived.

GOES-8 Imager - Channel One

The Imager aboard GOES-8 and its data system reports radiance measurements in digital count values ranging from 0 to 1023 counts. The linear response of the sensor over the range of the input signal provides the following calibration equation to convert counts (n) to radiance (L):

$$L = mn + b \tag{A.15}$$

where m is the inverse of sensor responsivity and b is the offset. The pre-launch values of these calibration coefficients, measured at ITT in Fort Wayne, Indiana, are m = 0.551 $Wm^{-2}ster^{-1}\mu m^{-1}count^{-1}$ and b = -15.3 $Wm^{-2}ster^{-1}\mu m^{-1}$ (available at the WWW site http://climate-f.gsfc.nasa.gov/~chesters/text/imager.calibration.html).

These values are only valid prior to launch and soon thereafter. Otherwise, the sensor is subject to response drift, which has been noticed in visible data from GOES-8. Weinreb (1995) calculated a decrease in responsivity of about 15% and is attributed to pre-launch storage (of 15 months) and the trauma of launch. There do exist methods to determine these calibration coefficients in-flight, although they require assumptions of the surface reflectance and atmospheric optical properties. Surfaces such as the ocean and deserts are useful for this process because their spatially homogeneous reflectances are well-studied. Whereas atmospheric optical properties, such as vertical structure of optical depth, single scatter albedo and asymmetry parameter of aerosols, are usually assumed variables. Aerosols over the ocean may have a relatively constant distribution and optical parameters, whereas aerosols over land are more variable in both respects. These atmospheric variables can be used in a radiative transfer model to calculate a radiance the satellite sensor should detect. This method was used by Fraser et al. (1984) to calculate GOES-7 VISSR coefficients from a region in the Atlantic Ocean.

Reflectance

The following discussion of reflectance does not include spectral dependence. Surface reflectance, solar emittance and the Imager sensor response have different spectral dependencies. Therefore, radiances mentioned hereafter are band-averaged quantities, averaged over the spectral response of the GOES-8 Imager (0.55-0.75 μm). The process of this band averaging is discussed in the next section.

Figure A.1 shows the geometry of a radiance from a source direction (the Sun) with zenith angle θ_o and azimuth angle ϕ_o reflected by a surface (dA) into the direction θ and ϕ (Stephens, 1994). The equation of reflected radiance (L_r) defined by Kidder and Vonder Haar (1995) is:

$$L_r(\theta_r,\phi_r) = \int_0^{2\pi}\int_0^{\pi/2} L_i(\theta_i,\phi_i)\gamma_r(\theta_i,\phi_i;\theta_r,\phi_r)\cos\theta_i \sin\theta_i d\theta_i d\phi_i \qquad (A.16)$$

where L_i is the incident radiance from the direction (θ_i, ϕ_i), which is partially reflected (γ_r) into the direction (θ_r, ϕ_r). γ_r is the bi-directional reflection function (BDRF) which requires:

$$\int_0^{2\pi}\int_0^{\pi/2} \gamma_r(\theta_r,\phi_r;\theta_o,\phi_o)\cos\theta_r \sin\theta_r d\theta_r d\phi_r \equiv A \qquad (A.17)$$

such that γ_r is the fraction of L_i reflected to the direction θ_r, ϕ_r and A is the total fraction of reflected light in all directions, the albedo (sometimes termed the total directional reflectance). Then, considering the sun as the only source, L_i becomes a delta function:

$$L_i(\theta_i,\phi_i) = \begin{cases} L_o & \theta_i = \theta_o, \phi_i = \phi_o \\ 0 & \theta_i \neq \theta_o, \phi_i \neq \phi_o \end{cases} \qquad (A.18)$$

where L_o is the solar emitted radiance. Also, if the reflecting surface is assumed to be an isotropic (or Lambertian) reflector, then incident radiance is reflected uniformly in all directions. Defining:

$$\gamma_r(\theta_r,\phi_r;\theta_o,\phi_o) = \frac{\rho}{\pi} \qquad (A.19)$$

so

$$\int_0^{2\pi}\int_0^{\pi/2} \gamma_r(\theta_r,\phi_r;\theta_i,\phi_i)\cos\theta_r \sin\theta_r d\theta_r d\phi_r \equiv \rho, \qquad (A.20)$$

where ρ is the effective isotropic albedo. Using equations A.4 and A.5, equation A.2 becomes:

$$L_r(\theta_r, \phi_r) = L_o \cos\theta_o \Omega_o \frac{\rho}{\pi} \tag{A.21}$$

where Ω_o is the solid angle of the sun subtended by the earth. Thus,

$$L_r(\theta_r, \phi_r) = \frac{\rho}{\pi} F_o \cos\theta_o \tag{A.22}$$

where $F_o = L_o \Omega_o$.

Calculation of GOES-8 Imager Channel 1 Reflectance

So from equation A.8, the effective isotropic visible albedo is calculated from the GOES-8 Imager by:

$$\rho = \frac{\pi L_r(\theta_r, \phi_r)}{F_o \cos\theta_o}. \tag{A.23}$$

L_r is calculated from Imager data counts and the calibration coefficients discussed above. Alternatively, if γ_r for the surface is known or assumed, then equation A.9 can be used without the isotropic assumption. The latitude and longitude of the image pixel and time of satellite scan determine $\cos\theta_o$. F_o is the incident radiance at the same wavelengths that measure L_r. So F_o is the theoretical radiance measured if the GOES-8 Imager Channel 1 were to look directly at the sun. It is determined by:

$$F_o = \frac{\int_0^\infty S_\lambda w_\lambda d\lambda}{\int_0^\infty w_\lambda d\lambda} \tag{A.24}$$

where w_λ is the spectral response, or weighting function, of channel 1 of the Imager and S_λ is the spectral irradiance of the Sun. Figure A.2 shows the solar emittance and figure A.3 shows the relative spectral weighting function of channel 1 of the Imager on GOES-8. From figure A.3, it can be seen that there exist limits on the weighting function outside of which the sum approaches zero:

$$\int_0^{\lambda_{min}} w_\lambda d\lambda + \int_{\lambda_{max}}^{\infty} w_\lambda d\lambda \approx 0 \tag{A.25}$$

where λ_{min} and λ_{max} are determined from w_λ. In the weighting function provided (Weinreb, personal communication), $[\lambda_{min}, \lambda_{max}] = [0.45, 1.01\mu m]$. So equation A.11 becomes:

$$F_o = \frac{\int_{\lambda_{min}}^{\lambda_{max}} S_\lambda w_\lambda d\lambda}{\int_{\lambda_{min}}^{\lambda_{max}} w_\lambda d\lambda} \tag{A.26}$$

Applying the data in figures A.2 and A.3 to equation A.12 results in:

$$F_o = 1627.945 \text{ Wm}^{-2} \tag{A.27}$$

Therefore, the effective isotropic reflectance is calculated by:

$$\rho = \frac{L_r(\theta_r, \phi_r)\pi}{1627.945\cos\theta_o} = \frac{L_r(\theta_r, \phi_r)}{518.191\cos\theta_o} = \frac{L_r(\theta_r, \phi_r)}{\cos\theta_o} 1.92979 \times 10^{-3}. \tag{A.28}$$

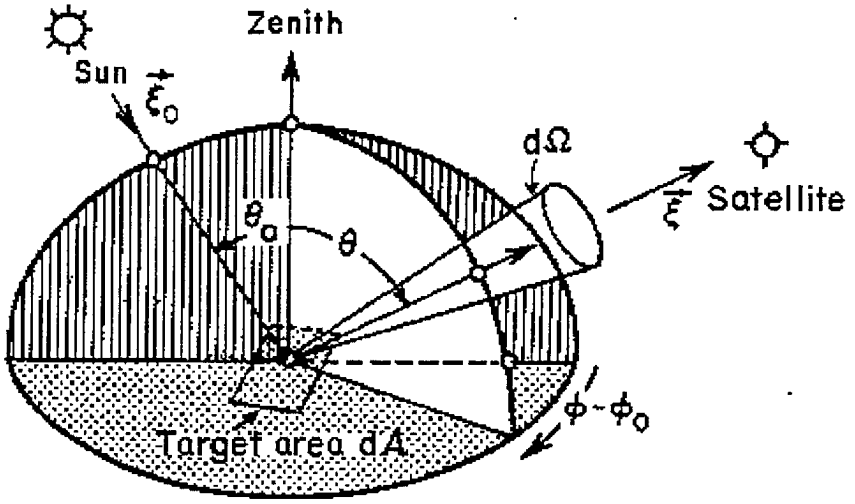

Figure A.1 - Schematic of reflected radiance, $L(\theta,\phi)$, by target area, dA, for the source being the sun, ξ_0 (Stephens, 1994).

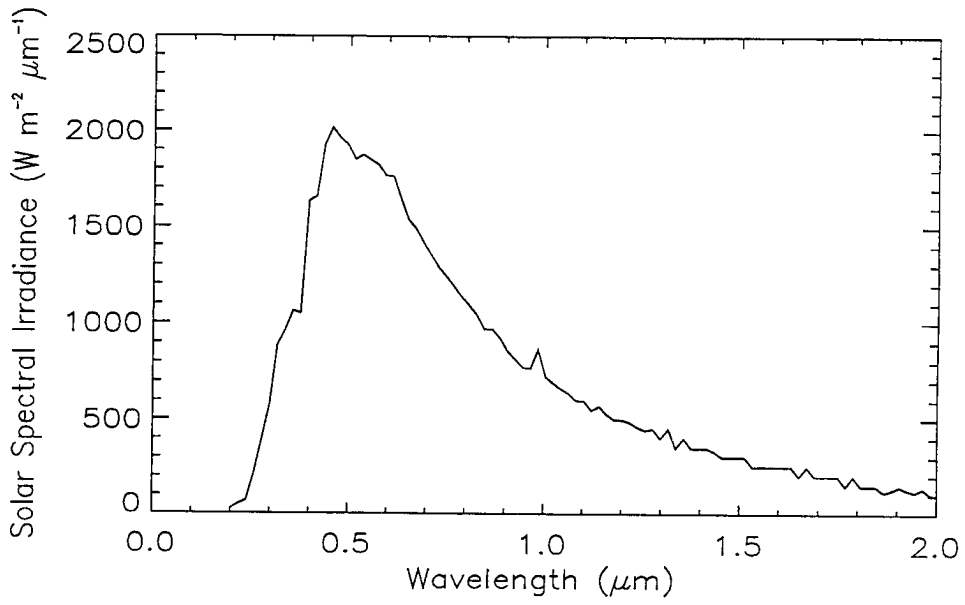

Figure A.2 - The TOA solar spectral irradiance as a function of wavelength.

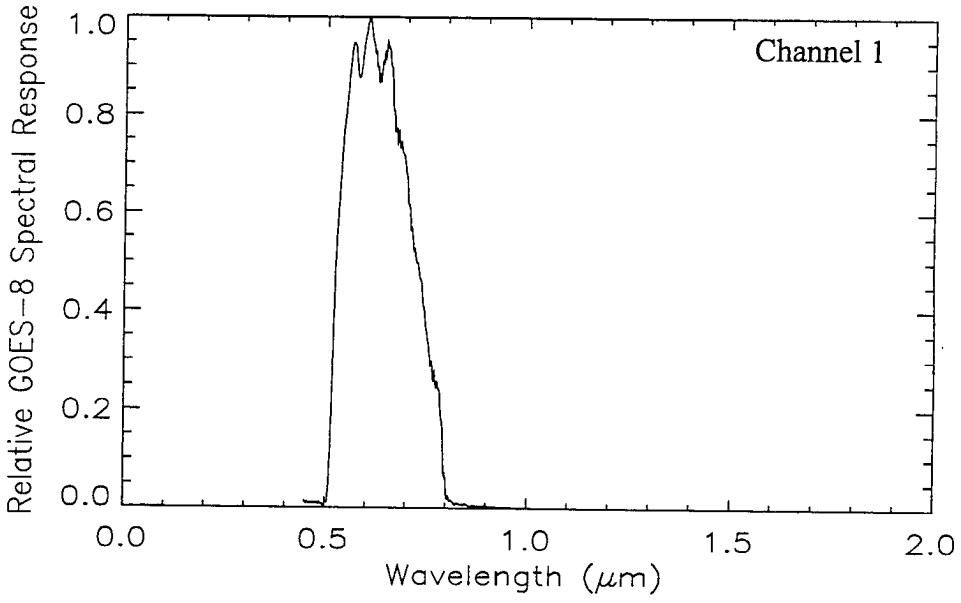

Figure A.3 - The relative weighting function (or spectral response) as a function of wavelength.